Online characterization of particle based reactions by laser backscattering

by

Miguel Medina

A thesis submitted in partial fulfillment of the requirements for the degree of

Master of Science

in

Chemical Engineering

Department of Chemical and Materials Engineering

University of Alberta

ABSTRACT

A fiber optic dynamic light scattering device was successfully developed for the *in-situ* characterization of particle size in turbid media. Currently available techniques are only capable of performing characterizations at room temperature and are highly limited by the turbidity of the sample.

In-situ particle size characterization was accomplished using the diffuse wave spectroscopy theory and time-dependent autocorrelation analysis. Using this basis for the interpretation, information regarding the particle morphology was obtained from the backscattering signals using two simultaneous lasers, of 532 and 655nm wavelength, at elevated pressures up to 5 MPa, and at temperatures up to 420 °C.

Validation of the analytical technique was achieved by studying a stable particulate dispersion of Carbon Lampblack (CB) in water and 1-methylnaphthalene. The 162 nm average particle size of the dispersion was characterized *ex-situ* with transmission electron microscopy and a commercial laser diffraction apparatus. The average particle size obtained by this technique was 275±39 nm at room temperature and 216±23 nm at 280 °C, showing a good agreement compared with the *ex-situ* values.

Ultimately, the goal of this work is to develop a technique capable to track on-line the size and concentration of nanoscale particles. For this purpose, sulfidation reaction of iron naphthenate was selected to study the *in-situ* generation of iron based nanoparticles. Particles of 202±33 nm average size were characterized by this technique, finding good agreement with ex-situ characterization of the collected reaction products. Further study of this reaction with the developed technique allowed to determine the temperature on-set for the particle generation at 274.6±0.7 °C.

While simultaneous determination of particle size and concentration was not possible in this work, several modifications of the current design are presented in the end of this manuscript aiming to solve the issues encountered during this work.

ACKNOWLEDGEMENTS

First and foremost I'd like to thank my supervisor, Dr. William McCaffrey for all his support. His supervision and insight guided me through this endeavor. Likewise many thanks to Dr. Manisha Gupta for all the technical discussions and advices she gladly gave me through the conceptual development of this work.

I would also like to thank the Institute for Oil Sands Innovation of the University of Alberta for its technical and financial support; with a special acknowledge to Xiaoli Tan and Brittany Mackinnon for their valuable technical advice and training. I also recognize the support from NanoFab laboratories of the University of Alberta for the training and characterization offered during the project.

I am very grateful for the invaluable contributions of Dr. Cedric Laborde-Boutet and David Dinh to this research. Special thanks also to all of the research group members Samuel Cardozo, Daniel Palys, Geraldine Fournier and Fabian Bender; this experience wouldn't have been the same without all of you.

Finally I would not be here today without the love, patience and encouragement from my friends and family specially my wife, mom, brothers and sisters; your infinite support during this time was my most valuable asset, this achievement is also yours.

TABLE OF CONTENTS

LIST OF FIGURES

LIST OF TABLES

NOMENCLATURE

DLS	Dynamic Light Scattering
DWS	Diffuse Wave Spectroscopy
PCS	Photon correlation spectroscopy
QELS	Quasi-Elastic Light Scattering
ELS	Elastic Light Scattering
IELS	Inelastic Light Scattering
NA	Numerical amplitude
SMA	Subminiature A connector
FC/PC	Fiber-optic connector / physical contact
OD	Outside diameter
DPSS	Diode pump solid-state
TEM	Transmission Electron Microscope
CB	Carbon Lampblack
SDS	Sodium dodecyl sulfate
FeNa	Iron Naphthenate
MeNa	1-Methylnaphthalene
FeNP	Iron based nanoparticles
θ	Scattering angle
φ	Azimuthal angle
θ_a	Fiber optics acceptance cone half angle
ε	Tilt-angle
λ	Wavelength
c	Speed of light
k_0	Incident light wave vector
K_S	Scattered light wave vector
I_0	Incident light intensity
I_S	Scattered light intensity

R_p	Particle radius
D_p	Particle diameter
ACF	Autocorrelation function
$G^2(t)$	Second order autocorrelation function
IACF	Intensity autocorrelation function
$G^1(t)$	First order autocorrelation function
τ	Correlation time
ℓ^*	Particle transport mean free path

Chapter 1: INTRODUCTION

It is well known that fossil fuels supply a large portion of the current world's energy, with liquid petroleum as the source of the majority of transportation fuels. At present, to enhance the profitability of petroleum refining, opportunity oils such as heavy oils are very attractive. Heavy feeds are highly complex and require conversion into lighter products, in a process termed upgrading, before they can be used as feedstocks for conventional refining and petrochemicals processes. Coke precipitation represents a very serious downstream problem when processing these feeds due to the elevated content of polyaromatics molecular chains, and is one of the main areas of study by many researchers.

Observations of thermal cracking processes have led to an understanding of many aspects of mesophase formation, a precursor in the coke formation pathway. One of the features observed is the particle-based behavior of both mesophase and coke, which has encouraged the development of online particle instruments to analyze these important phenomena.[1]

Existing technologies to upgrade heavy oils feeds, such as refineries residues and oil sands bitumen, into synthetic crude oil rely on the use of catalysts to facilitate the conversion. The performance of existing upgraders and refineries can be improved with the use of very small sized catalysts. In the HCAT process, a conditioning unit, to produce molecular size catalyst *in-situ* prior to the reaction with the feedstock, is the key to achieve high conversion with low coke formation downstream of the process. Even though these types of processes are complex and have high catalyst cost due to the continuous consumption of the catalysts precursor, this technology can help existing processes plagued with poor performance achieve competitive conversions. The operating conditions of the conditioning unit responsible for catalyst formation requires delicate control since it impacts, to a very significant extent, the overall efficiency of the process. [2] This work focuses on online particle characterization with the overall goal to optimize this type of processes.

Dynamic light scattering (DLS) has become a mature and useful technology for probing particulate materials either in solution or in suspension. A variety of applications can be found in physical chemistry, colloid chemistry, polymer science, biochemistry and biophysics, medical science, etc., as well as product development and quality inspection in industry. This technique, and many variants developed over the years, is based in the

determination of the particles motion based on estimations of the diffusion coefficient by studying the light scattering behavior of a particulate sample. Information regarding particles size, macromolecular chains conformation, particles interactions among themselves and with the solvent, and slow dynamics such as gelation and vitrification can be obtained from these techniques, to name a few.[3,4]

The main reasons why DLS has been so extensively used in many scientific fields is because it offers a non-invasive characterization technique, requiring very small amount of sample and does not require extensive sample preparation; DLS has matured to the point of the establishment of an international standard (ISO 13321:1996) covering the use of this technique as a certified method for particle size measurement in dilute samples.

Two distinct disadvantages, however, have prevented traditional DLS methods from acquiring acceptance as reliable real time monitoring probes for industrial processes: the first restricts the useful range of concentration of the suspension since the complexity in the interpretation of the measured signal increases with concentration, and the second relates to the need of very sensitive optical alignments, which have caused commercial instruments to have heavy and bulky optical setups.[3,5]

Ultimately the objective of this work is the use of the various dynamic light scattering advances over the years, to overcome the limitations mentioned above and develop a simple fiber optics device capable of monitoring online the evolution of the scattering signal from reactive systems in order to extract information regarding particle size and concentration. Ideally, this measurement will be done at elevated operating conditions of interest for any industrial application.

In the following sections of this manuscript, the basic theory behind this technique is presented along with the design of a fiber optics probe employing two simultaneous laser sources in a backscattering configuration. Following sections contains the assessment of such device with a stable particle dispersion in order to study geometric aspects influenced by the window thickness and material to define the final configuration of the instrument. Beside the geometric configuration of the device, the dispersion systems was also used for validation purposes both at room and elevated temperature by comparing the results obtained by this approach to similar characterizations made with well recognized *ex-situ* techniques. Finally the online observation of a chemical reaction with this device is presented in Chapter 5. Interpretation of the backscattering signal from the *in-situ* generated iron based particles allows the extraction of information

regarding average particle size during the isothermal stage of the reaction. These results serves as proof of the concept for the size characterization of a dynamic system. A number of difficulties in the detection of the signal during the transitional heating stage of the reaction along with the inability to characterize particle concentration of the sample necessitated the redesign of the probe. This redesign is presented at the end of Chapter 5.

Chapter 2: LITERATURE REVIEW

SECTION 2.1. ELECTROMAGNETIC RADIATION: LIGHT

Light is an electromagnetic radiation in the frequency range from approximately 10^{13} Hz (infrared) to 10^{17} Hz (ultraviolet) or the wavelength range from 3 nm to 30000 nm. Visible light is the part of the electromagnetic radiation to which the human eye is sensitive. The wavelength of visible light ranges from 390 nm (violet or purple) to 700 nm (red).[3].

As light propagates in space, it has the characteristics of both a transverse wave as well as a particle (photons). As a wave, light has properties such as frequency, wavelength and interference; as a particle, light has other properties such as momentum, velocity and position.[3]. Light can be used as a non-invasive probe to obtain information about the structure and dynamics of substances based on its interaction with matter. Maxwell's equations form the basis of the description of all electromagnetic phenomena, describing the light oscillations in both space and time.[6].

Light, as well as radio waves and x rays, propagates with electric and magnetic fields oscillating perpendicular to the propagation directions of the wave.[7]. Figure 2.1. shows an illustration of the light wave propagation geometry.

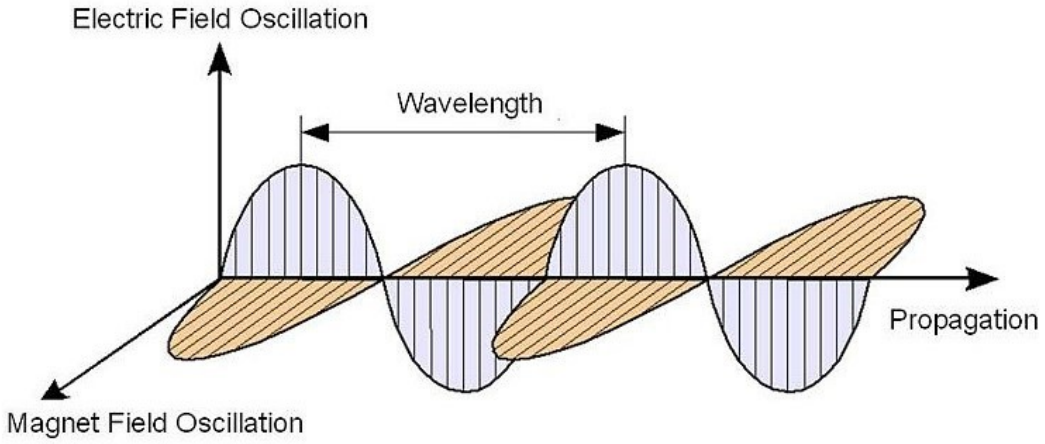

Figure 2.1: Light wave propagation.[8]

The only feature distinguishing these three types of radiation is the frequency of oscillation and, therefore, the wavelength since the frequency v, wavelength λ, and velocity c of an electromagnetic wave in vacuum are related by

$$c = \lambda v. \qquad \text{Eq. 2.1}$$

Light generated from a conventional light source may have the electric field pointing in any direction perpendicular to the direction of propagation at any time. If the direction of the electric field is maintained in only one direction through space and time, then the light it's called to be polarized.[7]

SECTION 2.1.1. LIGHT INTERACTION WITH MATTER

All matter consists of atoms, which themselves are built from negative and positive charges.[9]. When a light beam illuminates a piece of matter having a dielectric constant different from unity, light will be absorbed or scattered, or both, depending on the wavelength of light and the optical properties of the material. The net result of the absorption and scattering caused by the material is known as the extinction of light.[3].

Considering the wave-like properties of the light, the interaction of the electromagnetic waves with a molecule causes a disruption of the spatial charge distribution of the atoms.[9]. As light distorts the charge distribution of the system, radiation is emitted in the form of scattered light.[6]. If there is no exchange of energy between the photons and the system, then the frequency of the scattered light is equal to the frequency of the incident light and the process is referred to as elastic light scattering (ELS). If exchange of energy takes place, the process is referred to as inelastic light scattering (IELS).[6]. Scattering is observed only when a material is in itself heterogeneous, either due to local density fluctuations in the pure material or due to the optical heterogeneity for dispersed particles in a medium. In a perfectly homogeneous material the radiation scattered by individual molecules is isotropic and interferes destructively with the radiation from neighbors, thus no overall scattering is observed.[3].

Scattering, however, is not the only interaction between light and matter. The energy of the incident photon might be absorbed by the system.[6]. The absorbed energy becomes the excitation energy of particles, and will be either thermally dissipated or lost through a radiative decay producing fluorescence or phosphorescence depending on the electronic structure of the material.[3].

The response of a system to an external electric field is called the polarization of the system. The magnitude of the polarization is dependent upon the amplitude of the applied electric field and the ability of the charge distribution to be "deformed" by the external stimulus. The capacity of the system to be distorted is referred to as the polarizability and is represented by the letter α.[6].

Any light-matter interaction, at its most basic, can be broken down into the following components 1) the incident light, 2) the scattering medium, and 3) a detection scheme, as illustrated in Figure. 2.2. showing the incident light of intensity I_0, direction defined by the wave vector k_0 propagating along the X direction. [10]

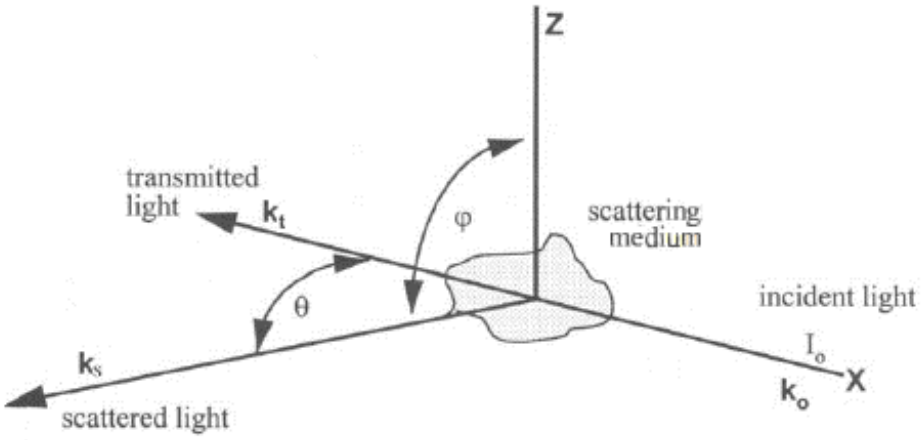

Figure 2.2: Scattering Geometry.[3](modified) (used with permission)

Most of the incident light will be transmitted in the direction of k_t, passing through the scattering volume unless multiple scattering occurs or if the system is highly absorbent. Both the scattering intensity and the intensity fluctuations are a function of scattering direction k_s, relative to the direction of the incident light. Normally, it is specified with the scattering angle θ, formed by the propagation directions of the incident light and scattered light, being 0° for transmission, and the azimuthal angle φ with respect to the Z direction, which unless otherwise stated is assumed to be 90°. In almost all light scattering experiments, both the illuminating light source (polarized or non-polarized) and the detection optics are placed at a distance much larger than the dimension of the particles, thus, both incident and scattered light behave as a plane-wave, making the theoretical description simpler.[3].

Section 2.1.2. Particle Scattering

As mentioned before, the heterogeneities required for the light scattering phenomena to happen may arise from the presence of particles in the medium. Light scattering occurs to a polarizable particle immersed in an electromagnetic field because of the difference in the dielectric properties of the material and the surrounding media, causing an induced oscillating dipole moment releasing radiations of light in all directions. The intensity of the scattered light will be related to the polarization direction of the incident light, scattering angle, and solution parameters.[7]. This phenomenon is the basis for explaining

why emulsions (such as milk) and suspensions can be opaque; and it has been utilized in many areas of science, to measure scattering intensity fluctuations as a function of time as well as time-averaged scattering intensity and phase analysis of scattered light, to determine the particles diffusion coefficient, size, shapes, aggregation/sedimentation, etc. [3,11]

Although the suspension medium also scatters light, the scattering from air or any homogeneous liquid can almost always be neglected when compared with the magnitude of the scattering from the particles.[3]. The volume of material influenced by the electromagnetic field is called scattering volume. This portion of medium is defined by the intersection between the incident beam and the detection cone, and therefore depends on the scattering angle[9]. In Fig. 2.3 the scattering volume, illustrated by the white and black area, is defined by the intersection of the incident light, represented by the dark grey line, and the detectable scattered light, soft grey line.

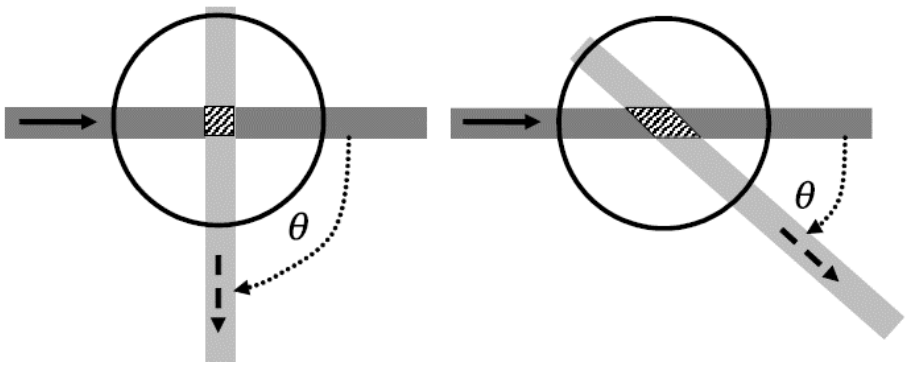

Figure 2.3: Scattering volume dependence on the scattering angle[9] (used with permission)

In the scattering volume, there may be only one particle, as in the case of optical particle counting, or many particles as in many other scattering techniques.[3]. As a consequence, in a light scattering experiment the detected scattered intensity has to be normalized to a constant, scattering angle independent, scattering volume.[9]. The resulting scattering vector, q, is the vector of momentum-transfer between the incident light and the system[3]. The magnitude of q is given by the following equations.

$$|q| = |k_S - k_0| \qquad \text{Eq. 2.2}$$

$$q = \frac{4\pi n_0 \sin\left(\theta/2\right)}{\lambda_0} \qquad \text{Eq. 2.3}$$

Note that the refractive index of the solvent itself n_0 has to be taken into account since it changes the wavelength of the incident light.[9].

Scattering from a unit volume of material that is illuminated by a unit flux of light is a function of the complex refractive index ratio between the material and its surrounding medium along with various other properties of the material. In the same way, the magnitude of the scattering intensity I_S, is inversely proportional to the fourth power of the wavelength λ ($I_s \propto I_0/\lambda^4$),[3]. When more than one particle is responsible for the light scattering (as is usually the case) the scattered light intensity is the square sum the individual electric fields[7], therefore there is a relationship between I_s and the square of the particle volume ($I_s \propto V_p^2$) which translates in a dependence of the scattered intensity to the power of six of the particle size ($I_s \propto R_p^6$).[12].

If there are N particles in volume V, the scattering effect per volume V is N times the effect of individual particles in the absence of interparticle interactions. For concentrated solutions or condensed media where particle-particle interactions must be taken into account, the absolute scattered intensity cannot be estimated in the same way, nevertheless it can still be analyzed from the fluctuation point of view[12].

SECTION 2.1.3. ISOTROPIC AND ANISOTROPIC SCATTERING

Depending on the size of those particles compared with the wavelength of the light very different phenomena occurs, which require individual theories to explain the interactions in each case.[3]

If a particle is much smaller than the wavelength of light, then each part of the particle will experience the same homogeneous electric field (uniform instantaneous phase) of the incident light and light scattered from the particle will be the same in all directions.[3]. In this case the detected intensity of the scattered light depends only on the spatial arrangement of the scattering centers and not the direction at which the scattered light is detected. This type of scattering is referred to as Rayleigh-Gans-Debye scattering.[6].

For larger scattering particles, the scattered intensity is no longer independent of the scattering angle.[9]. In this case the relative magnitude and phase of the electric field are altered by each scattering center, then the characteristics of the electric field are dependent upon its location within the particle. This type of scattering is referred to as Mie scattering.[6]. In the Mie-regime the dependence of the scattering intensity and particle size becomes non-trivial and overall the increase of the scattering intensity with particle size is less pronounced.[13]. Given that the ultimate objective of this work is to apply the developed technique in the in-situ catalyst generation, which are under the

Rayleigh domain, this study treats the particles with the Rayleigh approximation to study the accuracy of this theory.

Static light scattering rely on time-averaged scattering intensity assuming that the entire system is in some static condition: the scatterers are not moving, the incident intensity is constant from a stable light source, and there is no relative movement between the components of experimental setup. In reality, however, although the incident light intensity I_0 can be maintained at a constant level and the instrument can be made rigid, particles in the scattering volume are in constant movement.[3]

The movement can arise from random thermal motions (Brownian motion), forced motion introduced by a flow or electric field; or even motion arising from bioactivity such as the mobility of bacteria particles in water. Any motion of the particles will cause temporal changes or fluctuations in scattering intensity which may be fast or slow, depending on the nature of the motion and the type of particle.[3] Given that the multiple particles in motion causes the changes in the scattered light intensity, information regarding the mutual diffusion coefficient and hence the equivalent hydrodynamic radius may be obtained by analyzing the temporal behavior of the intensity.[6]

SECTION 2.1.4. CONCENTRATION AND PARTICLE-PARTICLE INTERACTIONS

The presence of multiple particles in the scattering volume has the effect of introducing faster components to the decay process. It is possible that a single photon may be scattered by more than one particle, or multiple scattering within one particle, before it finds its way to the photodetector. The effect of multiple scattering is to introduce a broader distribution of wave vector components into the view of the photodetector.[6]

Generally, there are two regions in which the contributions from each individual particle to the overall scattering pattern are different. In one region, when the number of particles is small and there is a large separation between the particles, multiple scattering can be neglected. Physical forces along with scattering interference between particles may be still present but have only a limited effect on the overall scattering pattern. In the other region, the number density of particles is high enough so that these particles are in close proximity, and several other phenomena may occur. There is, however, no clear borderline between these two regions since effects produced by an increase in concentration appear only gradually, and depends highly in the nature of the particles.[3]

With high particle density systems, some of the radiation scattered by a particular particle will be incident upon a second particle, which then re-scatters the radiation. The re-scattered light from the second particle may become the incident light upon a third particle, which then re-scatters; and so on. This phenomena is called multiple scattering. When particles are close enough to each other, physical interactions between them will take place and scattering from any particle will again be affected by the existence of its neighbors. In a high concentration environment multiple scattering, mutual polarization and strong interference between particles, all of which are heavily dependent on the morphology, dimension and nature of the particles; will interfere in the detection plane. Therefore, information retrieval about the characteristics of the particles from a time-averaged intensity measurement is a very difficult task in a concentrated particle medium.[3]

SECTION 2.2. DYNAMIC LIGHT SCATTERING (DLS)

One of the difficulties in obtaining reliable experimental data at high concentrations is the effect of multiple scattering in the detected signal[6]. Conventional methods, however, can be used to study the concentration dependence of the mutual diffusion coefficient with the implementation of sophisticated techniques to avoid or suppress the multiple scattering influence in the measure of single scattering events. The complete opposite approach is to measure the temporal fluctuations of the light in a highly concentrated system and use the multiple scattering properties to interpret the physics of the particles. In any case the measured diffusion coefficient is not and cannot be related directly to a single particle property, in any case the diffusion coefficient is the result of particle movement constrained by particle-particle interactions and spatial effects.[3]

In any dynamic light scattering experiment, except photon migration spectroscopy, the intensity of the incident light is constant and the relative positions of the instrument components remain unchanged. Therefore the source of the intensity variation arise purely from the movement of the particles, thus detecting intensity variations can provide information on the motions and the characteristics of the particles.[3]. A single spherical symmetric object in a homogeneous light field will scatter light with constant intensity, and hence will not produce temporal intensity fluctuations, therefore, the short-term intensity fluctuations of the scattered light arise from the fact that the scattering particles are in motion such as diffusive Brownian motion, own motion, (living microorganisms) or particle motion under external force.[11, 14]

Various terms have been used for this phenomenon: dynamic light scattering (DLS), photon correlation spectroscopy (PCS), quasi-elastic light scattering (QELS), spectroscopy of optical displacement, laser correlation spectroscopy and others. In any case, the pace of the movement is inversely proportional to the particle size (the smaller the particles are, the faster their motion or diffusion), and quantitative estimation of the motion can be detected by analyzing the time dependency of the light intensity fluctuations scattered from the particles when they are illuminated with a coherent light source. [11]

The common aim of all DLS techniques is the statistical analysis, often in terms of autocorrelation, of the temporal variations in the scattered light intensity for the purpose of characterizing the motion of a dynamic system. Making the DLS technique, and its variants, a very powerful characterization tool that has been applied in many areas of science and industry.[10]

The first fully implemented DLS has its origins as a quantitative technique in the 1960s, when the advent of the laser and development of higher sensitivity photo-detectors made possible the measurement of the remarkably fast fluctuations of the scattered light and extremely low signal levels compared with the previously available technology. The continuous development from both a theoretical and technical point of view of QELS served to pave the way for a number of other DLS techniques, such as diffusing wave spectroscopy (DWS). [10,11]

The theory behind QELS is based on a number of key assumptions that restrict the range of industrial applications of this techniques, where high concentration of particles and highly absorbent mediums are present. The basis for the "quasi-elastic" assumption, however, is met in most systems where the wavelength (and frequency) of the scattered photons are essentially the same before and after scattering. When this assumptions is met, statistical analysis of the scattered light can be directly related to the diffusive motion of the particles, which is known to be a function of particle size, temperature and viscosity of the medium.[10]

The intensity fluctuations described by the DLS are not usually observed because they take place on a time scale much faster than many photometers, including the human eye. The time required for the fluctuations to take place is inversely related to the particle radius. Based on this relationship it is expected that a large particle will have a smaller diffusion constant than a small molecule and therefore the fluctuations will take place more slowly.[7]

SECTION 2.2.1. GENERALITIES

Due to the stochastic nature of the light scattered from a dynamic system, a large number of fluctuations must be analyzed in order to obtain a statistically reliable measure of dynamic behavior. Therefore DLS as a technique is only suited to study systems exhibiting changes in the particle motion that occur more than three orders of magnitude slower than the maximum detection time-scale of the signal.[10]

Under some circumstances vibrations in various parts of the apparatus or of one part with respect to another can cause severe intensity fluctuations at the detector, representing an important factor in the experimental setup design. Convection currents in a cell can lead to a substantial contribution to the signal fluctuation. Temperature control of the sample is commonly incorporated given that the light source may introduce local temperature gradients, even more in the case of highly absorbent systems.[7]

Generally speaking, the lower size limit of this type of measurement is determined by the detectable scattering fluctuations of particles. The measured scattering fluctuations must be faster than the motion of the particles in order to obtain an unbiased result. The upper size limit of these measurements is determined primarily by the sedimentation limit. Particles that are being analyzed must be stably suspended. Sedimenting particles leave the scattering volume and undergo directional motion that add a degree of complexity to the interpretation of the scattering fluctuations.[3]

SECTION 2.2.2. ELECTRIC FIELD AND INTENSITY CORRELATION FUNCTIONS

It is known that the light scattering is a random process; therefore, essential information can be extracted from the data by using statistical methods. The simplest characteristic is its mean value, however, the mean value of the complex amplitude of the scattered electromagnetic field does not contain any useful information. More complex characteristic of a random process is the correlation function, which is the product average of the variable value for two different times t_1 and t_2. [11]

$$G(t) = \{f(t_1)f(t_2)\} \qquad \text{Eq. 2.4}$$

In light scattering, the variable may be either the electric field, in which case is called first-order correlation function ($G^1(t)$); or the intensity, second-order correlation function

($G^2(t)$).[3]. Given that the detectable quantity in these experiments is intensity, the time-correlation function of interest in these analysis, and is defined as.

$$G^2(\tau) = \int_0^\infty I(t)J(t+\tau)\,dt \qquad \text{Eq. 2.5}$$

Where I(t) and J(t+τ) corresponds to individual intensity measurements separated by a time scale. $G^2(t)$ is called the autocorrelation function or cross-correlation function depending on whether I(t) and J(t) are the same or different signals, respectively.

The correlation function has two features that are of particular interest for this technique. First, it is easily measured, using modern digital techniques for light signals of very low levels; and second, it can be shown to be the Fourier transform of the power spectrum which allows to establish relationships with the diffusion coefficients of the particles to extract useful information of the dynamics of the system.[7]

The time shift τ is often referred as the delay time, since it represents delay between the 'original' and the 'delayed' signal. The intensity correlation function cannot be continuously measured, instead it can be evaluated in discrete time intervals Δt points obtained by a summation over the duration of the experiment, thus the full extent of the measure is given by T=N*Δt while a particular time during the measurement t_n=n*Δt. [9,11]. Figure 2.4. shows an illustration of a measured intensity fluctuation and how the analysis of the autocorrelation function is applied to the signal.

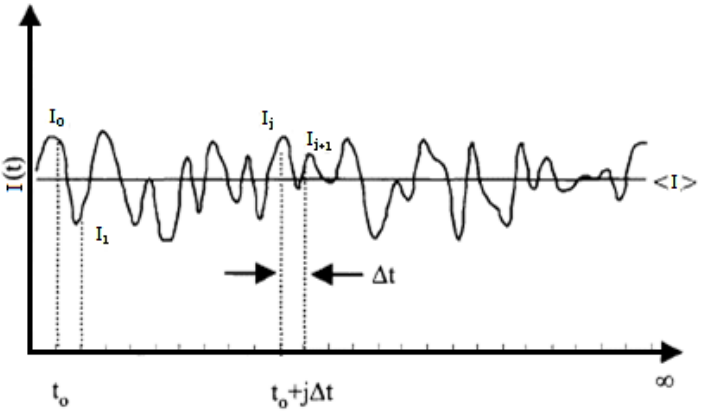

Figure 2.4: Intensity fluctuation analysis.[3](modified) (used with permission)

For static light scattering experiments, the average scattered intensity <I(t)> and the value is as indicated in the figure, is the measurable quantity. For dynamic light scattering, on the other hand, the detailed analysis of the fluctuating intensity I(t) is important, obtained from the discrete analysis of the measurement as follow:

$$G^2(\tau_k) = \sum_{n=0}^{t-\tau_k} I(t_n)I(t_n + \tau_k) \qquad \text{Eq. 2.6}$$

The physical meaning of the ACF is that, since the measurement at time (t+τ) occurs right after the measurement at time t, the signal or information contained in the measured values from these two measurements should be somehow related (correlated) if is small. The larger the value of τ the further away the system at time (t+τ) is from its original state at time t. When the delay time τ goes to infinity, the two states become completely uncorrelated.[3]

The statistical evaluation of the correlation function provides the ideal limits of the function as follow

$$\langle I(t) * I(t+\tau)\rangle \;\rightarrow\; \langle |I(t)|\text{^}2 \rangle \quad , \quad \tau \rightarrow 0 \qquad \text{Eq. 2.7}$$

$$\langle I(t) * I(t+\tau)\rangle \;\rightarrow\; \langle I(t)\rangle\text{^}2 \quad , \quad \tau \rightarrow \infty \qquad \text{Eq. 2.8}$$

Since $\langle |I(t)|\text{^}2 \rangle \geq \langle I(t)\rangle\text{^}2$ the ACF has a maximum at τ=0 and either remains constant or decays to the ⟨I(t)⟩^2 at sufficiently large τ, as shown in Figure 2.5. The form of decay depends on the nature of the variable I(t). [12]

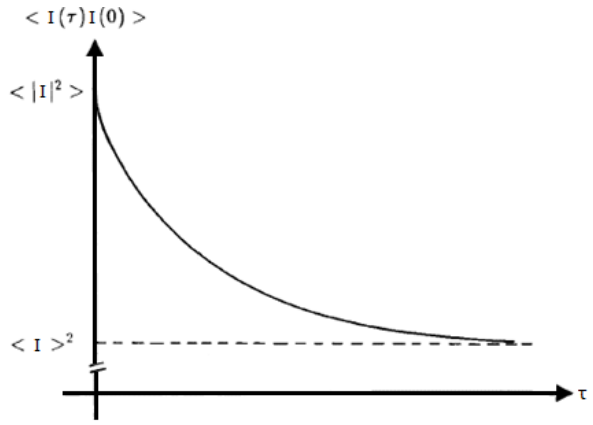

Figure 2.5: Ideal behavior of the correlation function.[12](modified) (used with permission)

The field correlation, however, is the function that contains all information concerning the motion of the scattering solute particle. In general, $G^2(t)$, however, is not simply related to $G^1(t)$. In the case when the incident light is described by a Gaussian function, these two ACF's are related by the Siegert relation, [3] as follow:

$$G^2{}_{(\tau)} = \langle I_s \rangle^2 + \left|G^1{}_{(\tau)}\right|^2 \qquad \text{Eq. 2.9}$$

The normalized form of all the previous equations are obtained by dividing by the variance of the function which can be estimated as the average autocorrelation value given by $<I(t)>^2$, obtaining the following normalized equation:

$$g^2{}_{(\tau)} = 1 + \left|g^1{}_{(\tau)}\right|^2 \qquad \text{Eq. 2.10}$$

And in the discrete form

$$g^2(\tau_k) = \frac{\sum_{n=0}^{t-\tau_k} I(t_n) I(t_n+\tau_k)}{\left[\frac{\sum_{n=0}^{t-\tau_k} I(t_n)}{N}\right]^2} \qquad \text{Eq. 2.11}$$

The above equation however comprises the ideal scenario where the detection area is exactly the same as the coherence area of the sample shined by the incident light, therefore for more realistic scenarios, an efficiency factor β is included in the to account for the real photon collection system

$$g^2{}_{(\tau)} = 1 + \beta \left|g^1{}_{(\tau)}\right|^2 \qquad \text{Eq. 2.12}$$

The ideal field correlation function in its normalized form corresponds to the diffusion of 'hypothetical' identical diffusing spheres [7,11]

Section 2.2.3. Heterodyne and Homodyne detection

Detection of the scattered light can be arranged in two different ways: Heterodyne and Homodyne. In a heterodyne arrangement, light directly from the source is simultaneously detected along with the scattered light; while in a homodyne arrangement only the scattered light is directed into the detector. Figure 2.6. shows a diagram of both arrangements. [11]

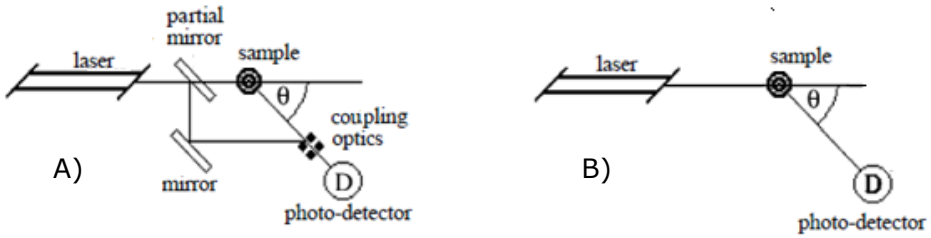

Figure 2.6: Scattering configuration A) Heterodyne B) Homodyne.[11] (used with permission)

Both configurations have been used extensively for different samples with no significant difference between the two besides the homodyne detection being simpler than heterodyne and not requiring continuous readjustment. The overall signal-to-noise ratio in each case is relative to how low the intensity detection is expected, since in heterodyne detection a significant portion of the total intensity is the raw incident light, the intensity fluctuations are shifted to higher magnitudes where detectors have better signal to noise performance. In cases where the scattering intensity is high enough, homodyne

detection tends to be more accurate since fluctuations coming from the light source are not directly detected.[11]

SECTION 2.2.4. DIFFUSE WAVE SPECTROSCOPY (DWS)

As mentioned before, one approach to study the intensity fluctuations of highly concentrated system is by the use of a multiple scattering limit, this approach is known as Diffusing Wave Spectroscopy (DWS). Originally introduced in 1987 the technique is very similar to conventional DLS, relatively simple to apply and it provides accurate information about local displacements in highly turbid media. Compared to standard DLS, DWS works in the opposite regime where the long multiple scattering path in the medium causes a large N number of scattering events. This implies that very small displacements, of the order of $\lambda/\sqrt{N}$ are sufficient to induce light fluctuations, with typical values for $\lambda/\sqrt{N}$ can lie in the sub-nanometer range and this makes DWS a much more sensitive technique as compared to conventional DLS. [15]

DWS requires assumptions on the statistics of photon paths in the medium, in the case of very strong multiple scattering in which the light is scattered a very large number of times in random scattering events promoting the diffusive propagation of photons in the medium. This process can be described by the diffusion approximation that neglects any interference effects of the light and assumes that the light intensity diffuses implying that individual scattering events play a less critical role in the overall scattering intensity. Because of these fundamental approximations, DWS can only be applied to samples with very strong scattering.[3]. It is clear that also in this case the main limiting factor is the penetration length in the sample. The light traveling long paths in the sample can be strongly attenuated and the characterization of the tails of the path length distribution can become difficult. [15]

Before the development of DWS there were numerous attempts focused on suppressing the contribution of multiple scattered light. The success of these techniques rely on the fact that a significant fraction of the detected scattered light has been scattered just once. By contrast, DWS requires strongly multiply scattered systems, thus extends the application of conventional DLS to highly concentrated, essentially opaque, samples in which the overall scattering is completely dominated by multiple scattering events.[16]

Many similarities are shared between DWS and conventional DLS, both techniques consist of measuring the temporal intensity fluctuations of the scattered light; in both cases these fluctuations reflect the dynamics of the scattering medium and both

techniques rely on statistical tools to calculate the temporal correlation functions. Because their similarity, DWS can use the same instrument as in a conventional DLS experiment to measure the light intensity fluctuations, except that a much stronger laser is needed because of the diffusing light over a much longer path length, moreover in the transmission configuration. [3,17]

The diffusive propagation of the light assumed in DWS, however, leads to correlation functions highly dependent on the experimental geometry. Only by properly defining the experimental conditions, it is possible to quantitatively analyze the dynamics of the particles. The light path in the medium has to be arranged so that only completely randomized diffusing light is detected. Back-scattering and transmission (180° or 0° scattering angles) are two convenient setups for a DWS experiment that have simple theoretical formulations. Since the diffusing light leaves the sample with nearly uniform intensity in all directions, the exact angle of detection becomes less critical than in conventional DLS. Other studies have proof no significant change in the measurements by varying ±20° the scattering angle. [3,16,17]

As mentioned before, for scatterers much smaller than λ, the scattering from each particle is isotropic and the direction of the light propagation is randomized over a distance ℓ through the medium. Therefore the transport of the light energy density, U(r, t), can be described over length scales longer than ℓ by the diffusion equation[16]

$$\frac{\partial}{\partial t} U(r,t) = D_\ell \nabla^2 U(r,t) \qquad \text{Eq. 2.13}$$

Where D_ℓ is the diffusion coefficient of the light in the medium. Then

$$D_\ell = c_\ell/3 \qquad \text{Eq. 2.14}$$

Where c_ℓ is the light speed in the medium. For particles which are not small compared to λ, the scattering is anisotropic, and the mean number of scattering events required to randomize the direction of light propagation is greater than in the previous case. Therefore the length scale over which the randomization of the light propagation occurs is defined by $\ell^* = n_0 * \ell$ (transport mean free path). Given that n_0>1 for particles considerably bigger than the wavelength of the light, the diffusion equation is valid only over length scales longer than ℓ^*. In practice, this means that the theory for DWS based on the diffusion approximation of the light will provide an accurate description of the temporal fluctuations of the scattered light only when the sample under study is greater

than ℓ^* and the distance that photons travel through the sample is much greater than ℓ^*, regardless of the particle size compared with the light wavelength.[16]

SECTION 2.2.5. GEOMETRY DEPENDENCE OF DWS

As mentioned before, the diffuse light propagation approximation of this technique causes a high geometry dependence of the theoretical approach. The following Figures 2.7. and 2.8. shows the scattering geometry and the detected intensity from a light pulse for transmission and backscattering configuration, respectively.

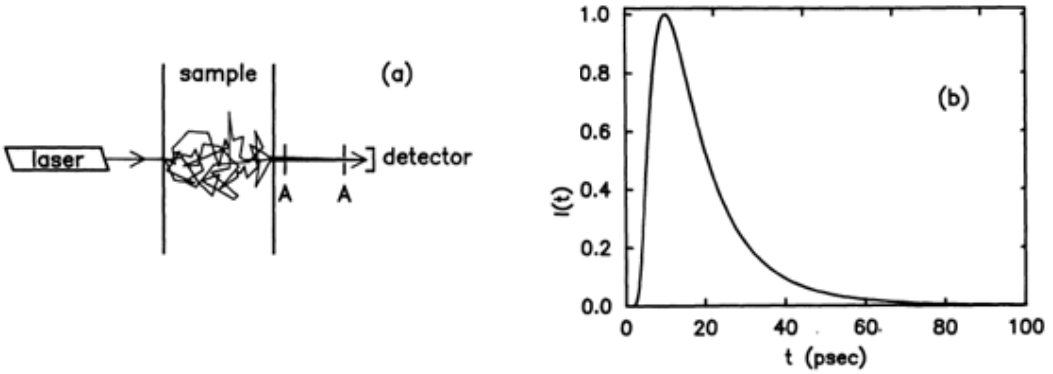

Figure 2.7: DWS Transmission configuration, a) Geometry, b) Detection.[16](modified)

(used with permission)

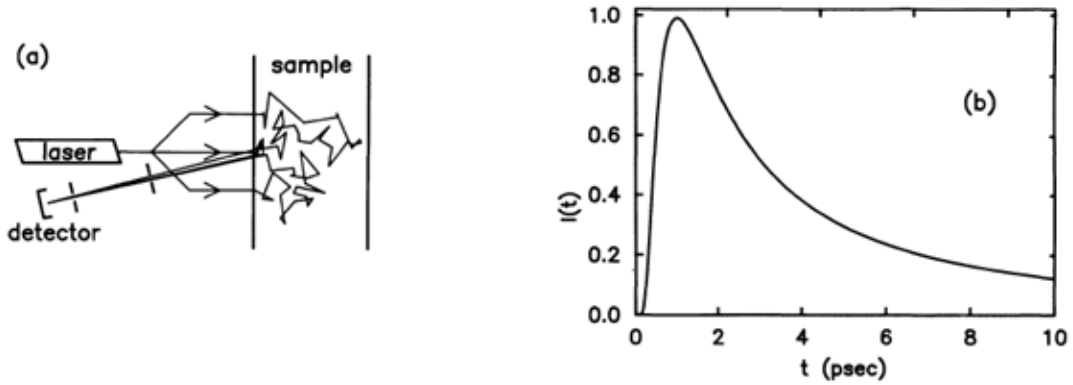

Figure 2.8: DWS Backscattering configuration, a) Geometry, b) Detection.[16](modified)

(used with permission)

In Transmission, the light has to travel through the whole scattering volume before is detected, in this path a much larger number of scattering events happen compared with the backscattering configuration. This behavior is the main reason why in Figure 2.7., in contrast to backscattering Figure 2.8., the average time that takes the light to reach the detector is much longer and its distribution is well-defined by the sample thickness. The

time scale in Figure 2.8. for the backscattering configuration shows a much faster detection time scale and much broader detection distribution, in fact, since paths of all lengths contribute in backscattering, the detection consists of contributions from all orders of multiple scattering. Since the light exits from the same face of the sample, longer paths consist of a larger number of scattering events and thus decay more rapidly, by contrast shorter paths consist of a smaller number of scattering events thus decaying more slowly and allowing to track the motion of individual particles over longer length and time scales. This feature is particularly advantageous from the backscattering configuration to analyze the dynamics of interacting systems, which can have a broad distribution of relaxation rates associated with motion over different lengths scales.[16]

Considering backscattering detection of a system of non-interacting spherical particles the electric Fourier transform of the field correlation function can be written as [18]

$$g^1{}_{(\tau)} \propto \int_0^\infty P(s)\, e^{\left[-(2\tau/\tau_0)(s/\ell^*)\right]} ds \qquad \text{Eq. 2.15}$$

Where P(s) is the probability that the light travels a path of length s, τ is the delay time and τ_0 the characteristic diffusion time. Physically, Eq. 2.15. reflects the fact that paths of "s" diffusion length corresponds to a random walk of s/ℓ^* steps and $g^1{}_{(\tau)}$ decays, on average, $e^{2\tau/\tau_0}$ per step. Thus $g^1{}_{(\tau)}$ contains a wide distribution of decay times, with the most rapid decay times coming from the longest paths.[18]

It is important to set a boundary conditions for the analysis of this expression: considering the backscattering geometry allowing $s<\ell^*$ leads to unphysically long decay times since $s=\ell^*$ represents the shortest decay time possible, corresponding to singly scattered light. Therefore the contribution of the unphysically short paths needs to be suppressed by changing the lower limit of the integral for $s=\ell^*$.[16]

The key to solve the above equations relies on the determination of P(s), which as explained before will depend in the experimental geometry. Maintaining an extended plane-wave detection, the incident light interacts with the front face of a sample volume of thickness L (the depth of the medium) in the backscattering configuration, and an effectively infinite lateral extent can be considered compared with the size of the illumination/detection optics. Under this experimental geometry constraints, the electric field correlation function for the multi-scattered light can be written as[18]

$$g^1{}_{(t)} = \frac{1}{\left(1-\gamma\,\ell^*/L\right)} \frac{\sinh\left[\left(L/\ell^*\right)\left(6\tau/\tau_0\right)^{1/2}\left(1-\gamma\,\ell^*/L\right)\right]}{\sinh\left[\left(L/\ell^*\right)\left(6\tau/\tau_0\right)^{1/2}\right]} \qquad \text{Eq. 2.16}$$

Again ℓ^* is the diffusive mean free path for light in the system, the length scale over which the direction of light propagation is randomized, and the parameter γ is introduced as a multiplicative factor to locate the conversion point within the sample at which the passage of light can be considered diffusive, providing a physically meaningful boundary condition to permit analytical solution of the diffusion equation.[17]

Given that experimentally, a sample thickness L is greater than ℓ^* is always required to obtain accurate results, then the above equation can be simplified to[17]

$$g^1{}_{(t)} \approx e^{-\gamma\sqrt{6\tau/\tau_0}} \qquad \text{for} \qquad L \gg \ell^* \qquad \text{Eq. 2.17}$$

Given the proportionality that Eq.2.17 shows between the first order autocorrelation function ($g^1(\tau)$) and the correlation time (τ), at τ→ 0 the slope is infinite and there is no dependence on ℓ^* for an infinitely thick sample.[17]

It is emphasized that in backscattering, in contrast to the case of transmission, $g^1(\tau)$ contains contributions from paths of all lengths, therefore is very sensitive to the details of how the propagating light is converted to diffusing light in the first several scattering events. The simplest approximation consist in assuming that the conversion occurs at a single distance, $\gamma\ell^*$, into the sample. The actual conversion process is considerably more complex and other approximations can lead to substantially different results, however, this approximation has shown very good agreement in various experimental conditions regardless its simplicity. [17]

For illustrative purposes figure 2.9. shows a general result of an autocorrelation function measured in backscattering geometry.

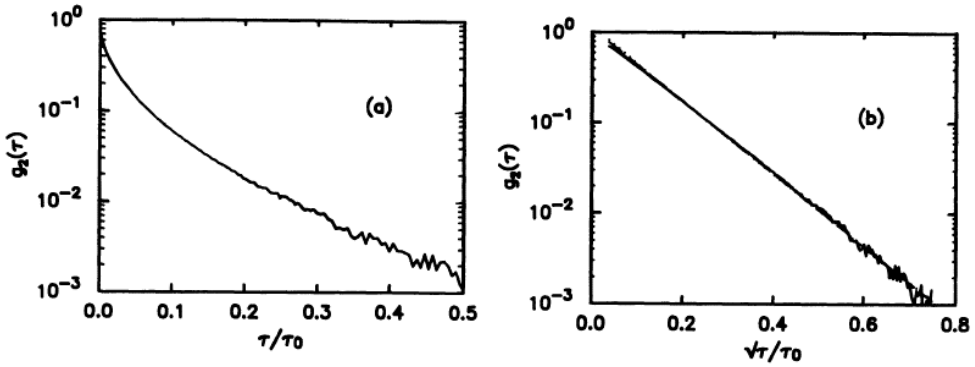

Figure 2.9: ACF for DWS in backscattering configuration.[16] (used with permission)

In Figure 2.9. A) The large amount of curvature exhibited by the plot of $g^1(t)$ vs τ reflects the expected contributions of a wide range of paths length scales. In Figure 2.9. B) is

clearly observed the linear dependence of $\ln[g^1(\tau)]$ with $\tau^{1/2}$ at early values. At later decay times, however, there is a slight deviation characteristic of these systems where the contribution of the longer decay times is still observed.[16]

SECTION 2.2.6. ABSORPTION

In any physical system there will always be absorption of light, either by the scatterers themselves or by the solvent in which they are suspended. Furthermore, the effects of absorption will be enhanced in the multiple scattering limit because the path lengths of the light and the number of scattering events are greatly increased.[16]. The presence of the absorption by either the solvent or the scatterers, causes two mayor phenomena: it would lead to local heating of the scattering volume, thus affecting the diffusion of the particles in the medium[6]; and attenuating the intensity of light travelling a path of length "s" exponentially by a factor exp $(-{}^{s}/_{\ell_a})$, where ℓ_a is the ''effective'' absorption length.[13].

Thus Eq. 2.15 becomes:

$$g^1{}_{(\tau)} = I_0 \int_0^\infty P(s)\, e^{\left[(-s/\ell_a)-(2\tau/\tau_0)\left(s/\ell^*\right)\right]} ds \qquad \text{Eq. 2.18}$$

Since both terms in the exponent are linear in s, the effect of the absorption is mathematically the same as shifting the time scale. Thus all of our previous analysis is directly applicable considering the substitution:

$$\tau/\tau_0 \rightarrow {}^{\ell^*}/_{2\ell_a} + \tau/\tau_0 \qquad \text{Eq. 2.19}$$

Obtaining a simplified autocorrelation function, similarly as Eq. 2.17, as follow:

$$g^1{}_{(t)} = e^{-\gamma\sqrt{6\tau/\tau_0 + 3\ell^*/\ell_a}} \quad \text{for} \quad L \gg \ell^* \qquad \text{Eq. 2.20}$$

Considering the above equation, absorption will significantly affect the decay of the autocorrelation function only for time scales less than $\left({}^{\ell^*}/_{2\ell_a}\right)\tau_0$.[16]

Physically, the effect of the absorption is to reduce the contribution of the longer paths to the decay of the autocorrelation function. These paths would otherwise contribute a rapid, initial decay of the correlation function, by deviating the correlation function at early times. In light of this analysis, systems where particles may exhibit strong absorption adds some complexity to the interpretation of the measurements[13], significantly more profound in the case of transmission configuration where the already long path of the propagating light is lengthen even further. In practice, however, when the absorption is sufficiently strong to significantly alter the autocorrelation function, the

entire transmitted intensity will be so strongly attenuated and signal levels are so low that measurements are usually unfeasible.[16]

SECTION 2.2.7. POLYDISPERSITY

In many cases of interest, the scattering medium will consist of a distribution of species with different optical properties and different diffusion coefficients. Most often, this situation arises when there is a distribution of particle sizes. In the case of conventional dynamic light scattering, this leads to a non-exponential decay of the autocorrelation function. In the case of strong multiple scattering, the non-exponential decay of the autocorrelation function and the geometry dependent makes the polydispersity effect more difficult to discern from the data than in DLS. This effect can be predicted by exploiting the diffusive nature of the light transport.[16]

For a polydisperse system the scattering from different size particles leads to phase shifts of different average magnitude resulting from the dependence of $<q^2>$; and a particular D related to individual particle size. This results in a random walk with different step sizes. Even though the shape of the autocorrelation function should remain the same for a polydisperse system as for a monodisperse system, there is no additional information concerning polydispersity available from DWS measurements in contrast to DLS when a particle size distribution can be obtained. This technique is only capable to give information of average properties. Nevertheless, the average quantities can be calculated for a particular particle size distribution and therefore the effect of different distributions can still be measured. [3,16]

SECTION 2.2.8. SIZING

Plotting $\ln\left[g^1{}_{(t)}\right]$ as a function of $\sqrt{\tau}$, from Eq 2.17 is expected to obtain a straight line, which slope corresponds to $\gamma\sqrt{{}^{6}/_{\tau_0}}$. Where

$$\tau_0 = {}^{1}/_{D_0 q^2} \qquad \text{Eq. 2.21}$$

Being D_0 the defined by the single particle diffusion coefficient and q the scattered light wave resulting vector related to λ, the wavelength of light in the medium.

Hence if $g^1(t)$ is a constant it is then possible to determine the (average) short time single particle diffusion constant of Brownian particles from the decay time τ_0. From this expression the particle size can be calculated using the Stokes–Einstein relation for spherical particles as follow:

$$D_0 = \frac{2*K_B*T}{6*\pi*\eta_{(T)}*d} \qquad \text{Eq. 2.22}$$

For a backscattering measurement, the determination of γ must be done independently. However, more limited information is available for particle sizing with DWS as compared to conventional DLS. For example, as shown above, no information concerning particle size polydispersity can be obtained from DWS, whereas the determination of particle size distributions is a well-developed feature of DLS. When multiple scattering impedes the use of DLS, DWS holds the potential for giving at least information regarding average particle size.[16]

Each geometry configuration for DWS has its own merits. The advantages of backscattering are its simplicity in that only one optical access to the sample is required. Furthermore the shape of the autocorrelation function in backscattering can provide considerable additional information: curvature in the shape indicates the presence of either absorption, for downward curvature at early times, or particle interactions, for upward curvature at later times.[18]

SECTION 2.3. PRACTICAL CONSIDERATIONS

Although DLS, and its variants, has increased its acceptance as a reliable characterization technique, most of the advances in the last years have been brought by technological advances in the emission and detection aspect of the technique. The invention of the laser and fiber optics, particularly, has conferred simplicity, versatility and compactness to the initial setups, increasing the application of the theoretical interpretation of the signal.

SECTION 2.3.1. LASER LIGHT

As mentioned before, the light source required for this kind of measurements need to be coherent. Because of its high coherence, monochromaticity, linear polarization, etc. laser light is the main light source used in DLS experiments.[3]. The word "laser" is the acronym for “light amplification by stimulated emission of radiation”, and is present in a version of the technique name (Laser Light Scattering) emphasizing its essential role in obtaining effective signal measurements.[12]

In terms of Fourier optics each detectable signal of scattered light is the superposition of multiple waves propagating at as many angle as the detection optics can perceive, therefore the elasticity of the scattering event is facilitated by maintaining coherence of

the light source.[19]. Given that the signal analysis of a DLS technique is based on the scattering fluctuations, variations inherent to the light source greatly impacts the interpretation of the signal.

In selecting a laser there are four factors that must be taken into consideration: stability, polarization, wavelength and output power. The first factor enters in a negative sense: any fluctuations in laser power should be avoided, if at all, since will affect the motion detection of the particles. The polarization aspect of the incident light is a determining factor in the scattering intensity, therefore it is essential that the incident light is polarized. The following two factors are coupled because the power required to achieve a given signal-to-noise ratio depends on the wavelength, in general the scattering power is proportional to $1/\lambda^4$ therefore it is preferable to use smaller wavelength if low light levels are anticipated to obtain better photomultiplier efficiency. The wavelength to be selected is governed by the nature of the sample to be analyze: the first requirement is that no, or little, absorption is promoted in the sample, otherwise local heating of the sample will substantially arise leading to convective flow of the solution. Similarly, it is undesirable to excite fluorescence in the sample, although unwanted light from this source could be removed with filters it may cause additional changes in the sample. Beyond these requirements there is relatively little scientific reason to choose one wavelength over another. [7]

Section 2.3.2. Scattering with Fiber optics

In a concentrated opaque suspension, the incident light intensity diminishes rapidly as it propagates through the scattering volume due to strong multiple scattering. In these situations, measuring the light scattering from a thin layer of sample becomes the best choice in order to maintain detectable signal intensities and useful signal to noise ratio. Without special effort involved in making an extra thin cell, using an optode (an optical fiber probe) in a backscattering configuration allows to selectively measure the scattering from a few layers of particles near the incident light, offering miniaturization almost impossible using conventional optics.[3]

If a fiber is used directly to collect the scattered light without additional optical elements at the end of the optode, then the scattering angle θ will depend on the maximum acceptance half cone angle of the fiber. The acceptance cone propagation is illustrated in Figure 2.10, and is mainly related to the refractive index difference between the fiber core and cladding.[3]

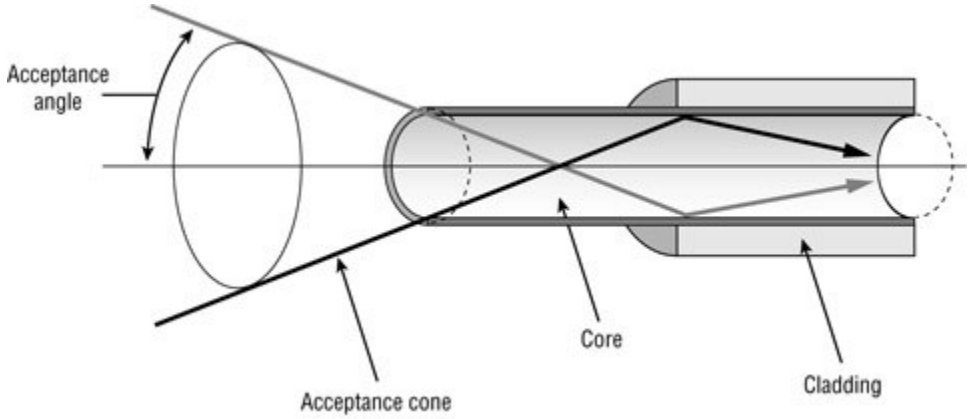

Figure 2.10: Fiber optics acceptance cone.[20]

Quantitatively, this angle is estimated by the following expression

$$n_0 \sin \theta_{max} = \sqrt{{n_{core}}^2 - {n_{clad}}^2} = NA \qquad \text{Eq. 2.23}$$

Where n_0 is the refractive index of the propagating medium. Commercially, a dimensionless number called Numerical Aperture (NA) characterizes the maximum acceptance cone angle over which a fiber optic can transmit or receive light. Typical values for monomode fibers in air are around 4.7° while the angle grows up to 9° for multimode fibers.[3]

One fiber optic is capable of both transmitting the incident light and detecting the scattered light, however a directional coupler is required to merge the two fibers in one end to connect both the light source and detector. This arrangement, while reducing the space of the optode, also introduces the detection of raw light sources reflected in the fiber termination. The face of the fiber in this case acts as a local oscillator introducing a baseline intensity relative to the difference in refractive index of the fiber core and the medium, making the homodyne detection particularly challenging for single fiber optodes. Transport of the incident and scattered lights, can also be carried out separately by two individual fibers, defining the scattering volume by the intersection of the two individual fiber optics acceptance cones. While the scattering volume adopts more complex shapes in this case, it can be adjusted by controlling the angle and the spacing between the two fibers, conferring more geometric versatility to this arrangement in sacrifice of smaller optode size.[3]

Figure 2.11. illustrates both single and multi-fiber arrangements

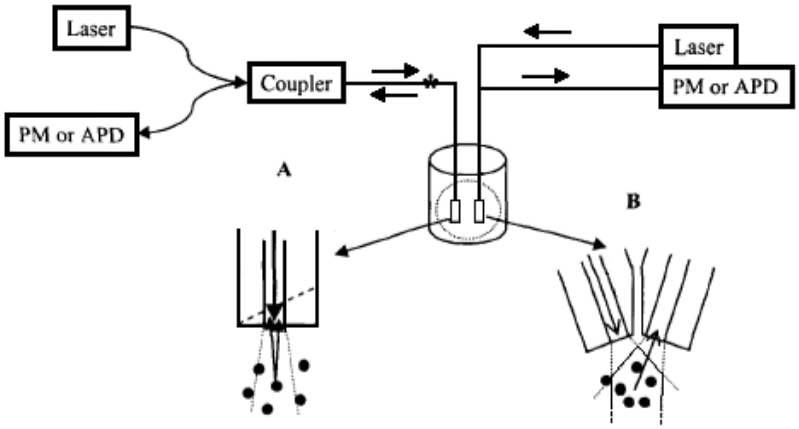

Figure 2.11: Fiber optics arrangements.[3] (used with permission)

Optical fibers are basically incoherent, in other words the coherence properties of the wave entering in one end of the fiber does not corresponds to the coherence properties of the light emanating from the other end of the fiber. In terms of the previously explained NA is that light entering one end of the fiber, at any angle, will always exits at the other end of the fiber at the full numerical aperture. There is, however, a range of angles in which the entering light will not suffer significant attenuation throughout the fiber, known as the coherence angle $(\Delta\theta)_{coh}$; which is a function of the scattering volume and the scattering angle θ. Figure 2.12. shows the behavior of $(\Delta\theta)_{coh}$ with the scattering geometry for a fixed scattering volume.

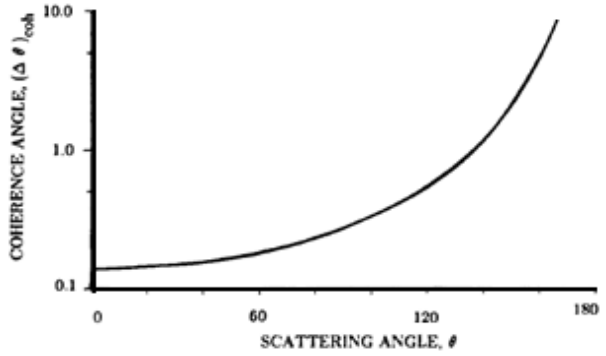

Figure 2.12: Fiber optics coherence angle vs scattering angle.[12] (used with permission)

From the plot, it is clear that the backscattering configuration offers a very favorable spatial coherence $(\Delta\theta)_{coh}$ of the entering light at higher scattering angles.[12]

Chapter 3: Experimental Materials & Methods

Section 3.1. Materials

Section 3.1.1. Chemical Reagents

The chemicals used in this research are listed in the following table 3.1. All of the chemicals were used as received.

Table 3.1: Chemical Reagents

Chemical	Purity	Supplier	Use
Carbon Lampblack	-	Fisher	Colloidal Particles
Sodium Dodecyl Sulfate	-	MP	Dispersion Stabilizer
Water	Deionized	In house by Milli-Q apparatus	Dispersant
Toluene	99.9>	Fisher Scientific	Dispersant/Cleaning
Acetone	99.7%	Fisher Scientific	Cleaning
1-Methylnaphthalene	97%	Acros Organics	Dispersant/Reactor Feed
Iron Naphthenate	6%	OM Group	Reactor Feed
Carbon Disulfide	99.9%	Sigma-Aldrich Co.	Reactor Feed
Nitrogen	99.998%	PRAXAIR Canada Inc.	Reactor Feed
Hydrogen	95%	PRAXAIR Canada Inc.	Reactor Feed

Section 3.1.2. Laser Backscattering Setup

One of the reactors using in this study was a batch system fitted with a window to allow on-line observations of the reactive chamber. The reactor as well as various auxiliary parts were placed inside an enclosure to minimize the personnel exposure to the laser light and to protect workers from sharp fragments of the window in the case of failure under elevated pressure. Figure 3.1. shows a representation of the enclosure with the insulated reactor and supporting platform. The remaining components of the experimental apparatus are set outside the enclosure; these components include the temperature controller, two laser sources of different wavelength, the spectrometer and the computer.

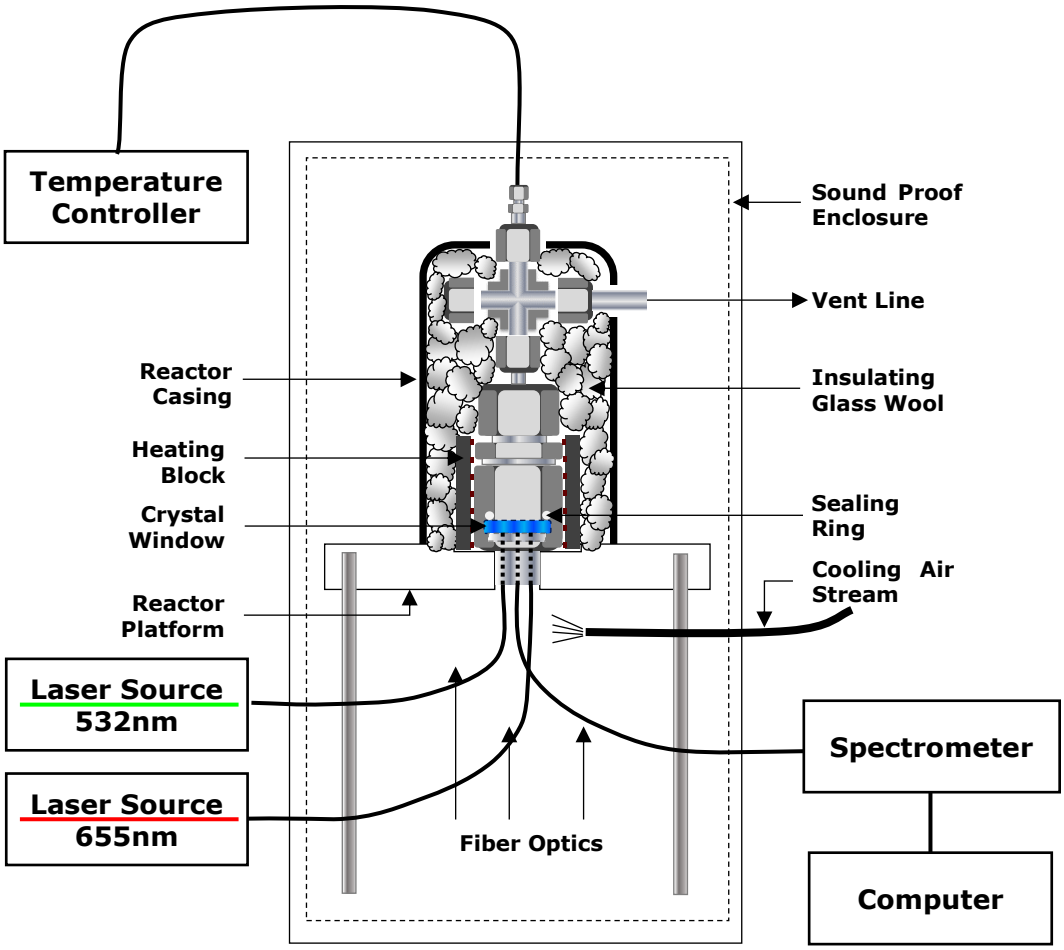

Figure 3.1: Schematic of laser backscattering system

The reactor was inserted in a custom made heating block, which was placed on top of a ceramic platform. The platform had a groove to accommodate the heating block minimizing the movement and a hole through in the center allowing access of the fibers optics to the bottom window. In this particular configuration, observations were made from the bottom of the reactor; this inverted configuration offers the advantage of observing the sample directly rather than through a gas phase as would be the case in a top-down configuration, thus avoiding condensation on the inside surface of the window. For high temperature measurements the heating block was surrounded by a layer of an insulating glass wool and braced by a steel casing to keep the assembly stable. A cooling air stream was also incorporated for the elevated operating conditions in order to maintain the integrity of the fibers during the duration of the experiment.

SECTION 3.1.2.1 REACTOR ASSEMBLY

The reactor vessel has a total available volume of 7.1 mL and is made of an assembly of stainless steel fittings. This reactor was developed and used in other applications[1, 21, 22] and the current configuration has proven capabilities to withstand elevated operating pressure and temperature up to 5 MPa and 420 °C respectively. Details of the individual reactor parts are described in Appendix A1.

For this project a gland and a holder were included so that the fiber optics could be used for particle size characterization. A detail explanation of the fiber optic holder design is presented in chapter 4. The rest of the critical components inherited from the previously developed reactor are described in the following sections.

SECTION 3.1.2.2. TEMPERATURE CONTROL

The reactor includes an OMEGACLAD® XL thermocouple probe, obtained from OMEGA Engineering. This thermocouple is aligned in the center of the reactor and submerged into the sample. The temperature control loop accomplished by an OMRON E5CK two mode controller automatically regulates a 300 W heating coil clamped around the heating block to reach and maintain the temperature set point.

SECTION 3.1.2.3. SEALING RING

The seal between the reactor body and the window is achieved by the deformation of an o-ring, which is placed in a small groove at the bottom reactor fitting. Two types of sealing rings were used depending on operating conditions, as shown in table 3.2.

Table 3.2: Sealing Ring Selection Criteria

Sealing Ring	Temperature [°C]	Pressure [MPa]
Fluorocarbon FKM O-Ring	<50	<1
Stainless Steel O-Ring	>50	<5

The selection of the sealing ring for low temperature operation was based mainly on cost given that the metallic ring had to be disposed after single usage due to their permanent deformation. The torque needed in the compression of the metallic sealing ring had to be delicately adjusted in order to avoid leaks (under-tightening) or breakage of the window (over-tightening).

Section 3.1.2.4. Optical Window

The bottom part of the vessel is closed by a cylindrical window that acts as a viewport for the incident lasers and scattered light. The selection of an ordered crystal material in contrast with cheaper amorphous solids such as glass is motivated on the reduction of inner reflection in the grain boundaries of the window resulting in light intensity loses and detection of noise signal. The different crystal material as well as thickness used during experimentation, are listed in table 3.3.

Table 3.3: Crystal Windows

Material	Refractive index @20 °C		Thickness [mm]	Provider
	532 nm	655 nm		
Yttrium aluminum garnet (Yag)	1.838[23]	1.828[23]	4	OptoCity
Aluminum oxide (Sapphire)	1.772[24]	1.765[24]	4 8	Meller Optics

In the case of the Sapphire windows, the crystal was C-axis orientated (C-axis normal to circular faces) to maintain the orientation of the crystal with the laser light direction and minimize the birefringence effect. The window thickness was a determining factor for the pressure rating of the vessel and geometry of the light propagation; calculations with the modulus of rupture of the selected crystals ensured safe operation up to 5 MPa of pressure at high temperature (up to 420 °C). Details of the calculations are shown in appendix B.

Section 3.1.2.5. Laser Sources, Fiber Optics and Spectrometer

The laser sources used in this project were 100 mW maximum output 532 nm and 655 nm nominal wavelength M-series Diode-pumped solid-state (DPSS) lasers with their respective manual power driver regulator obtained from Dragon Laser.

Fused silica core fiber optics of 800 μm diameter and 0.22 NA, obtained from OZ Optics Ltd, were used in order to transmit the laser light from the sources into the reactor as well as collecting the scattering from the sample. The fibers were conventionally terminated with standard SMA and FC/PC terminals on one end to connect with the laser sources and spectrometer, while the other ends were modified so that they could be inserted to the holder *via* custom made 1.8 mm OD stainless steel ferrule terminations.

The scattered light from the sample was measured by an AvaSpec-2048-USB2 spectrometer, obtained from Avantes. The signal collected was processed using AvaSoft 8.2.1.0, software. See section 3.2.1.3. for details.

Section 3.1.3. 15 mL Batch Reactor Setup

The 15 mL batch reactor system used consist in a 3/4" stainless-steel assembly provided by Swagelok. This reactor configuration offers a total of 15 mL of volume and can be safely operated up to 15 MPa of pressure at the reaction temperature of 380 °C. Agitation of the reactor was achieved by an electrical motor moving the reactor assembly in vertical direction keeping it inside a Tecam Fluidized Sand Bath (Model No. SBS–4). The temperature is controlled by an on/off OMRON E5CK controller and the sand bed fluidization was achieved through a regulated air flow at the bottom. In the rest of this thesis, this reactor system will simply be referred to as the batch reactor system. Details of this reactor individual parts are described in Appendix A2.

Section 3.2. Experimental Methods

Section 3.2.1. Laser Back Scattering Setup

Section 3.2.1.1. Cleaning Procedure

The cleanness of the device was a crucial preparation step, given that the reactor assembly was used multiple times. This cleaning step is critical to prevent cross contamination between measurements. For a thorough cleaning, the reactor system must be disassembled, rinsed, dried, reassembled and then pressure tested. In most cases particles got trapped in the fitting junctions and they were impossible to remove without disconnecting the fittings. The rinsing step was accomplished using either acetone or toluene for aqueous or organic dispersions, respectively; and the drying step was completed rapidly using compressed air. After the thorough cleaning procedure a leak test with nitrogen at 1 MPa was performed with an empty reactor to ensure the assembly was leak-tight. For replicates at room temperature using the same particles, the reactor disassembly step can be omitted.

Section 3.2.1.2. Sample Loading

Prior to the actual loading of the sample, proper selection of the sealing ring and window was required following the criteria showed is sections 3.1.3.3. and 3.1.3.4.

Since the sample was liquid in all cases studied in this project, the loading was made by disconnecting the assembly in the union cross having the window previously sealed in the reactor fitting. Amounts between 0.8 and 1.2 g were loaded in the vessel to ensure that the thermocouple tip was completely submerged in the sample for good temperature control.

After loading was complete and the reactor reassembled, nitrogen at 1 MPa of pressure was used to purge the oxygen from inside the reactor with 5 cycles of compression/decompression, followed by a leak test. For high temperature experiments, an additional leak test with nitrogen at 5 MPa was made due to the higher pressure inside the vessel caused by elevating the temperature. The final preparation step of the reactor consist in a pressurization to the initial condition identical for all the experiments of 1.2 MPa.

SECTION 3.2.1.3. *IN-SITU* MEASUREMENT PROCEDURES

Once the reactor is loaded, leak tested and pressurized, it was placed on the ceramic platform inside the enclosure described in Section 3.1.2. If experimentation was to be done at elevated temperatures, the insulating glass wool and the steel casing were affixed prior to the fiber optics. Special care was taken at the moment of placing the fibers in their respective holder channels; keeping the collection fiber connected to the spectrometer always in the central position and the illumination fibers connected to the laser sources in any of the available peripheral positions. As recommended by the supplier fibers handling manual, curvatures smaller than 6cm of radius had to be avoided. For high temperature experiments, before the start of the heat ramp and while the reactor is cool, the cooling air stream was triggered and spectrometer signal was monitored to identify if the compressed air stream may cause a shift in the position of the fibers. If a problem is identified, the fibers were repositioned before the start of the experiment.

The spectrometer software used had two specific configuration defined by the acquisition time of the signal: one used to observe the behavior of the backscattering intensity of the sample during the experiments was set to record the complete detection wavelength range (179.15 - 1100.34 nm) from the backscattered signal in 15 s intervals. The alternative software configuration used for the *in-situ* particle characterization was set to record 8000 spectra with an acquisition time of 1.05 ms over the range of 529.65-664.04 nm wavelength. These configurations were used for the study of the following two systems

SECTION 3.2.1.3.1. CARBON LAMPBLACK DISPERSION

Dispersions of 1% w/w of carbon lampblack (CB) with 1% w/w of sodium dodecyl sulfate (SDS) as stabilizer prepared both in in deionized water and 1-methylnaphtalene were studied in the online observation setup. The observations of the aqueous dispersion were done at room temperature while the organic dispersion was studied at both room temperature, 380 and 280 °C. Nitrogen was always used to achieve the initial pressure conditions. Both dispersions were characterized *ex-situ* as explained in the section 3.2.3.1.

SECTION 3.2.1.3.2. IRON BASED PARTICLE GENERATION

Reactions involving the *in-situ* generation of particles were carried at 380 and 280 °C for 20 min of reaction time, using an iron naphthenate and carbon disulfide stock solution as reactant mix, maintaining 3:1 atomic Sulfur to Iron ratio. These reactions were conducted exclusively with the 8 mm thickness sapphire window configuration and using hydrogen as atmosphere gas. Reaction products were collected and characterized *ex-situ* as explained in section 3.2.3.1. to validate the observations.

SECTION 3.2.2. BATCH REACTOR

The cleaning procedure of this reactor assembly consisted of consecutive rinse steps with toluene until the solvent was observed clear followed by a drying step using compressed air. A clean, dry reactor is loaded with a total of 4 g of feed material by disconnecting the top fitting connector. Once loaded, the oxygen in the reactor was purged with 5 consecutive compression/decompression steps with nitrogen at 1 MPa followed by leak test at 5 and 10 MPa. In this case the final pressurization stage was achieved using nitrogen and hydrogen respectively for 2 different set of experiments, maintaining 1.2 MPa of initial pressure at room temperature indifferently of the gas. When Hydrogen was used as atmosphere gas, additional purge of the nitrogen and following leak test with Hydrogen was performed prior the final pressurization step.

Sulfidation reactions were carried out in the batch reactor operated at 380 °C for 20 min of reaction time maintaining the same 3:1 S:Fe ratio in the feed. In this case the agitation was controlled at 355 RPM and the cooling of the reactor was achieved by removing the reactor from the sand bath and let it cool naturally to room temperature. The products of these reactions were collected and characterized with a transmission electron microscope (TEM) as explained in section 3.2.3.2.

SECTION 3.2.3. *EX-SITU* MEASUREMENT PROCEDURES

SECTION 3.2.3.1. LASER DIFFRACTION

The mean particle size of the samples were characterized *ex-situ* by a Malvern Mastersizer 3000 arranged with The Hydro MV sample cell, obtained from Malvern Instruments Ltd. Amount between 1.0 and 1.5 mL for the CB dispersions and between 0.2 and 0.3 mL for the case of the Iron particles were injected in the equipment cell to reach 5±1% of obscuration value recommended by the standard operating procedure of the Mastersizer for every characterization. The dispersant used in the sample cell was deionized water for the aqueous samples and toluene for the organic samples.

For every particle size analysis, the equipment software was configured to report the average particle size distribution curve of triplicate measurements. An additional authentication of the characterization was achieved by repeating the characterization before and after 1min of sample sonication in the cell.

SECTION 3.2.3.1. TRANSMISSION ELECTRON MICROSCOPY

The products of the iron particle reaction conducted in the batch reactor were mixed with toluene in equal amounts of the recovered sample to prepare the particles to the TEM analysis. The toluene-sample mix was agitated and centrifuged to extract half of the liquid phase of the mix over five cycles in order to minimize the content of the original solvent and the unreacted species in the sample.

Finished the preparation of the dispersion a copper matrix was immersed in the sample to offer a solid support to insert the adhered particles in the observation chamber of a CM20FEG transmission microscope operated at 200 kV and -1KPa of pressure.

Chapter 4: Fiber Optic Probe Design and Validation

Section 4.1. Fiber optic holder

The reactor assembly used in this work has been previously developed for inverted cross-polarized microscopy[1] and depolarization ratio[22], this configuration was adapted for the size characterization application with the addition of a stainless steel gland and custom made fiber optics holder below the reactor window as shown in Figure 4.1.

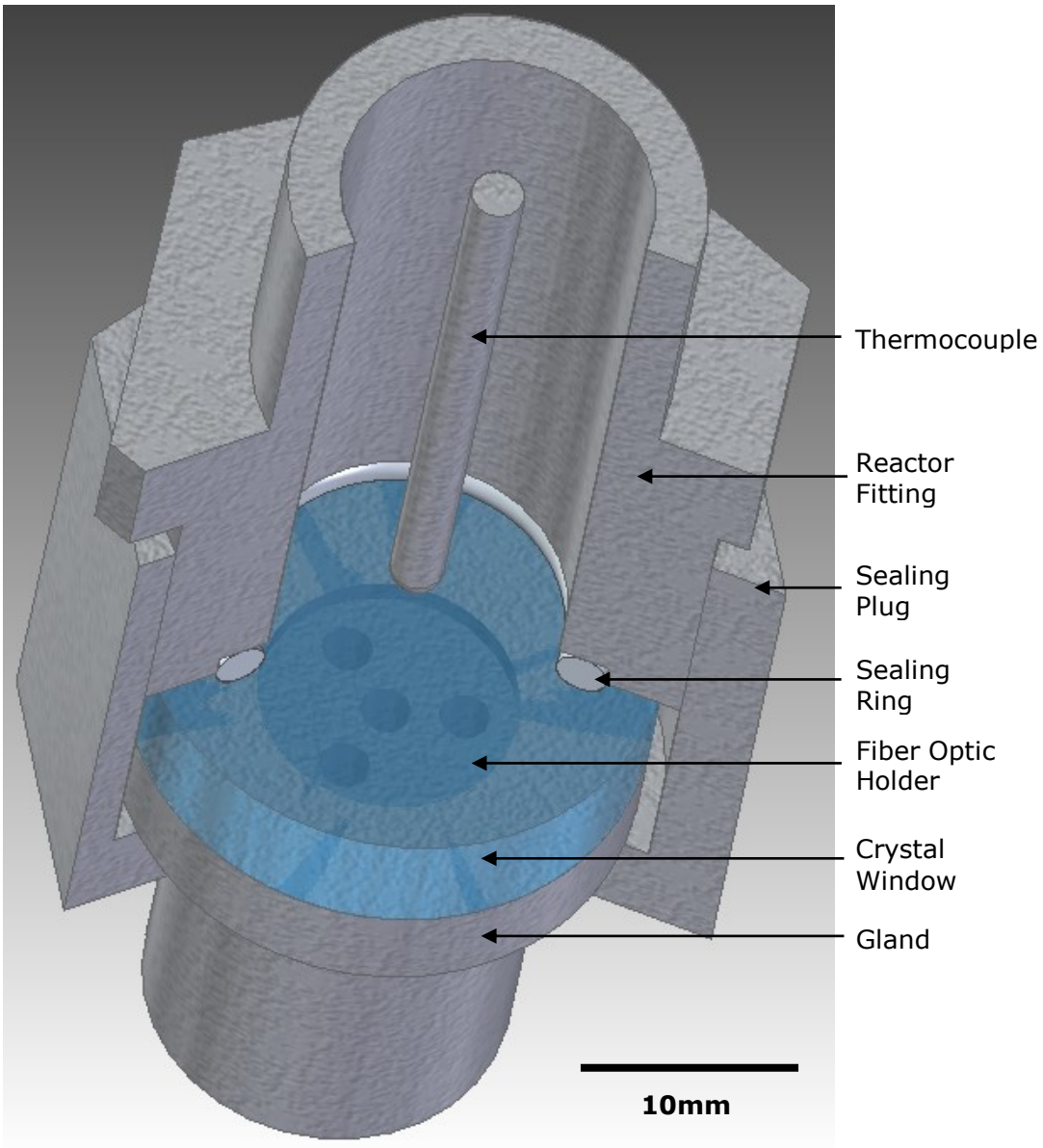

Figure 4.1: Reactor Assembly

The inclusion of the gland maintains the holder in a fixed position and orientated parallel with respect to the window, meanwhile the holder was design to fit tight inside the gland maintaining the fiber optics in the desired position below the sample chamber. For the system to work, the face of the fiber optic must be in good contact with the surface of the window, for that purpose both the holder and gland have matching treads to allow the front face of the fiber optics holder to be in direct contact with the outer surface of the window by screwing up the piece inside the gland. Figure 4.2. shows a close up illustration of the holder front and back face.

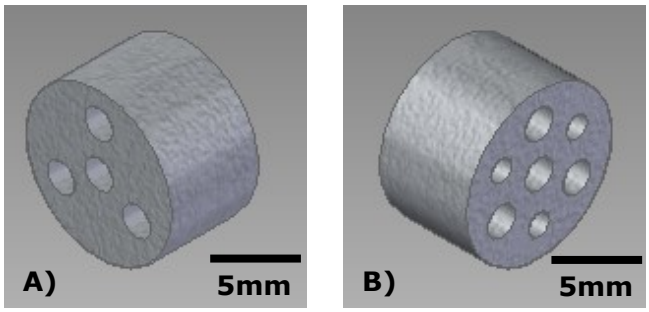

Figure 4.2: Fiber Optics Holder a) Front, b) Back

The four holes showed in Figure 4.2. A) were machined trough the piece to facilitate a tight fit of the fiber optics ferrule termination and are precisely positioned so that the central channel used for collecting the backscattered light is equidistant from each of the three available illumination channels. While the device was designed to allow for the simultaneous illumination from three lasers, only two channels were used in this study. Beside these fiber channels, Figure 4.2. B) shows three additional narrower holes that go halfway through the piece from the back face to facilitate the handling of the holder piece once inserted in the gland. The use of fiber optics for this project has help simplifying the setup from complex alignments; and reducing the use of vibrations sensitive components such as pinholes and optical lenses[25].

Since the penetration depth of the light delivered by an optical fiber is greatly limited by the absorption properties of the sample[5], multimode fibers were selected for this study. Compared against single mode fibers commonly used in similar applications[26], the bigger core diameter of multimode fibers enhance the device ability to operate with strongly absorbing samples by increasing the amount of light transported into the observation chamber[27].

Individual fiber channel for the transport and collection of the light offers the advantage of eliminating the need of a directional coupler for separating the illumination from

scattered light traveling through the same optical fiber avoiding background signals produced due to the collection of reflected light at the fiber termination[28] and therefore providing an extra degree of freedom from the configuration geometry over the overall resolution of the device[5].

SECTION 4.1.2. GEOMETRY OF THE HOLDER

Since optical lenses were not used for focus/collimation of the light beams in the device configuration studied in this project, the characteristic acceptance cone of the fibers optics was considered as the light propagation path through the window. Authors in various fields of study [5, 25, 28-33] have used similar arrangements of probes with multiple channels for different applications, showing special relationship between the setup geometry, namely scattering volume as well as the scattering angle, with the resolution of the measurement.

It is important to highlight that the presence of a crystal window in the configuration also impacts the measurement by affecting the relative alignment between the sample and the probe, and introducing beam steering effect on the incoming and scattered light that travels through the window[34]. The gland and fiber optic holder are specifically designed to maintain a parallel alignment of the probe with respect to the window during the measurement while the beam steering effect is studied in this work by comparing the signal changes using two crystal materials with different birefringence.

In the particular case of a backscattering configuration, the window presence also introduces two additional reflection surfaces that must be considered in order to maintain homodyne detection. The first surface encountered in the path of the transmitted light into the setup is the surface in contact with the gland and the holder while the second surface is the one in contact with the sample. Using separate fibers for illumination and detection has an extra advantage of requiring space between the fiber terminations thus preventing the collection of reflected light from the first crystal surface. Avoiding the reflection from the crystal-sample interface is achieved by increasing the spacing between the fibers to avoid overlapping of the individual light propagation cones at the second window surface.

Considering the limited light penetration depth in highly absorbent samples such as those used in this work maintaining a minimum allowable spacing between the fibers, considering the propagation cone, maximises the resolution of the device by increasing the effective scattering volume. As described earlier, the acceptance cones of the fibers

grow as the light propagates through the window before reaching the sample, therefore the crystal thickness becomes a determining factor on the geometry of the device. As a result the longest light propagation scenario studied in this project represents the critical design condition. Table 4.1 shows the calculations of the light propagation for every window configuration, see section 2.10. for details.

Table 4.1: Light Propagation Calculations

Crystal Material	Propagation Length [mm]	Acceptance Angle (θ_{max})	Minimum Spacing [mm]
Yag	4	6.87°	1.76
Sapphire	4	7.13°	1.80
	8	7.13°	2.80

The final design of the holder has 3 mm of spacing between the fiber cores to prevent the intersection of the acceptance cones at the crystal-sample interface, allowing for a slight margin of error in the manufacture. This spacing prevents the collection of reflected light from the inner surface of the crystal window even in the 8 mm thickness scenario. Figure 4.3. shows a representation of the acceptance cones propagation for the device with 8 mm thickness window.

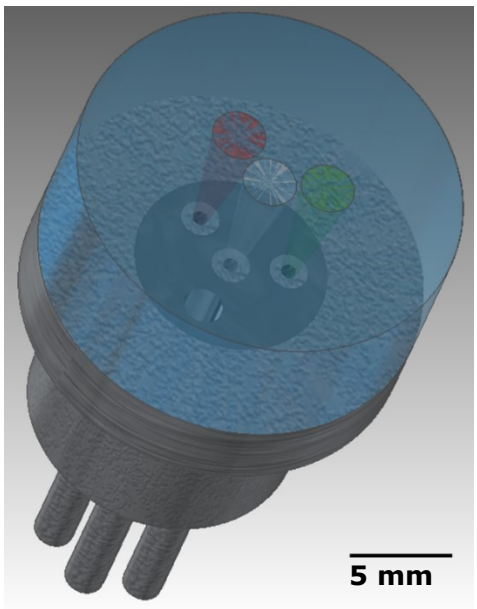

Figure 4.3: Backscattering Device Acceptance Cone propagation in 8 mm Window

The fiber termination faces were initially obtained by an electronic cleaver. With use, the ferrule faces suffered damage from wear. In order to maintain the smoothness and angle of the termination, the faces were maintained by polishing the ferrule ended

surface. The fiber termination faces were inspected after every experiment and restoration treatment with a 100x magnification microscope to detect imperfections.

SECTION 4.2. HEAT TRANSFER IN THE DEVICE

Given that an important part of this project is to study the capabilities of the device to make characterizations at high temperature, the fiber optics setup must be resilient to the elevated operating conditions. Furthermore the contact of the fibers with the reactor window demands additional measures to prevent damage to the heat sensitive components of the device, namely the plastic jacket of the fibers cannot withstand temperatures higher than 60 °C.

In light of this temperature limitation, a portion of the fiber at the ferrule termination was stripped and replaced by a stainless steel capillary. In addition, a cooling air stream was incorporated in the setup beneath the reactor around the stainless steel capillaries to maintain the temperature below the permissible limit. Given the fragility of the fused silica cores to bend, the cooling air flow rate had to be limited in order to avoid breakage of the fibers.

Simulations with COMSOL Multiphysics 5.0 were made considering a maximum temperature in the sample vessel of 420 °C to calculate the optimum pair of cooling air flow rate and capillaries dimensions. In the Figure 4.4. the temperature profile simulation of the final design is showed.

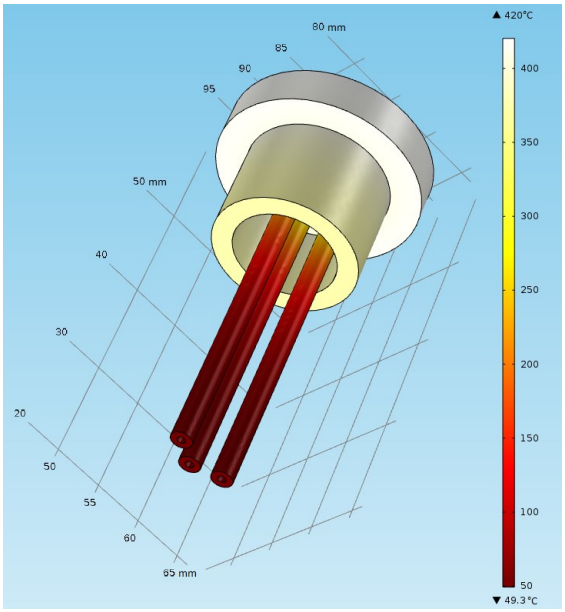

Figure 4.4: Temperature profile of the Device

Stainless Steel capillaries of 0.1 mm wall thickness and 25 mm length coupled with 0.5 m/s of cooling air at 25 °C were calculated to offer enough heat exchange surface to cool the fiber cores before reaching the plastic coating of the fibers. In practice the cooling air was regulated empirically maintaining the flow higher than the minimum rate calculated above without causing breakage of the fibers.

SECTION 4.3. DEVICE VALIDATION

Given the reflectivity of the inner walls of the reactor, validation of the spectra from the lasers as well as calibration of the spectrometer were achieved by observations of the empty vessel. Figure 4.5. shows the full wavelength spectra collected by the fiber optic probe from specularly reflected light from both laser sources.

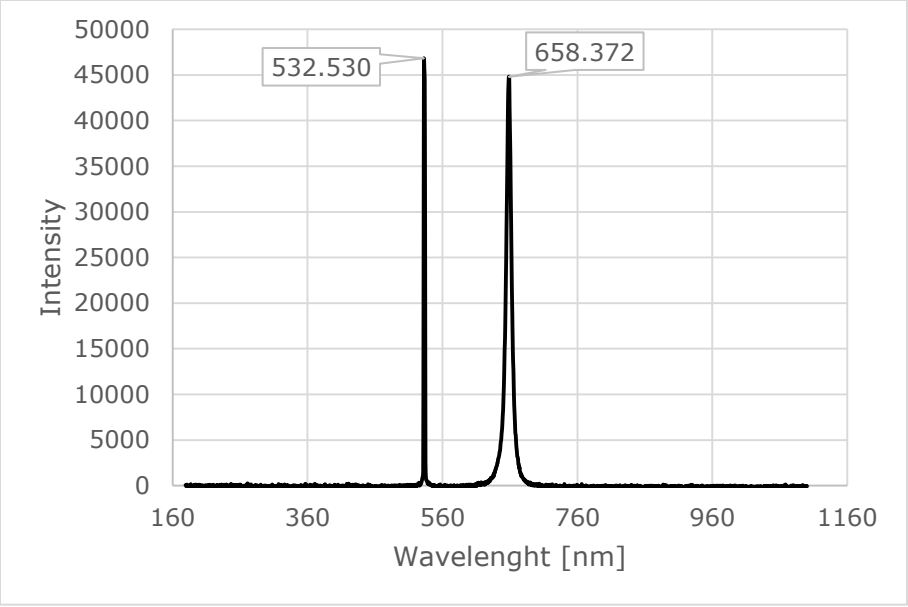

Figure 4.5: Raw laser sources backscattering spectrum

The plot indicates a consistent detection of the expected wavelength for both laser sources, even though the corresponding 655 nm signal bandwidth is considerably wider compared with the 532 nm as well slightly shifted towards higher wavelength with respect of the nominal wavelength. Later observations of the samples backscattering spectrum showed a consistent behaviour of the signal compared to the raw lasers light, reason why no additional measures were taken to correct the irregularities of the red laser source. It is important to highlight that during experimentation, output fluctuation of both lasers was observed during a period of 20 min after turning on the light sources. This fluctuation period correspond to a "warm-up" stage of the digital components of the

laser sources and respective drivers, reason why 40 min of pre-heating were promoted prior every measurements.

To confirm that the design geometry is effectively avoiding the collection of specular reflection from the crystal window surfaces, the spectrum of a black electrical tape placed over the 8 mm thickness windows was recorded. No detectable signal was obtained by the spectrometer, indicating that specular refection from any of the window surfaces was detected. Similar results were obtained for both 4mm thickness crystal windows, regardless the material.

SECTION 4.4. HIGH TEMPERATURE VALIDATION

In order to confirm the designed resilience of the device to high temperature as well as the effect that the increased operating conditions brings to the measurements, four thermal treatment replicates of Carbon lampblack dispersed in 1-methylnaphthalene were performed in the laser backscattering setup with a temperature ramp from ambient to 380 °C. Figures 4.6. and 4.7. shows the backscattering and temperature profile of such experiments at 532 and 655 nm wavelength respectively.

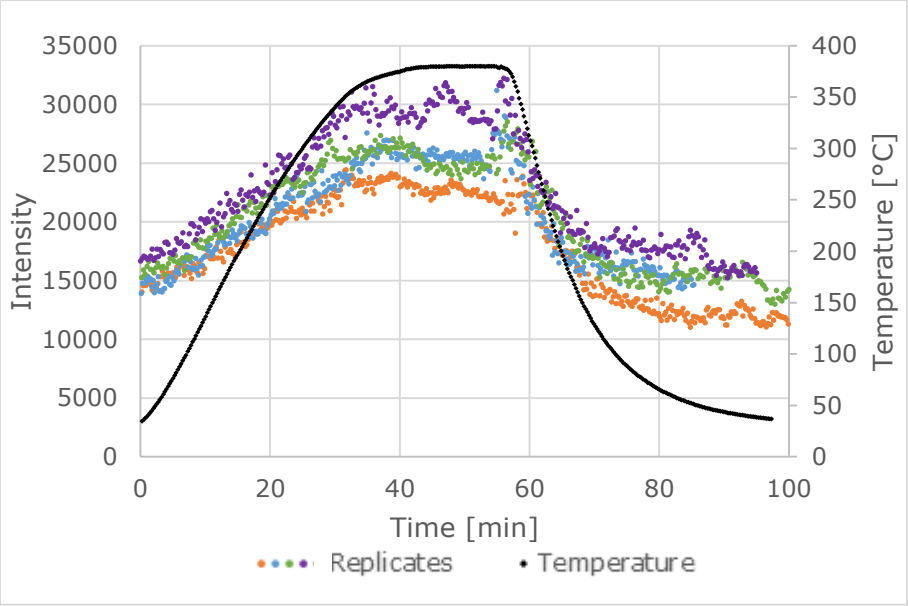

Figure 4.6: Carbon black thermal treatment backscattering signal at 532 nm

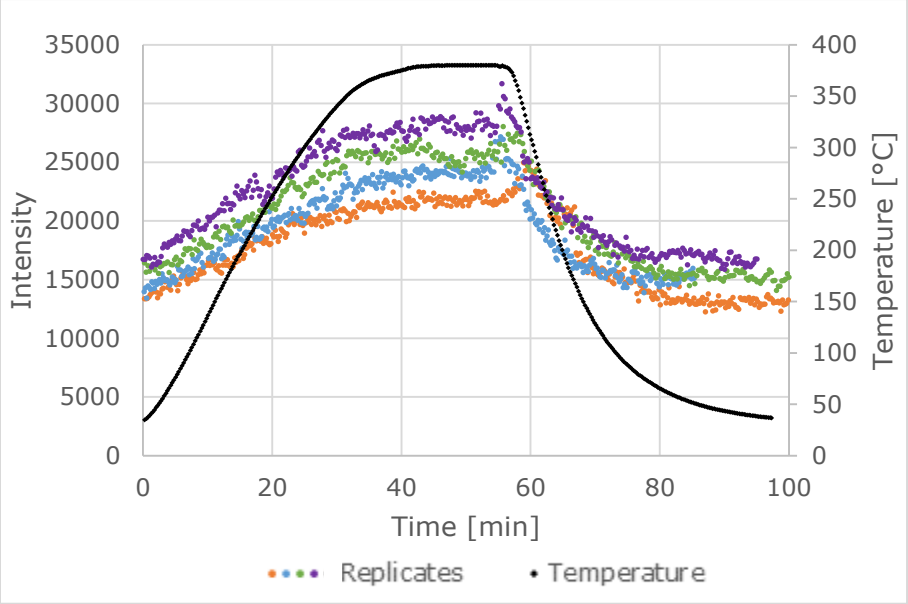

Figure 4.7: Carbon black thermal treatment backscattering signal at 655 nm

The graph shows the expected trend of the backscattering signal, considering that the change in the temperature causes changes in the refractive index of the sample. As the temperature increases, the refractive index of the sample decreases allowing more light propagation through the liquid which translates into more backscattering light traveling to the detection fiber, returning to the initial values as the temperature decreases to the initial conditions. In the graph is also observed a slight difference in the scale of each individual trend, which considering that the lasers power output was controlled by their respective driver to be the same for each replicate this variability is attributable to small differences in the physical configuration of the setup.

This reversibility in the measurement confirms the temperature resilience of the configuration allowing to perform high temperature observations of importance to this work without introducing apparatus caused by the elevated temperature.

Section 4.5. Size Characterization Technique Development

Given the early stage of this approach for the online particle size characterization at high operating conditions, basic understanding was needed to accurately configure and interpret the result. For that purpose a stable particle dispersion of carbon lampblack (CB) in both aqueous and organic medium was *in-situ* characterized as a validation stage prior to the application of this technique to a more realistic and dynamic systems such as a chemical reaction.

Section 4.5.1. Sampling Rate and Duration

Observations of aqueous carbon lampblack dispersion were made to analyze the limits of the current configuration. To optimize the utilization of the physical memory of the spectrometer, the wavelength spectrum of the signal was narrowed from full scale, 179.15 to 1100.34 nm, to the expected signal response from 529.65 to 664.04 nm. This change increases the maximum sampling capacity of the system to 8000 spectra that can be saved each minute at the maximum sampling rate of 1.05 ms. Figure 4.8. shows an example of a raw signal recorded with this configuration.

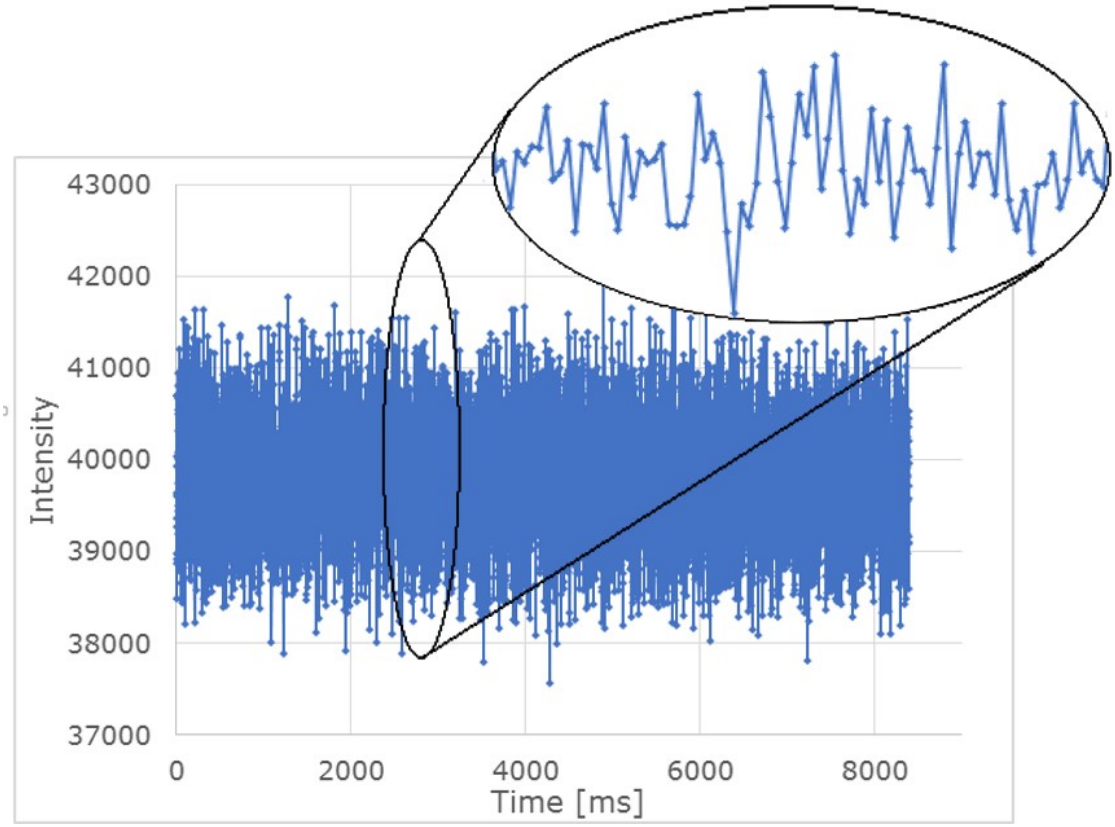

Figure 4.8: raw Backscattering signal

The intensity fluctuations recorded over the experiments are correlated with themselves (autocorrelation) increasing periodically the time lag of the correlation (correlation time) with the signal over the duration of the detection, allowing to extract information from the "random" trend of the signal in relation to the Brownian motion of the particles. Detailed explanation of the autocorrelation function and its statistical derivation of can be found in section 2.2.2, the final normalized form is shown below.

$$IACF = g^2(\tau) = \frac{\langle I_{(t)} \cdot I_{(t+\tau)} \rangle}{\langle {I_{(t)}}^2 \rangle} \qquad \text{Eq. 4.1}$$

The analysis of the signal is performed post-experimentation by a computational algorithm to finally calculate the corresponding intensity autocorrelation function (IACF) for multiple measurements simultaneously. The specific code used for read the raw data and calculate the IACF is included in appendix C1. Figures 4.9. and 4.10. shows a graph of the intensity autocorrelation function $(g^2(\tau))$ vs square root of the correlation time $(\tau^{0.5})$ representative from the set of 10 experimental observations made to the Aqueous CB with both sapphire windows mounted on the device.

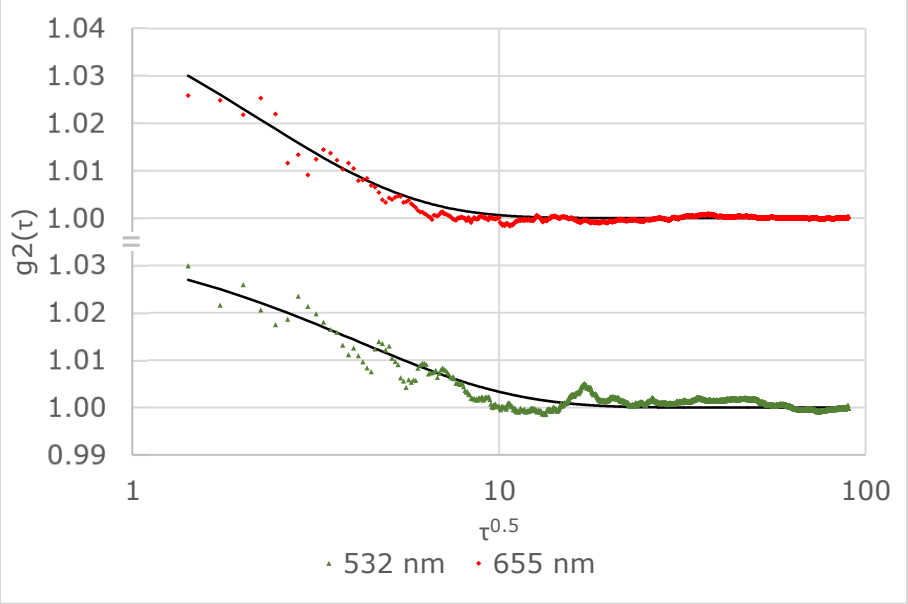

Figure 4.9: Aqueous CB IACF with 8 mm Sapphire window

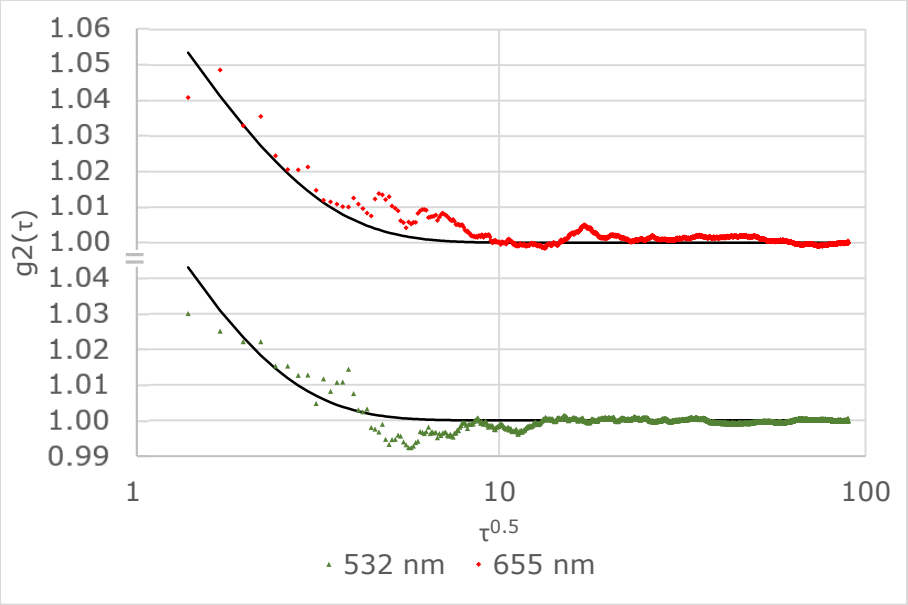

Figure 4.10: Aqueous CB IACF with 4 mm Sapphire window

Figure 4.11. show similar plot of IACF obtained by observations of the ACB with the YAG window configuration.

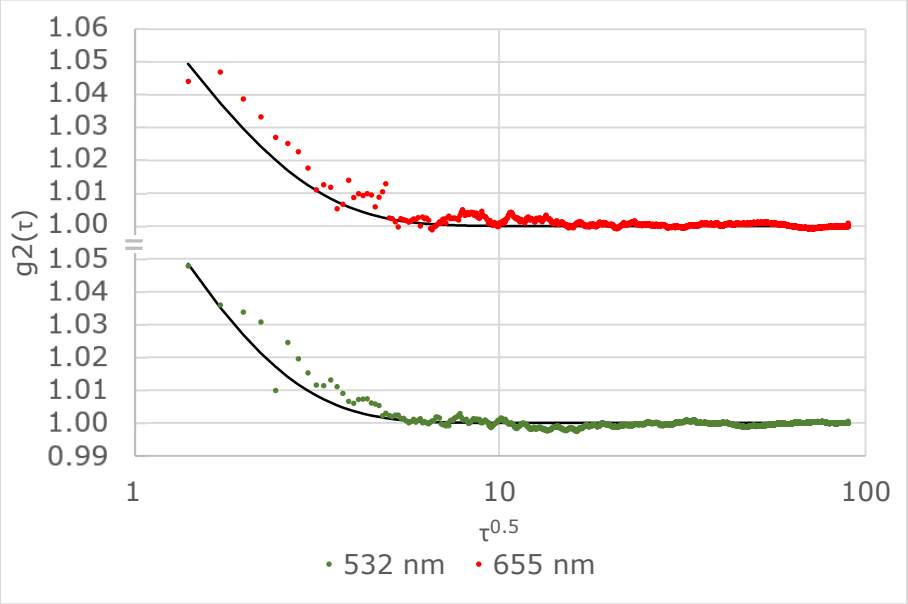

Figure 4.11: Aqueous CB IACF with 4 mm YAG window

The graphs show that the autocorrelation decay of the signal, regardless the device configuration, happens slightly faster than the detector sampling rate; evidenced by the start of the decay in the experimental data at the start of the trend. In light of this result the current configuration presents an under-sampling of the intensity fluctuations, also evidenced with the low initial value, at τ=0, of the experimental data compared with the value of 2 expected from the ideal autocorrelation function.

While the limitations observed and explained above would lead to poor results in terms of accuracy and precision from the current configuration of the device, the presence of a small portion of data before the full decay to the baseline of the IACF allows the online estimation of the particle size proposed for this work. The effect however of the capability of only detecting the final section of the IACF implicates high uncertainty and error in the results obtained from this device compared with the typical values of commercially available equipment using similar techniques.

In order to reduce the uncertainty of the results given the available detecting hardware and considering the small portion of useful data obtained by the current configuration of the device, two wavelength lasers were simultaneously used in order to double the

amount of information detected each time, thus reducing the relative error by increasing the amount of data without the need of replacing the available equipment.

Given that the calculations involved are based in the analysis of very fast signal fluctuations, ten times faster than the decay rate is a conventionally accepted sampling rate[10], however knowing in advance the value of the decay rate pose a very challenging estimation due to the complexity of the systems used in this project. Considering this aspect of the analysis and the limitations of the installed detecting equipment, the measures to maximize the use of the hardware memory available is furthermore required to enhance the particle size range capable of being characterize. It is important to clarify that in order to study smaller particles, the integration of equipment with faster signal acquisition time is required implicating no significant change in the treatment and interpretation of the signal developed in this work.

In terms of sampling duration, all the graph shows that the normalized intensity autocorrelation function quickly decays to the unity roughly after $\tau^{1/2}$=10 corresponding to 100 data point, showing that the sampling conditions provide enough detection time to observe the complete decorrelation of the temporal intensity fluctuations. However acquiring the signal for several orders of magnitude (decades) longer than the representative decay time is an accuracy determining factor given that enough pairs of data separated by the correlation decay time are needed for the autocorrelation function calculation[10]. For this reason the sampling configuration of this particular system was set to allow the spectrometer to acquire the maximum 8000 spectrum from which 4 set of 2000 continuous data points were analyzed separately from each detected spectra.

Section 4.5.2. Crystal Window Configuration

The behaviour of the light through their path along the window is a crucial factor of the measurement interpretation. Yttrium aluminum garnet (Yag) is a widely used material in the optical field due to its isotropic optical properties, however Aluminum oxide (Sapphire) in comparison present a more attractive, industrially wise, option considering its thermal and mechanical properties. Therefore the study of the effect of the anisotropic optical properties of the sapphire as window material is an important part of the scope of this project, maintaining at minimum possible this effect by selecting a C-Axis oriented sapphire crystal.

The intensity recorded with the 3 window configurations: 4mm Yag, 4mm Sapphire and 8mm Sapphire; was used to calculate the autocorrelation function fit to a three parameter negative exponential model of the form:

$$g2_{(\tau)} = a * e^{-b*\sqrt{\tau}} + c \qquad \text{Eq. 4.2}$$

In the following table 4.2. the exponential fitting coefficient "a" and "b" calculated for each versions of the device configurations are showed. The inclusion of the parameter "c" is to account for temporal fluctuation preventing the complete decay of the autocorrelation function to 1 which in all cases was resulted in 1±0.001.

Table 4.2: Autocorrelation Exponential Fit Coefficient

Material	Thickness [mm]	532nm			655nm		
		a	b	%Dev	a	b	%Dev
Yag	**4**	0.200	1.003	26.6	0.125	0.866	26.1
Sapphire	**4**	0.188	1.041	19.7	0.170	0.818	24.9
	8	0.038	0.244	12.8	0.057	0.452	12.4

The table shows a similarity within the coefficient of the exponential fit for the 4mm window thickness independently of the material. This results proof that the selected C-axis orientation of the sapphire effectively minimize the birefringence effect on the selected laser beams thus reducing errors due to changes in the light propagation path through the crystal window. It is important to highlight that the deviation of individual intensity measurement, %Dev, is associated to the low resolution of the configuration, expected from the previous results, and experimental differences in the adjustment of the fibers for each measurement beside differences in the optical window.

In the case of the 8mm window thickness a significantly different fit coefficients and lower variability in the measurements is obtained compared with the thinner window configuration. These results are strongly related to the device geometry which in this case provides a longer light propagation path enlarging the scattering volume, therefore minimizing the effect of differences in the device preparation increasing the configuration tolerance and enhancing the precision of the measurements.

The high concentration of particles greatly limits the light propagation inside the particle medium, shortening the penetration depth of the light causing a rapid fade of the light once it reaches sample. This effect causes the overall detected signal be less contributed by highly multiple scattered signal rather than less multiple or even single scattering events. The windows thickness plays a significant role in how multiple scattered

dependent is the overall detected signal. As the thickness of the window increases the acceptance cone for both the transporting and collecting fibers grows, thus increasing the effective illuminated volume of sample and the volume that can be detected by the central fiber as well as reducing the relative distance between the illumination and the collection propagation cone. Figures 4.12. and 4.13. shows a comparison of the scattered intensity recorded with 4 and 8 mm thick sapphire window maintaining the same power output for both 532 and 655 nm wavelength lasers.

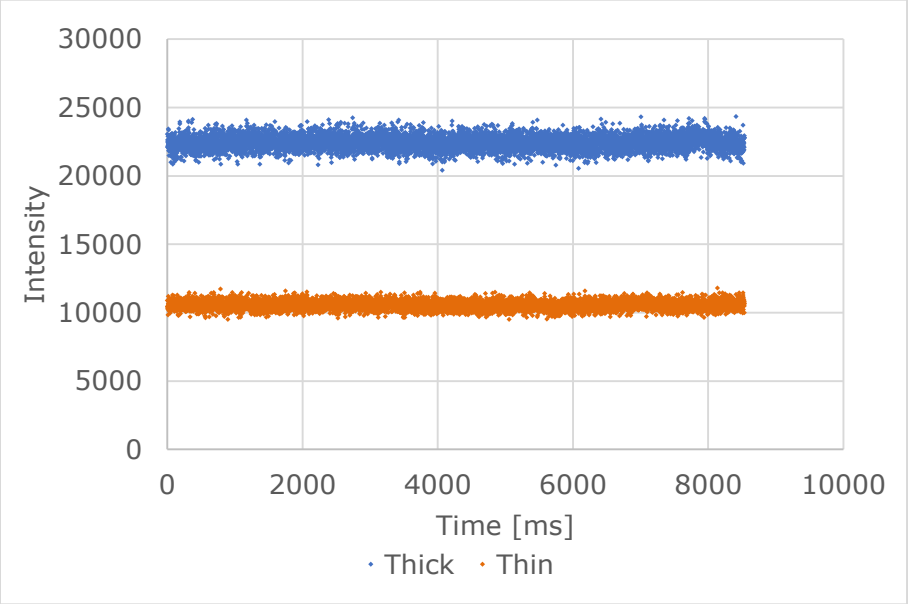

Figure 4.12: window Thickness effect Backscattering Intensity at 532 nm

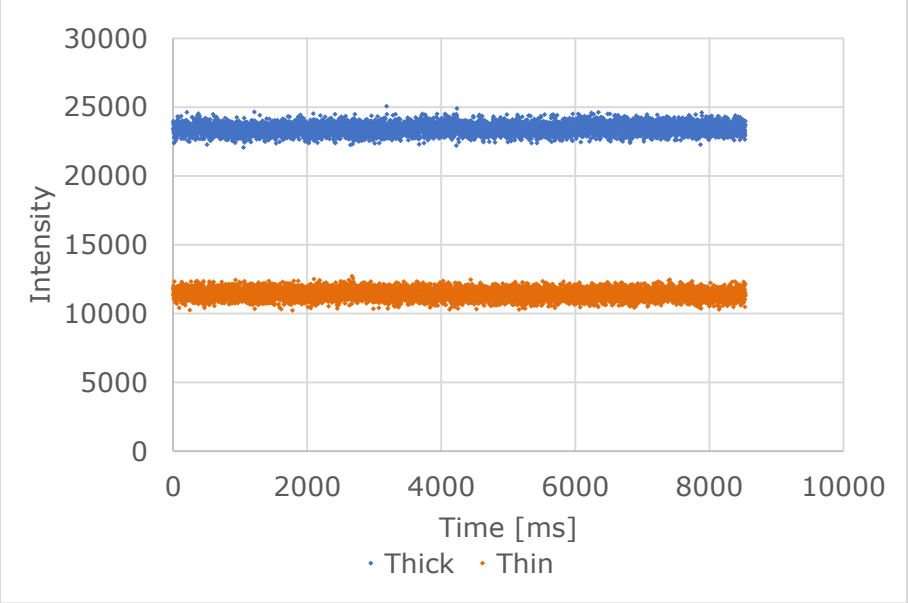

Figure 4.13: window Thickness effect Backscattering Intensity at 655 nm

The expected behaviour based on the effects previously explained is demonstrated in the graphs were the average scattered signal intensity for the 8 mm thick window is roughly 2.5 times higher in magnitude than the signal detected under the same laser power output with the 4 mm thick window. The weaker signal intensity under the thinner version brings a lower signal to noise ratio and therefore less precision comparing to the thicker version.

Considering the beneficial effect in terms of resolution and precision given by the windows thickness and the enhanced mechanical and thermal properties of the sapphire compared with Yag, with no apparent loss of optical properties; the 8 mm thickness sapphire window was selected to be used exclusively for the rest of the studies in this research.

SECTION 4.5.3. GEOMETRIC FACTOR DETERMINATION

Having selected the best available configuration for the device, dispersion of carbon lampblack in 1-methylnaphthalene were observed and analyze at room temperature to calculate the geometric factor necessary for the particles size estimation.

Considering the derived equation for DWS under backscattering configuration explained in the chapter 2, the following simplification can be made

$$g^1{}_{(t)} \approx e^{-\gamma\sqrt{6\tau/\tau_0}} \qquad \text{Eq. 2.15} \qquad \tau_0 = {}^1/_{D_0 q^2} \qquad \text{Eq. 2.19}$$

$$D_0 = \frac{2*K_B*T}{6*\pi*\eta_{(T)}*d} \qquad \text{Eq. 2.20} \qquad q = \frac{4*\pi*RI_{(T)}\sin(\theta/2)}{\lambda_0} \qquad \text{Eq. 2.2}$$

Substituting τ_0, D and q on $g1_{(\tau)}$ is obtained

$$\ln(g1_{(\tau)}) = -\gamma * \frac{4 * \pi * RI_{(T)}\sin(\theta/2)}{\lambda_0} * \left(6 * \frac{2 * K_B * T}{6 * \pi * \eta_{(T)} * d} * \tau\right)^{1/2}$$

Given that in Backscattering configuration θ=180°, then

$$\ln(g1_{(\tau)}) = -\gamma * \frac{4 * (2 * \pi * K_B)^{1/2}}{\lambda_0} * RI_{(T)} * \left(\frac{T}{\eta_{(T)} * d} * \tau\right)^{1/2}$$

$$\boxed{\ln(g1_{(\tau)}) = -\boldsymbol{C_{\lambda_0}} * RI_{(T)} * \left(\frac{T}{\eta_{(T)}*d} * \tau\right)^{1/2}} \qquad \text{Eq. 4.3}$$

Where the factor "C_{λ_0}" represent a calibration factor for each wavelength that comprises all the temperature independent constant and the empirical geometric factor for the configuration. Linear fitting of the $\ln(g^1(\tau))$ obtained from the intensity measurements vs $\tau^{1/2}$ can be calculated with a known particle size sample to determine the calibration factor of the system under observation at each specific signal wavelength. The Figure 4.14. shows a characteristic trend for the experimental data acquired under this configuration with the corresponding linear fit.

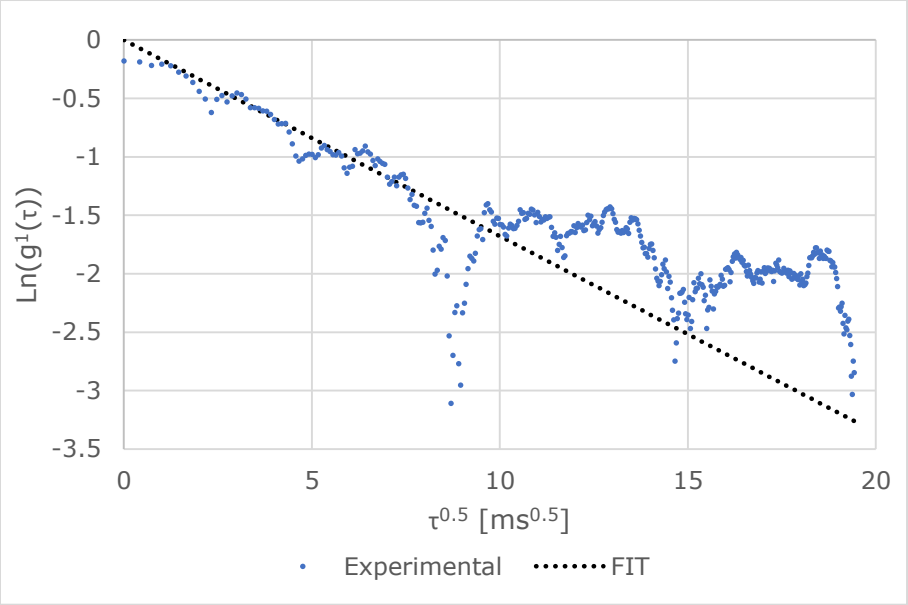

Figure 4.14: Calibration Factor Linear Fit

In the Figure is shown that roughly after $\tau^{1/2}$=5 (τ=25ms) the experimental data start to deviate significantly from the linear data, which lead us to consider only the initial portion of the data for the fitting. This deviation at longer decay times is characteristic of this kind of measurements under backscattering configuration, and is related to the broader distribution of autocorrelation decay time caused by the contribution of many multiple scattered signal at later detection times[18,16].

Given the considerable variability between individual measurements, triplicates of the *in-situ* observations were carried along with their respective *ex-situ* characterization of the sample before and after a heating the sample to 280 °C, to calculate the calibration factor for this system. Table 4.3 shows the values of the calibration factor at both wavelength. The calculation algorithm used to determine the autocorrelation function as well as the linear fit coefficient is shown in Appendix C2.

Table 4.3: Calibration Factor C_{λ_0} for Carbon Lampblack at room temperature

Replicate	Wavelength [nm]					
	532			655		
	Raw	Treated	%D	Raw	Treated	%D
1	1.26E-07	1.40E-07	10.8	1.79E-07	1.58E-07	12.2
2	1.52E-07	1.53E-07	0.5	1.80E-07	1.83E-07	1.7
3	1.63E-07	1.50E-07	8.2	1.96E-07	2.12E-07	7.7
Average	1.47E-07	1.48E-07	0.5	1.85E-07	1.84E-07	0.3
%Dev	13.0	4.4		5.3	14.6	

The table summarizes 2 relative deviation: first regarding the difference of the calculated value before and after each individual experiment; and a deviation from all the measurement to the average calibration factor calculated individually before and after the thermal treatment from each replicate. Once more, the effect of the low acquisition rate affects the accuracy of the measurements as shown in the magnitude of the %Dev in the table. The difference obtained comparing the values before and after the heating cycle are presumably more related to experimental factors promoted by the elevated temperature than actual changes in the dispersion.

In order to confirm the significance of the variability obtained from the heating process, a two tail t-test analysis of the average calibration factor obtain from the experiments for each wavelength was performed. The results of these tests t_{532nm}=0.93 and t_{655nm}=0.96 shows no statistical differences between the calibration factor value calculated for each wavelength before and after the heat treatment, reason why a single average calibration factor from all the measurements is determined for each wavelength $C_{532}=1.47_x10^{-7}$ and $C_{655}=1.85_x10^{-7}$.

Maintaining the position of the fibers was an important designing factor, however the repetitive use requires manual removal/insertion from one measurement to the next introducing slight alignment differences due to human factors within each experimental observation. In light of these results it is presumed that the effect of this process was largely underestimated causing extensive implications over the reproducibility of the results. Even with these limitations, the autocorrelation function obtained from the intensity fluctuation measurements shows the expected exponential decay trend given the diffuse light propagation approximation similar to the reported behavior of concentrated systems in the literature[25, 35-37]. Therefore the calculated calibration factor allow this technique to be use as a semi quantitative sizing technique despite the source of error already discussed.

Having calculated the calibration factor for this particular system, extracting particle size information from the sample is the next step in the development of this technique. At room temperature information regarding the refractive index of the dispersant is available from the literature[38], however the absence of the dispersant optical properties at high temperature pose an additional calculation problem reason why the two scenarios are treated separately in the following sections.

SECTION 4.5.4. SIZE CHARACTERIZATION AT ROOM TEMPERATURE

Using the already calculated calibration factor the particle size was calculated independently for each wavelength signal. Tables 4.4. and 4.5. summarizes the particle size results obtained through the calculations based on the *in-situ* measurement with the respective *ex-situ* characterization of the sample before and after each heating process for four replicates.

Table 4.4: Size characterization of raw Carbon Lampblack

Replicate	*Ex-situ* [nm]	*In-situ*			
		Wavelength [nm]			
		532		655	
		Size [nm]	%Error	Size [nm]	%Error
1	162	309.4	91.0	238.6	47.3
2	162	338.7	109.1	279.7	72.6
3	162	350.3	116.3	273.5	68.8
4	162	277.1	71.1	306.1	88.9
Average	162.0	318.9		274.5	
DEV	0.0	32.7		27.8	

Table 4.5: Size characterization of thermally treated Carbon Lampblack

Replicate	*Ex-situ* [nm]	*In-situ*			
		Wavelength [nm]			
		532		655	
		Size [nm]	%Error	Size [nm]	%Error
1	163	261.5	60.4	262.1	60.8
2	167	248.7	48.9	268.3	60.7
3	164	305.1	86.0	214.6	30.9
4	171	238.5	39.5	220.0	28.7
Average	166.3	263.4		241.3	
DEV	3.6	29.3		27.8	

In both cases the analysis of the measurements shows the expected magnitude of variability considering the result showed previously regarding the calibration factor

calculation. In addition a slight difference is obtained in the case of the *ex-situ* characterization after the heating cycle of the sample in each case, in order to confirm the significance of the particles apparent difference due to the thermal treatment a two-tailed t-test analysis of the *ex-situ* mean particle size was done obtaining a value of t=0.099. which compared with a p=0.05 proofs that there is no statistical difference between the mean particle size of each experiment due to the heating of the sample.

Similarly, t-test analysis of the particle size calculated by each wavelength measurement was performed obtaining t=0.084, confirming no statistical differences between the particle size calculated with each wavelength therefore supporting the use of two different wavelengths in this work to effectively double the information obtained from the measurements. With all this statistical considerations, the final particle size characterized by this technique is 274.5±39.3 nm with 67.26% of error relative to the particle size characterized by the *ex-situ* technique.

Further comparison of the value calculated for the particle size shows a significant deviation towards bigger particle sizes compared with the *ex-situ* characterization. This difference can be explained in relation to the operation principle of each characterization technique: the *ex-situ* method used is based in the deconvolution of the laser diffraction patterns caused by the sample, meanwhile the *in-situ* device has been developed to use the diffuse wave spectroscopy approximation of the dynamic light scattering technique which is based on measurements of the intensity fluctuations caused by the sample motion.

In a laser diffraction measurement the scattered light from the large particles in the sample size distribution is lost in the experimental noise creating a bias of the technique towards the pattern generated by the smaller particle from the size distribution[3]. Contrarily the backscattering intensity of a particle is proportional to the sixth power of its diameter (from Rayleigh's approximation)[12], therefore causing the *in-situ* characterization being extensively bias towards the intensity fluctuations caused by larger particles.

Section 4.5.5. Size Characterization at Elevated Temperature

Having studied the system at room temperature and after obtaining reasonable agreement between the particle size characterized with a recognized commercially available *ex-situ* technique and with the *in-situ* technique developed in this work, validation under elevated operating conditions represent the next validation step.

Given that the calculations of this technique are based on the fluctuations of the backscattering signal caused by particle displacement modeled by Brownian motion, deviations in the flow pattern of the particles greatly influence the measurements. This aspect of the technique requires special measures at high temperature condition to minimize deviations such as convection patterns inside the sample cause by temperature fluctuations. In order to minimize this effect, a temperature stabilization period with a maximum variations of 0.5 °C during a lapse of 20 minutes was controlled before the signal measurements.

As described before from the signal recorded, the analysis of 4 sets of 2000 data points from each recording minimizes the effect of anomalies in the measurements. Despite this measure the variability obtained is still considerably high, reason why a filtering criteria was included for the calculated values to reduce the variability of each experiment data set. This criteria is based on an exclusion of the measurement whenever the IACF linear slope value falls out of the standard deviation range of the whole set of measurements recorded. Table 4.6. summarizes the changes to the average and relative standard deviation of the set of measurements for each experiments due to the filtering criteria implemented.

Table 4.6: Measurement exclusion for Carbon Lampblack at High Temperature

Rep	***IACF* Slope Wavelength [nm]**							
	532				**655**			
	Raw Ave ($_x10^{-2}$)	**% DEV**	**Filtered Ave ($_x10^{-2}$)**	**% DEV**	**Raw Ave ($_x10^{-2}$)**	**% DEV**	**Filtered Ave ($_x10^{-2}$)**	**% DEV**
1	-9.9	62.8	-8.5	23.8	-14.5	52.4	-14.2	24.2
2	-11.5	44.3	-8.9	18.6	-18.7	66.7	-17.5	36.4
3	-19.0	75.5	-10.2	32.4	-12.1	45.1	-13.1	12.9
4	-10.7	67.8	-8.4	16.7	-13.5	37.6	-14.3	15.1
Ave		62.6		22.9		50.4		22.1

The table shows even greater error values related to the accuracy and reproducibility compared to the results in previous sections of this work influenced in this case by the temperature fluctuations explained before, confirming the importance of the temperature stabilization. From the table is also obtained a substantial difference in the error value within a single experiment measurements due to the filtering criteria, reducing from roughly 60% to 20%, showing the importance of the exclusion of anomalous measurements.

Considering the data acquisition limitation already discussed at room temperature, the high temperature further impact the resolution of the detection given the enhanced motion of the particles promoted by the elevated operating conditions. The significant reduction of the variability obtained through the implementation of the exclusion criteria, shows an additional profoundly underestimated implication of the temperature on the precision of the observation. Given that with the increase in temperature the geometry of the device is subject to change due to thermal expansion of the components, additional displacement on the fibers due to the cooling air stream incorporated below the setup is presumed to cause unrelated differences from one experiment to other. In light of this effect 30 measurements were taken at high temperature from each wavelength to have more available information after the initial filtering of the data.

At the elevated conditions, additional ways to estimate the solvent refractive index are required to be able to solve the DWS equations to extract particle size. The "one-third" rule[39-41] is a frequently used correlations in the oil and gas industry used to estimate hydrocarbon density from *in-situ* refractive index measurement by using the Lorenz-Lorenz model for the molar refractivity as follow

$$\frac{1}{3} \approx \frac{1}{\rho}\left(\frac{n^2-1}{n^2+2}\right) \qquad \text{Eq. 4.4}$$

Given that the correlation is commonly used in its field of application over a broad range of temperatures and pressures, the reverse use proposed on this project to estimate the refractive index knowing the density of the dispersant is therefore supported with confidence under the conditions studied in this work.

Density estimations of the solvent at elevated condition required for the one-third rule, poses a relatively easier task by relying on a cubic equations of state. Even though the direct form of an equation of state does not include density, there are extensive available studies in the literature for density of liquids that helped modify the classical equations of state over the years into very reliable equations such as the Peng-Robinson to estimate the properties of liquids. In this work the estimation of liquid density was obtained by using a commercial version of a Virtual Materials Group Simulator (VMGSim) configured with Peng-Robinson equation.

The validity of using the "one-third" rule and the estimation of the liquid properties in this work was checked at room temperature, obtaining a MeNa refractive index of RI=1.599, in good agreement with measured values found in the literature (1.612-1.618)[38]. Following this procedure, the solvent properties were calculated at elevated

temperature obtaining a range of refractive index of 1.465 to 1.475 within the range of temperature at which the replicates were conducted (272.3-286.0 °C).

The increased temperature also impacts the overall behavior of the dispersion regarding the particle-particle and particle-dispersant interactions, introducing additional deviations with respect to the behavior exhibit at room temperature. For this reason the calibration factor studied and calculated at room temperature only describes the system at the operating condition at which was calculated, therefore requiring the re-calculation of the calibration factor for the high temperature condition. With the dispersant refractive index estimation at elevated conditions and given that the t-test analysis over the *ex-situ* analysis showed no significant change in the particle size due to the heating cycle of the sample, the calibration factor can be determined as before (see section 5.1.1) for the elevated operating conditions. Table 4.7. summarizes the results of the 3 replicates conducted for the calculation of the high temperature calibration factor.

Table 4.7: High Temperature Calibration Factor C_{λ_0} for Carbon Lampblack

	Wavelength [nm]			
	532		**655**	
	Room T	**High T**	**Room T**	**High T**
Average	1.47E-07	1.92E-08	1.85E-07	2.95E-08
STDEV	8.7	20.6	9.8	18.2

As expected, the results showed for the high temperature calibration factor have a considerably higher experimental standard deviation and the average value is roughly an order of magnitude different from the calibration factors values obtained at room temperature. These two results confirms the large impact of the high temperature on the behavior of the dispersion and the impact of the temperature gradients in the sample creating convective flow inside the sample.

Using the new calibration factor, the particle size can be calculated with the *in-situ* measurements at high temperature with the same calculation algorithm showed in appendix C2, obtaining the following results summarized in the table 4.8.

The particle size calculated using the high temperature calibration factor maintain the same relative error within each other due to the inherent resolution of the setup discussed in the previous sections. Similarly as with the measurements at room temperature, t-test of the results from each wavelength signal allows to obtain an overall particle size of 215.8±23.3 nm with 31.49% of error relative to the particle size characterized by the *ex-situ* technique.

Table 4.8: *In-situ* carbon lampblack average particle size at high temperature

Replicate	*Ex-situ* [nm]	*In-situ*			
		532 nm		655 nm	
		Size [nm]	%Error	Size [nm]	%Error
1	163.0	249.1	52.84	228.2	39.98
2	167.0	209.9	25.69	189.5	13.46
3	164.0	190.1	15.90	236.3	44.06
4	171.0	230.4	34.75	193.1	12.92
Average	166.3	219.9	32.30	211.7	27.60
%Dev	3.6	25.5		23.9	

It's also important to highlight that the apparent improvement in the accuracy of the result obtained with the 31.49% error associated with the *in-situ* average particle size at high temperature compared with the analogous *in-situ* particle size characterized at room temperature of 67.26% is a temperature effect rather than an actual enhancement on the precision of the technique at elevated operating conditions. As expected, high temperature causes deviations of the apparent particle size result towards smaller particle size values given the boost in the particle motion which is associated to smaller particles undergoing faster motion[6, 7, 12, 42].

At this point enough confidence of the mechanics of the measurement and the interpretation of the results was achieved to continue with the *in-situ* particle size characterization of reactive systems, however it is expected to have even higher uncertainty and accuracy issues in a dynamic system such as a chemical reaction based on the poor consistency and reproducibility of the experiments discussed in this section.

Chapter 5: Characterization of *In-situ* Generated Iron Based Nanoparticles.

Section 5.1. Particle Detection

The formation of iron sulfide nanoparticles by the thermal decomposition of iron naphthenate was selected for this study due to its proven capabilities of *in-situ* particle generation[43,44]. Previous studies with this system were focused on the formation catalytic iron particles for heavy oil hydrogenation. A description of the dynamic process of the particle generation, however, has not been well described in the literature. In this work, the effect of the reaction temperature and atmosphere composition on the iron particle generation from iron naphthenate were investigated. Particle generation was carried out in both the batch reactor system and the laser backscattering setup and the reaction products were characterized *ex-situ*.

The batch reactor system was operated isothermally at 380 °C and an initial cold pressure of 1.2 MPa, following the procedure explained in the section 3.2.2. Micrographs of the reaction products from experiments using nitrogen and hydrogen are presented in Figures 5.1 and 5.2., respectively.

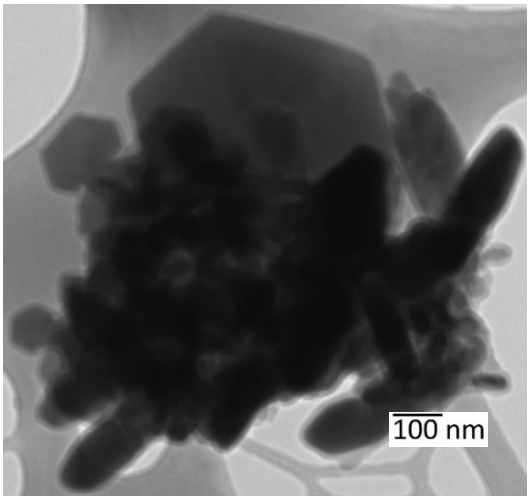

Figure 5.1: Iron Nanoparticles in Nitrogen Atmosphere

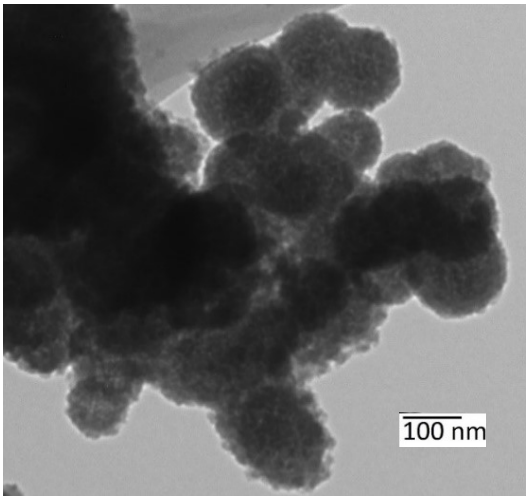

Figure 5.2: Iron Nanoparticles in Hydrogen Atmosphere

Using nitrogen, the particles present a rod-like shape, Figure 5.1., compared with the spherical shaped particles obtained in the case of hydrogen, Figure 5.2. Even though the shape of the particles clearly differ depending on the gas used, the apparent average sizes of the particles in each case are roughly from 100 to 200 nm. In the reference literature available for this system[43,44], however, the average particle size obtained under similar operating condition is in the range of 10 nm. The much smaller particle size obtained in other works found in the literature is highly influenced by particle-solvent interactions, given that in those studies particles were *in-situ* generated to serve as catalyst for hydrogenation in the presence of the complex heavy oil samples whether 1-Methylnaphthalene is the only specie present as solvent in this work. The complexity of a heavy oil feed may introduce a significant difference in the presence of nucleation sites for the iron particle growth in comparison to the pure MeNa, however the effect of the solvent complexity in the final particle size is not covered by this work.

Particle size characterization using DWS involves the measurement of intensity fluctuations which are mathematically analyze to extract particle size information from the sample. Several simplifications of these equations are valid only for spherical shaped particles, making the interpretation of the signal response much easier for this type of particle morphology. Consequently, hydrogen was selected as atmosphere gas in this work for the online study of the Iron-based particle synthesis due to their spherical shape.

The micrographs also shows that nearly all of the particles analyzed by TEM were agglomerated. This agglomeration is likely an artefact caused by the concentration and drying of the particles needed for the sample characterization in the TEM due to the low particle concentration obtained from the reactions.

Considering that the development of a device for the real-time characterization of particle size is the objective of this work, differences in the backscattering signal of a sample caused by the presence of particles is key study of this research by comparing the signal behaviour obtained during the reaction with the case of only 1-Methylnaphthalene. These experiments were carried out in the laser backscattering setup using a temperature ramp from ambient to 380 °C, following the method explained in section 3.2.1.3.2. Figures 5.3. and 5.4. shows the backscattering and temperature profile of such experiments at 532 and 655 nm wavelength respectively.

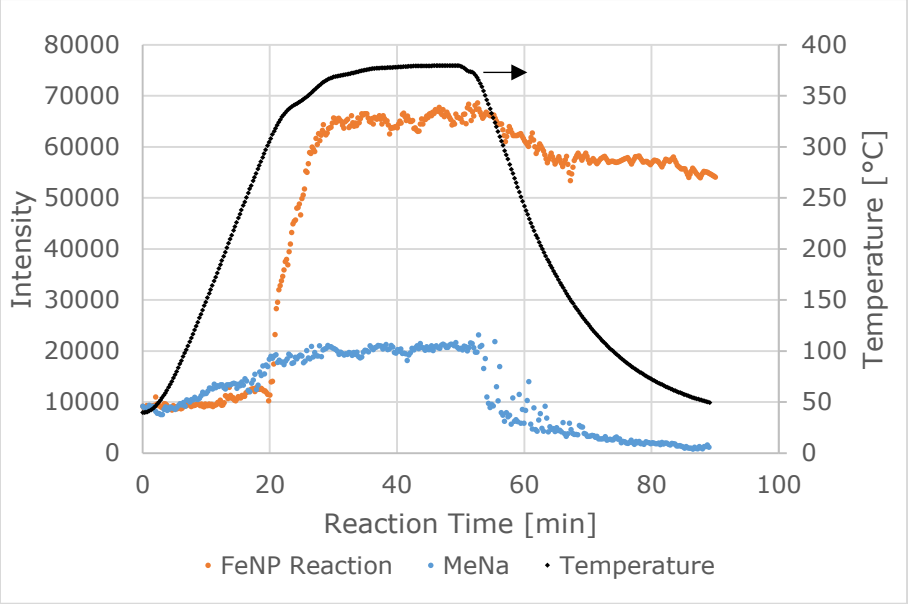

Figure 5.3: Backscattering signal of FeNP Reaction and MeNa at 532 nm

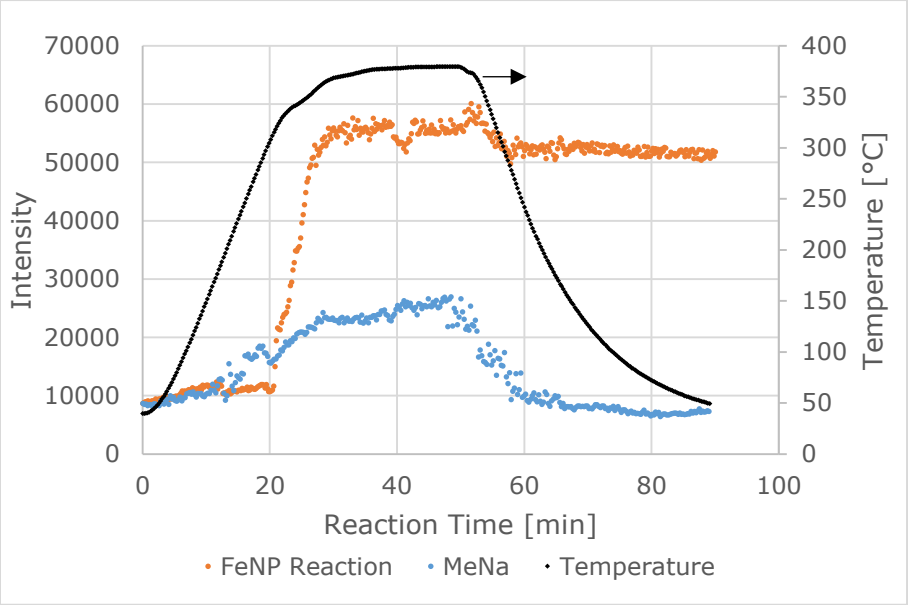

Figure 5.4: Backscattering signal of FeNP Reaction and MeNa at 655 nm

In the previous section, similar thermal treatment of the dispersion was studied to determine that even in the presence of particles the temperature increase cause proportional changes in the optical properties of the sample. The homogeneity of reactive solution in this case prior of the reaction allows us to study the change in the signal caused by the sudden appearance of particles as the result of a chemical reaction. As expected the behaviour the reaction backscattering trend changes proportionally with temperature like the case of the pure solvent and the dispersion presented previously in

section 4.4. of this work. The irreversibility of this process in the case of the reactive system however represent a fundamental difference.

In the case of pure solvent and/or disperse particles samples, where particles are already present from the start of the experiment, the signal intensity increases with the temperature and decreases almost to the initial values after the cooling stage while in the case of the reaction the much higher increase observed during the heating does not completely disappear even though a decrease is still observe at the cooling stage of the experiment. Comparing these results it is clear that the step increase in the backscattering intensity observed during the reaction does not corresponds to only the change in the optical properties. The magnitude of this difference between the initial and final intensity value only present in the reactive system compared with the pure solvent and the dispersion is evidence of the *in-situ* formation of particles and the capacity of the device to detect their generation with their substantial contribution to the overall backscattering of the sample after the reaction. It is important to clarify that the lower value of the intensity achieved by the solvent after the thermal treatment with respect to the initial value is caused by undesired reactions promoted by impurities present in the solvent causing a slight change of the final color observed on the liquid after the thermal treatment.

Demonstrated the capability of the device to detect the presence and measure the effect of the particle in the sample, sets of five reaction replicates were conducted for comparative purposes. The resulting evolution of the backscattering signal and reaction temperatures for five identical replicates with time is shown for the 532 and 655 nm lasers, these data are presented in figures 5.3. and 5.4., respectively.

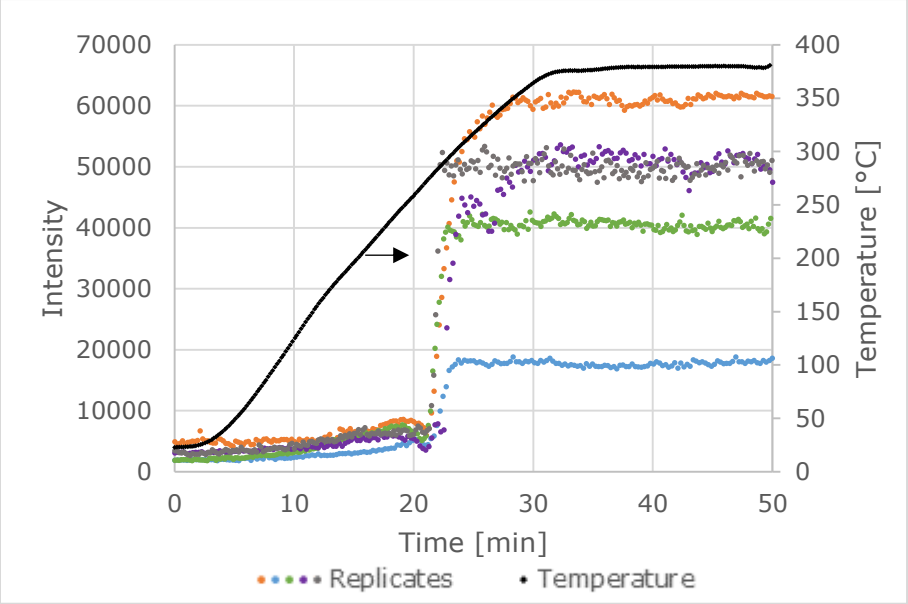

Figure 5.5: Iron Particles reaction Backscattering Signal at 532 nm

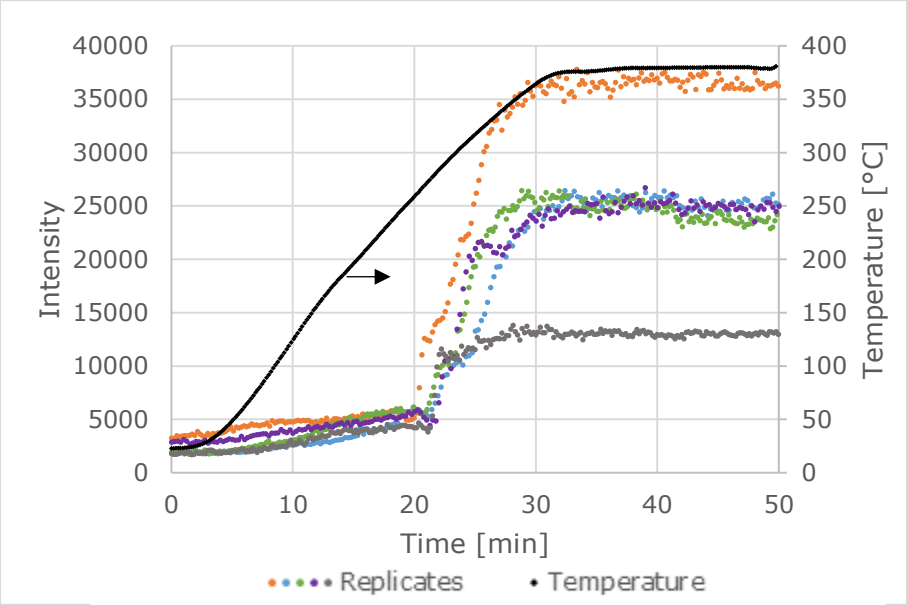

Figure 5.6: Iron Particles reaction Backscattering Signal at 655 nm

As mentioned before, at the start of the experiments the reactants solution is a black homogeneous liquid phase of iron naphthenate and carbon disulfide in 1-methylnaphthalene. Without the presence of particles, Figures 5.5. and 5.6. shows relatively low backscattering intensity values registered from the probe at the initial stage of each replicate. During the course of the experiment, the FeNa and CS_2 react to form FeS_x particles. A step change in the backscattering intensity takes place indicating this transformation after approximately 20 minutes and well below the temperature set

point selected for the reaction around 280 °C. The formation of the particles characterized by the sudden increase in the intensity takes approximately 5 min of reaction time, and once it happens no significant change is observed during the end of the heating ramp and the isothermal stage of the experiment. Similar experiments conducted at 200 and 250 °C further confirms this behaviour since no change in the backscattering trend was observed at those conditions. Further optimization of the reaction temperature was not studied in this project.

Inspection of the results presented in Figures 5.5. and 5.6. shows a significant and unexpected variation in the final backscattering intensities for each of the five replicates. To further analyse how the backscattering intensity at the later stages of the reaction is affected by the generated particles, e*x-situ* characterization for each of the reaction replicates was performed. These data are presented with the respective final intensity values in table 5.1.

Table 5.1: Final stage Particle reactions intensity and *Ex-situ* characterization

Reaction		**Replicate**					**Average**	**%DEV**
		1	**2**	**3**	**4**	**5**		
***Ex-situ* Mean Particle size [nm]**		135	134	132	122	118	128	7.7
Average Intensity ($_x10^3$)	**532 nm**	17.5	50.0	61.3	50.4	40.2	43.9	37.6
	655 nm	24.5	13.0	36.5	25.0	23.7	24.6	33.9

The data shows a considerably higher average standard deviation from the individual backscattering intensity measurements, regardless of the laser wavelength, compared to the deviation obtained from the *ex-situ* particle size characterization of each reaction product. The average *ex-situ* particle size on the other hand shows a good agreement with the individual particle size observed in the equivalent batch reaction micrographs, 100-200 nm. Based on this similarity it is likely that the system exhibits good dispersion under the reacting conditions and the particles did not significantly agglomerate *in-situ*.

Assuming full conversion of the soluble iron species into solid FeS and considering that the same reactant stock solution was used for each replicate to ensure identical initial concentration in each case, the maximum final particle concentration relative to the individual mean particle size can be estimated for each replicate. These results are shown along with the *ex-situ* particle size and final intensity value for each replicate in Figure 5.7.

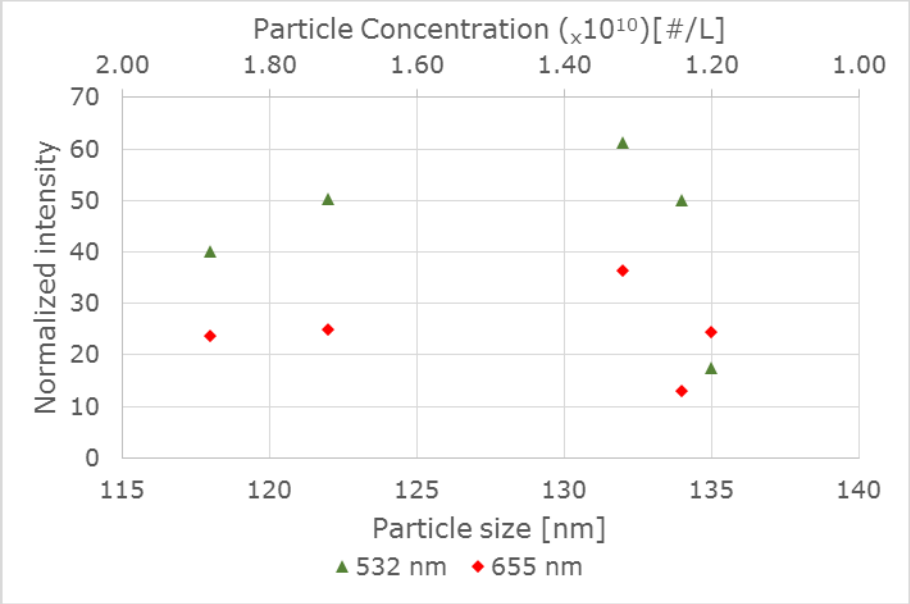

Figure 5.7: Normalized Intensity vs Particle size and concentration

Even though the increase in the final particle size obtained in each replicate is concomitant with a decrease in the particle concentration considering a fixed amount of reacting material in the sample, no correlation was found between the particle size and the average backscattering intensity in the replicates results. The behaviour of the normalized intensity obtained is expected to be more sensitive to the particle size considering that the Rayleigh's scattering theory predicts the backscattering intensity to increase in proportion with particle size to the power of six[25].

Based on the average particle size of 128 nm from the *ex-situ* characterization, a final particle concentration of $1.45x10^{10}$ #/L is calculated to be present in the reacting medium. This pair of particle concentration and size represent a mean inter-particle distance of 25 µm, which is roughly 200 times the average particle size. The magnitude of the spacing between particles is a critical factor in the agreement between the particle size obtained from the *ex-situ* characterization and the individual particles size observed in the micrographs confirming the premise of no particle agglomeration in the reacting media.

Beside particle size and concentration, the difference observed after the temperature stabilization in the reaction backscattering signal shown in Figures 5.5. and 5.6. can also be caused by differences in experimental conditions, laser power and fiber optics alignment. Given that the heating ramp during experiments and the final temperature were controlled to be nearly identical in all of the replicates, the effect of operating

conditions on the variation in the final intensity is minimal. Finally, variations in the laser outputs were considered to be negligible since both lasers were operated at maximum output and allowed to stabilize prior to each replicate. Considering all of those factors, the physical alignment of the probe is most likely the leading factor contributing to the observed differences in the final intensity between replicates. This effect, even though was also observed with the CB system, is more pronounced in this case since the initial presence of the particles in the dispersion gives a reference value of intensity for the alignment of the fibers during the setup of the device.

In order to continue the analysis of the differences obtained in the backscattering trends from individual reactions a normalization of the signal is required to correct for the previously discussed differences in the final intensity. This normalization consists of a percentage valuation of each replicate intensity relative to its initial and final condition. Figures 5.8. and 5.9. show the corresponding normalized intensity trends with temperature and reaction time for the 532 and 655 nm wavelength signal respectively.

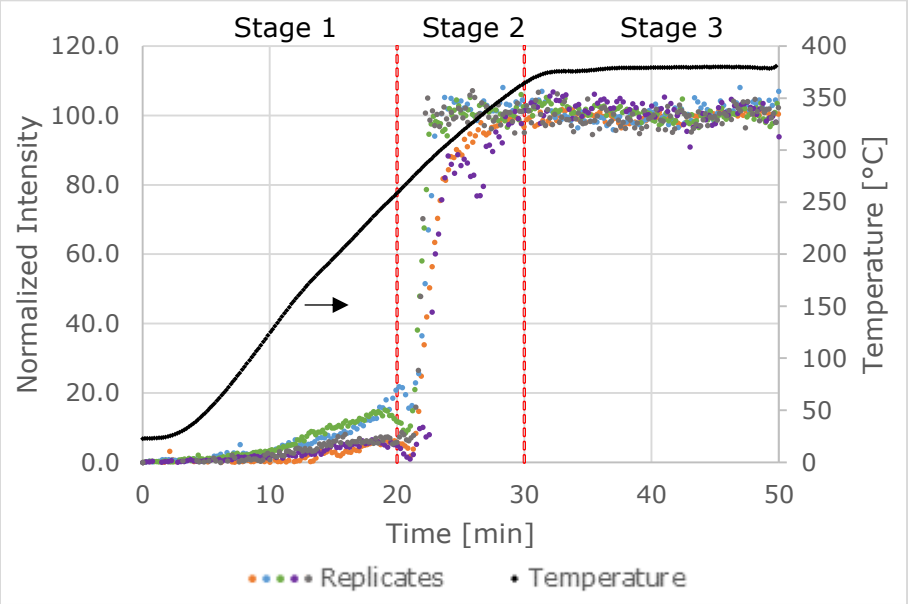

Figure 5.8: Normalized particles reaction signal at 532 nm

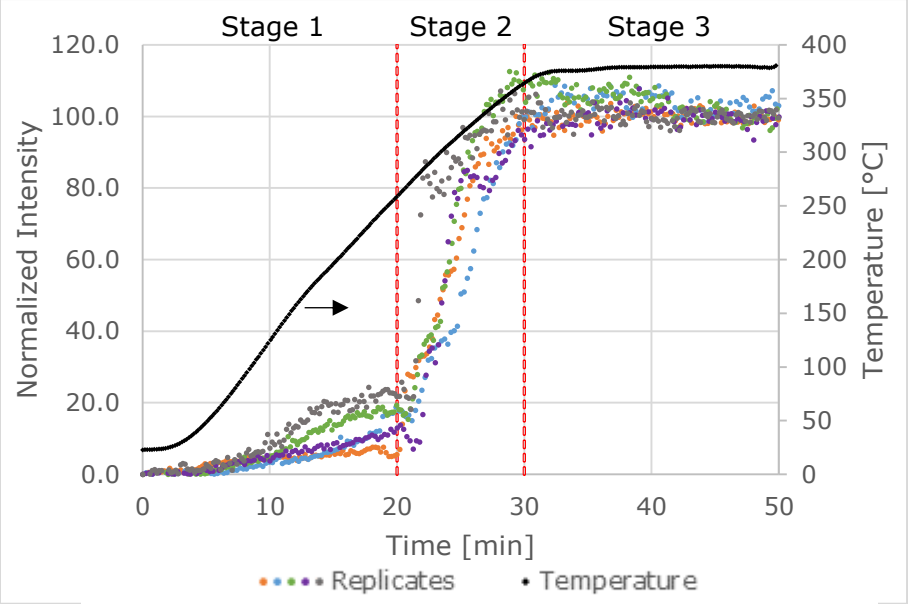

Figure 5.9: Normalized particles reaction signal at 655 nm

The normalization implemented clearly shows consistent similarities of the backscattering signal trend for each individual reaction, regardless the differences in the backscattering intensity magnitude, confirming the capability of the device to record signals representing the reacting medium. The trends also display three clearly differentiated stages at both the 532 and 655 nm wavelength cases:

- Initially, in Stage 1, the signal intensity gradually increases following the heating of the sample; this effect was also found in similar studies[22] and is attributable to the increase of the reflectance of the liquid sample due to the temperature increase.
- In Stage 2 there is an abrupt increase in the backscattering scattering detection. Considering the relation of the backscattering signal with the presence of particle, this effect is directly associated to the *in-situ* particle formation.
- In Stage 3, once the particles have been formed, the evolution of the scattering signal is controlled once more by the heating of the sample, increasing until the set point in temperature is reached and stabilizing afterwards in an average backscattering intensity value much higher with respect of the initial, homogeneous, conditions.

Previous studies focused on the iron particle generation as an *in-situ* catalyst for hydrogenation reactions[43,44], reason why conventional hydrogenating temperature such as 380 °C was selected for the study of the particle generation in this work, however further analysis of the similarities observed in the previous graphs offers additional information regarding the onset of the particle formation. Backtracking the time at which

the sudden change in the signal is obtained it is possible to identify the temperature on-set for this reaction under the conditions studied in this work at 274.6±0.7 °C. Other studies have found that the thermal decomposition of naphthenate-metal precursors under nitrogen happens around 300 °C for Copper and around 400 °C for Calcium[45], corresponding with the result obtained in this work for the case of Iron naphthenate.

Even though the scattering signal has proof to effectively give more information of the kinetic of the reaction, such as activation enery[22], further studies of these aspects are not part of the objectives of this work.

Much more complex reactive systems using Athabasca bitumen were also observed with this device under visbreaking conditions. Results obtain from such observations were inconclusive given the early stage of this technique and the complexity of the interpretation of these results, however, those results are presented in Appendix D. Further studies with such systems were beyond the scope of this research.

Changes in the physical configuration, namely the fiber optics placement in the holder, are likely to be the principal effect in the scale irreproducibility of backscattering behaviour from the reactive system. The effect of the fiber optics alignment was also obtained in the CB system, however its implication in the quantitative size estimation of the technique become irrelevant given that the information useful for the particle size characterization is obtain from the signal fluctuation analysis while the overall scale at which the intensity fluctuations is detected does not take any part in the size calculations.

Further understanding of the correlation between the backscattering signal intensity and the particle size may be use to further characterize particle concentration in the sample. However the scale mismatch between individual experiments cannot be interpret without removing the effect of the variability of fiber optics alignment in the measurement, preventing this characterization with the current configuration of the device. In order to address the poor reproducibility of the results which prevent the comparison of individual experiments, a new design focused on having the fibers permanently fixed and thus minimizing handling differences from individual characterizations is proposed later in this chapter.

SECTION 5.2. PARTICLE SIZE CHARACTERIZATION

As mentioned before the quantitative analysis of the intensity fluctuations is still possible allowing the particle size characterization with the current device. Having developed and

validated the data processing and calculation algorithm with the stable dispersion system, *in-situ* backscattering observations of iron naphthenate sulfidation were performed with the purpose of online particle sizing.

Based on the precision and reproducibility of particle size calculations made with CB system, six reactions were conducted in this case following similar procedure and operating conditions as before, with the exception of the reaction temperature set to 280 °C; closer to the onset of the particle generation determined in the previous section 5.1. Observations of the final product after the cooling stage of the reactor were made prior to the extraction of the sample for *ex-situ* characterization, in order to determine the calibration factor for this system at room temperature. Table 5.2. shows the results of such calculations.

Table 5.2: Calibration Factor C_{λ_0} for Iron Nanoparticles at room temperature

Replicate	$C_{532\ nm}$	**%Dev**	$C_{655\ nm}$	**%Dev**
1	1.21E-07	29.78	1.81E-07	19.35
2	1.40E-07	29.16	1.60E-07	31.76
3	1.70E-07	38.63	1.44E-07	33.41
4	1.50E-07	42.48	1.23E-07	26.84
5	1.59E-07	24.41	1.95E-07	29.47
6	1.43E-07	41.53	1.36E-07	57.88
Average	1.47E-07	34.33	1.57E-07	33.12
%Dev	11.48		17.71	

The table shows a reasonable agreement of the calibration factor values calculated for the *in-situ* generated iron nanoparticles compared with the calibration factor calculated for CB in the previous sections, 1.47_x10^{-7} and 1.85_x10^{-7} for 532 and 655 nm respectively. Even though this correspondence is desired, the calibration factor value is highly dependent on the particle-particle and particle-solvent interaction of each system. Considering the selection of both systems based on their similarity in the particle size, it is reasonable that particular differences in the particle nature in each case does not cause mayor differences in their behavior, considering the weak solvent-particle interactions promoted by the 1-Methylnaphthalene in both cases.

In order to further compare this results, a close comparison of the particle size distribution for both systems is presented in the following Figure 5.10.

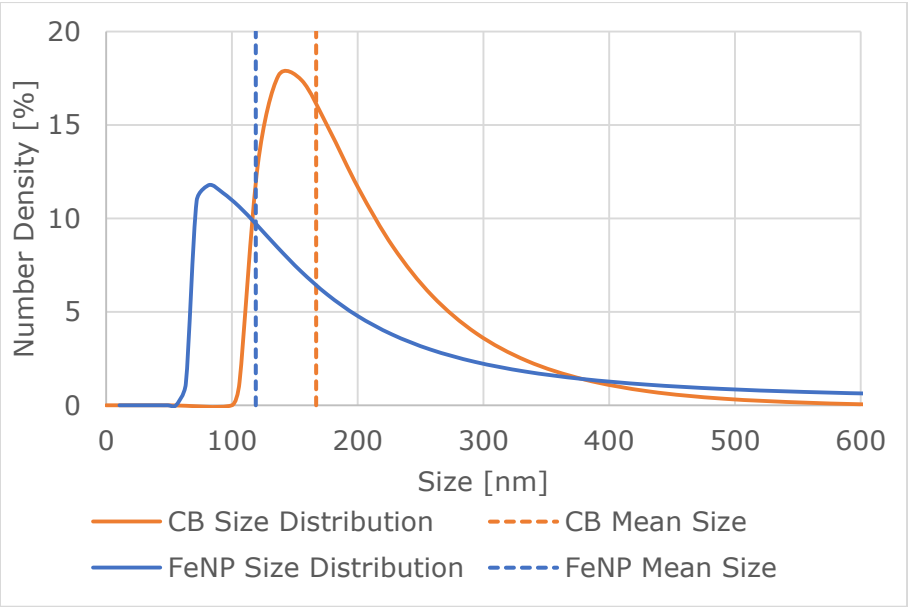

Figure 5.10: *Ex-situ* CB and FeNP Particle size distribution

The Figure 5.10. clearly shows a similarity in the mean particle size between both systems but also a considerable difference in terms of particle size distribution which for the case of FeNP is much broader than the case of CB. The particle size similarity was intentionally selected in order to have better comparison of both systems, the difference in the particle size distribution in the other hand is presumed to be the main cause for the much larger variability within individual measurement obtained in the case of FeNP, in the order of 30%, compared with the previous results obtained with CB dispersion, in the order of 10%. This effect with the additional variability of the reaction product inherent to a batch process, explains the increase in standard deviation of the calibration factor calculation.

Due to the inherent dynamic nature of a chemical reaction, control of the temperature was more difficult to achieve. Therefore interpretation of the whole set of measurements taken from each reaction requires individual data selection to discard the measurement affected by convective patterns caused by temperature gradients in the liquid. Figure 5.11. shows an example of the ACF linear fit slope with the temperature for each measurement.

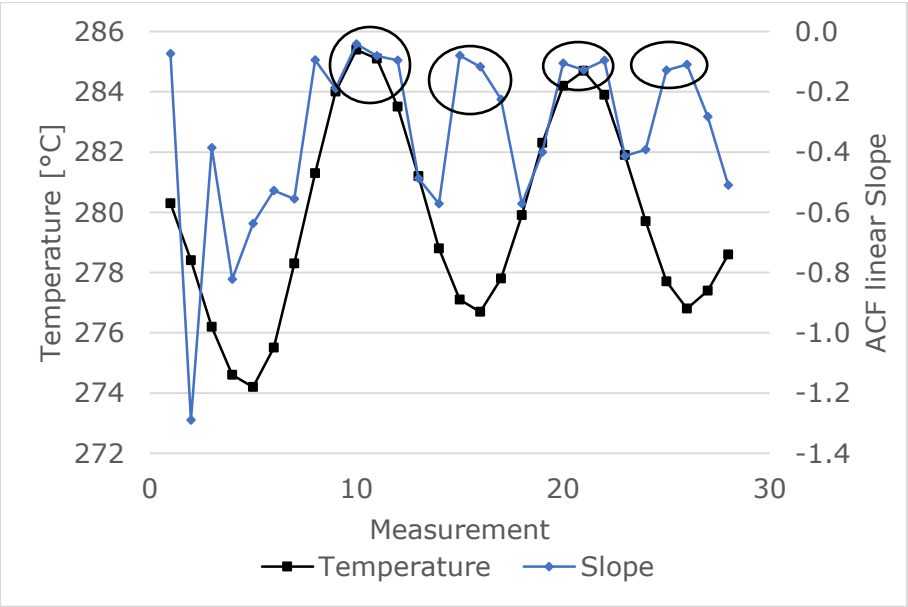

Figure 5.11: FeNP ACF behavior at High temperature

In the graph is shown how the ACF linear slope drastically changes shortly afterwards the valleys and peaks of the typical temperature sinusoidal control. As expected, the temperature fluctuation causes convective flow pattern that modifies the particle behavior in the sample, increasing the motion of the particles and therefore the magnitude of the ACF decay.

The existence of this effect it's intrinsically associated with the dynamics of the chemical reaction happening in the observation chamber and the difficulty of the temperature control system, reason why a different data filtration was required for the study of this sample in order to disregard the temperature fluctuation effects on the measurement and obtain useful information with the current setup. The data filtration in this case is based on selecting the ACF linear slope values corresponding with the temperature minimums and maximums, avoiding the transitional regions where the values of the slope are affected by the temperature gradients.

Considering that elevating the temperature in the signal is affecting the particle diffusion in the sample, as shown with the previous studies with the CB system, the calibration factor for *in-situ* characterization at high temperature requires adjustment from the room temperature values. In order to compensate for this effect the MeNa used as dispersant of the CB system and solvent for the FeNP reactions was selected to be identical in both cases and resilient to the operating conditions. Considering this similarity in terms of particle size and concentration between the systems and the

stability of the solvent to the operating conditions in both cases, it is assumed that the proportion in which the calibration factor changes from room to high temperature at each wavelength for the CB system can be extrapolated to the FeNP system as follow

$$C_{FeNP\ @280°C} = \left(\frac{C_{CB\ @280°C}}{C_{CB\ @roomT}}\right) C_{FeNP\ @roomT}$$

Considering this relation and having previously calculated the room temperature calibration factor of the FeNP system, the calibration factors estimated at high temperature are 1.77_x10^{-8} and 2.41_x10^{-8} for 532 and 655 nm respectively.

With these estimated high temperature calibration factor and the criteria implemented for the measurements selection, the particle size characterization of the iron nanoparticles in the reactive media is achieved following the calculation algorithm explained in previous sections, table 5.3. summarizes the results. See appendix C2 for the detailed calculation code.

Table 5.3: *In-situ* iron nanoparticles average particle size at high temperature

Replicate	*Ex-situ* [nm]	*In-situ*			
		532 nm		655 nm	
		Size [nm]	%Error	Size [nm]	%Error
1	111.0	198.2	78.52	198.5	78.87
2	111.0	167.4	50.83	178.8	61.12
3	145.0	184.4	27.20	191.3	31.90
4	145.0	263.7	81.84	273.6	88.71
5	145.0	196.5	35.53	182.8	26.07
6	132.0	202.1	53.09	190.5	44.33
Average	131.5	202.0	54.50	202.6	55.17
%Variability	16.7	32.7		35.5	

The table shows relatively the same variability within each replicate, similar deviation towards bigger particle size and equivalent relative error between the *in-situ* calculated value and the *ex-situ* characterization, compared with the results obtained from the CB system. This similarity lead us to support the assumption made in order to estimate the high temperature calibration factor of the iron nanoparticle system, validating the use of this approach as particle size characterization technique.

It is important to highlight that in this case the majority of the liquid phase correspond to the solvent 1-methylnaphthalene which due to its high temperature resilience does not undergoes major chemical changes during the reaction time. This property of the

solvent was carefully selected for this study given that the optical properties of the continuum phase are approximated to the pure solvent throughout the entire temperature range and reaction time. In situations where the solvent composition changes bringing major differences in the refractive index of the medium, this approximation cannot be done requiring additional quantitative ways to estimate or measure online the refractive index of the medium.

Similarly as before t-test of the results for each wavelength were conducted finding a factor t=0.91 proving again the validity of using the characterization from both wavelength simultaneously, obtaining an overall particle size average of 202.3±32.5 nm with 53.86% error relative to the *ex-situ* characterized particle size.

Is important to mention that having available an instrument such as the one developed in this work may allow much better process control and optimization of the existing particle based processes, such as the HCAT process mentioned at the beginning of this manuscript, as well as allows new developments inclined to tailor particle based processes to produce more specific morphologies such as core-shell type of particles, currently with high interest in the catalysis field; by promoting a step process in which the formation of a controlled particle size core from an inexpensive material serves as backbone for a subsequent reaction in which the active (high value) catalysts material is grown as shell of the previous particle maintaining individual control of both core and shell sizes and activity in each step.[46]

Due to time limitations of this project, the manufacture and assessment of a new version of the device designed specifically to avoid the issues encounter during this research was not possible. However a full description of a new fiber optics holder is presented in the following section.

SECTION 5.3. REDESIGN OF THE DEVICE

As mentioned before, the alignment of the fiber optics in the configuration has been determined to be the principal limiting factor for the reproducibility in the intensity scale of individual results, preventing the comparison whiting experiments. Figure 5.13., shows a graphic representation of a new fiber optics holder design, which looks to address this issue maintaining from the current configuration the advantages of using 8 mm thickness sapphire window for better mechanical properties and enhanced scattering signal in contrast with YAG and 4mm thickness respectively. It also retain the use of

individual 800μm core diameter fused silica fibers to illuminate and collect the sample scattering.

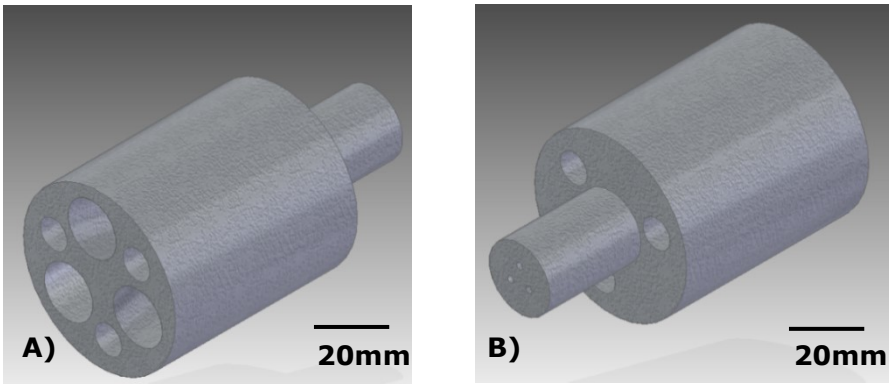

Figure 5.12: Fiber optic holder Mark 2 a) Front, b) Back

In the back of the piece, Figure 5.12. A), 2 set of cavities are showed: the 3 smaller holes, of 4.5mm Φ, close to the edges of the cylinder, of 22mm Φ, are in place for cooling purposes which in contrast with the previous design goes throughout the entire 25mm length of the back cylinder creating a cooling flow through the piece. The additional 3 bigger holes of 8mm Φ, goes 8mm deep into the big cylinder body concentric to the fiber channels, match the commercial specifications of a SMA female adapter to serve as a connector for the external fiber optics plugged into the laser sources and detector respectively. Meanwhile in the front of the piece, Figure 5.13. B), is shown a smaller cylinder body of 10mm Φ and 15mm length that fit inside the existing threaded gland and reaches the outer surface of the window. In this view are also shown the 3 fiber channels, equally spaced from each other.

In order to maintain the compact size of the instrument the fiber channel in this design are inclined from the longitudinal axis of the holder piece, causing the fiber termination to be angle-ended. This called tilt-angle (ε) between the normal of the surface and the core axis of the fiber causes face of the cylindrical core to be reshaped into an ellipse and the aperture angle of acceptance light cone (θ_a) to be refracted in contrast to the traditional termination, changing the geometry of the propagating light. In the Figure 5.13. the difference of the light propagation profile between traditional perpendicular termination and the angled termination are showed.

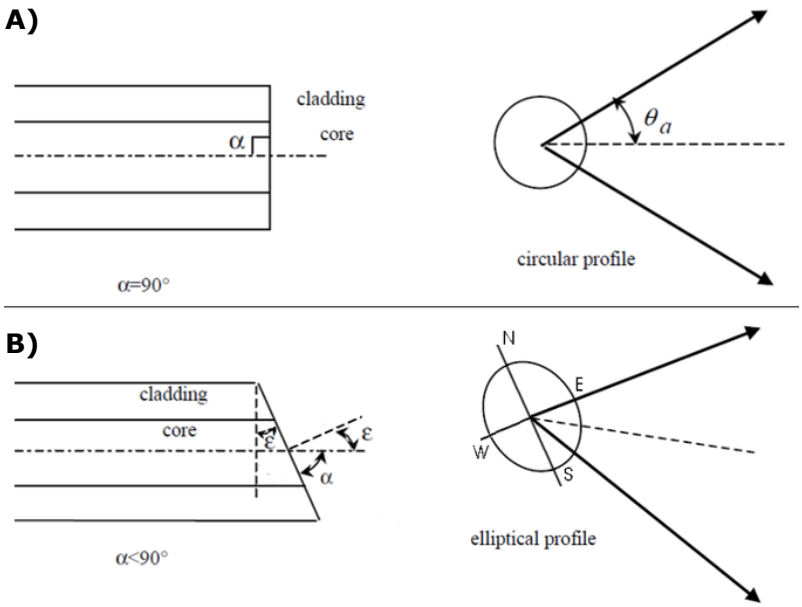

Figure 5.13: a) Perpendicular Termination, b) Angle-ended Termination.[47]

(used with permission)

The refracted acceptance cone angles are calculated in two different light propagation scenarios: through the minor axis WE and mayor axis NS. In the first case the light propagation occurs similar to the straight face case with an acceptance cone with θ_a, obtained by Eq. 2.22 explained in the chapter 2, however in the former case the refraction between the normal of the elliptical face and the rays of light propagating alongside the fiber core plane varies significantly depending on the value of ε[47,48]. Detailed information on the calculation for this scenario is provided in Appendix E.

The introduced changes in the light propagation geometry caused by the tilt-angle greatly modify the scattering area at the window-sample interface compared with the old design. Iterative calculation were made in order to determine the tilt-angle and core spacing of the new design maintaining a small distance between the acceptance cones in the inner crystal-sample interface, results of these calculations are summarized in table 5.4.

Table 5.4: Scattering Area from different device configurations

	Tilt Angle (ε) [°]	Window Thickness [mm]	Core Spacing [mm]	Crystal-Sample light cone spacing [mm]
Used design	0	4	3	1.2
	0	8	3	0.2
New design	10	8	2	0.6

Finally simulations in COMSOL Multiphysics 5.0, similarly to the current design, were made to determine the minimum diameter for the cooling channel required to maintain a maximum temperature of 60°C at the connection point with the external SMA fiber optics. Figure 5.14. shows the result from the heat transfer simulation

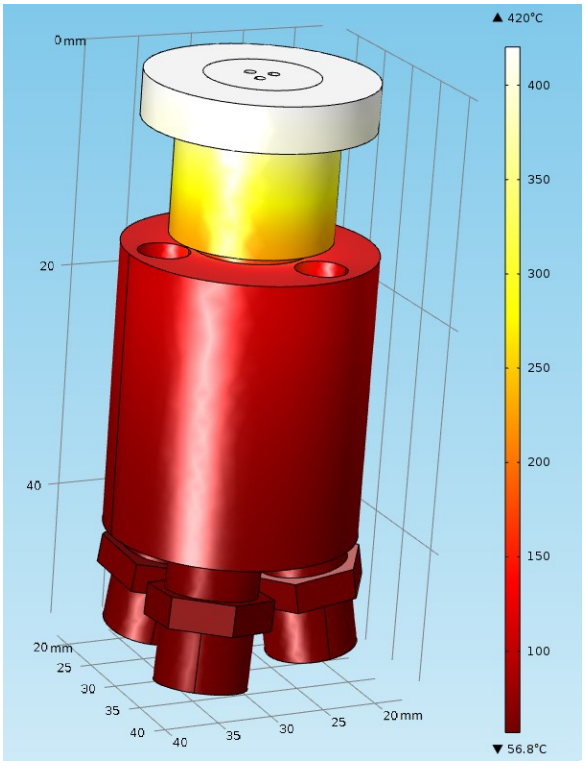

Figure 5.14: Temperature profile of the new holder design

The robust body surrounding the fibers in the new design allows to incorporate a faster 15m/s of cooling air at 25°C required to maintain the connection point below the maximum temperature.

Chapter 6: CONCLUSIONS AND RECOMMENDATIONS

SECTION 6.1. CONCLUSIONS

Based on the experimental work made in this project, the following conclusions can be drawn regarding the development of an online particle size analyzer used to study the *in-situ* generation of iron based nanoparticles

- The fiber optics arrangement proposed in this project proved to be resilient to elevated temperature and pressure, maintaining the sensitivity to detect the presence of particles.
- The C-Axis oriented Sapphire of 8mm thickness proved to be the best configuration, from the options studied with this device, for *in-situ* particle size characterizations.
- Real-time characterization of the average particle size was achieved by the implementation of the Diffuse Wave Approximation theory at room temperature and 280 °C.
- Changes in the optical properties related to chemical reactions can be detected under operating conditions by the device developed in this project.
- In the presence of hydrogen the *in-situ* iron based nanoparticles are spherical shaped while in the presence of nitrogen the particles take rod-like shapes.
- Temperature onset for the particle generation by sulfidation of iron naphthenate under the conditions studied in this work was determined to be 274.6±0.7 °C.
- Iron based nanoparticles produced in this work were *in-situ* characterized at 280 °C obtaining 202±33 of average particle size.

SECTION 6.2. RECOMMENDATIONS AND FUTURE WORK

It is important to highlight that due to the novelty of the online characterization at high temperatures, simplicity was the main design criteria used in the development of the device used for this project. After demonstrating the capabilities of such approach, mayor improvements are needed to further develop the characterization technique.

- Manufacture and assessment of the proposed redesign explained in the section 5.3. of this work.

- The effect of the particle concentration on the particle-particle interactions and propagation of the light must be studied both at room and high temperature conditions to further understand and validate this technique
- Development of the technique to estimate particle concentration can be done by empirical correlations including temperature and refractive index once the reproducibility issues encountered during this study are taken care of.
- In order to make the device more robust and more industrially feasible, a controlled flow pattern of the liquid phase must be included in the study to represent more realistic stirring conditions in comparison to Brownian Motion.
- Higher acquisition rate spectrometers or more complex optical arrangements with ultrafast digital correlators should be considered to enhance the current particle size resolution.
- Further studies of the effects of the medium in the final shape of the *in-situ* generated iron based particles should be done to understand the mechanism in which hydrogen influence the final shape of the particles in order to tailor reaction conditions to obtain the desires characteristics of the particles.
- The effect of nucleation sites in the reacting media over the formation of iron based nanoparticles and their final average particle size can be studied with this technique.
- Further studies with different temperature ramps can be done with this technique to extract kinetic information of the selected particle based reaction.

BIBLIOGRAPHY

1. Bagheri, S. R. Mesophase Formation in Heavy Oil. University of Alberta, Edmonton, 2012.

2. Castañeda, L. C.; Muñoz, J. A. D.; Ancheyta, J., Current situation of emerging technologies for upgrading of heavy oils. *Catalysis Today* **2014,** *220-222*, 248-273.

3. Xu, R., *Particle characterization. [electronic resource] : light scattering methods*. New York : Kluwer Academic, c2002.: 2002.

4. Shibayama, M.; Karino, T.; Okabe, S., Distribution analyses of multi-modal dynamic light scattering data. *Polymer* **2006,** *47* (18), 6446-6456.

5. Dhadwal, H. S.; Ansari, R. R.; Meyer, W. V., A fiber-optic probe for particle sizing in concentrated suspensions. *Review of Scientific Instruments* **1991,** *62* (12), 2963.

6. Schmitz, K. S., *An introduction to dynamic light scattering by macromolecules. [electronic resource]*. Boston : Academic Press, ©1990.: 1990.

7. Pecora, R., *Dynamic light scattering : applications of photon correlation spectroscopy*. New York : Plenum Press, c1985.: 1985.

8. University of Washington Departments Web Server. http://depts.washington.edu/cmditr/modules/lum/electromagnetic_radiation.html (accessed July 10, 2016).

9. Schärtl, W., Light scattering from polymer solutions and nanoparticle dispersions. In *Springer laboratory manuals in polymer science* [Online] Springer: Berlin, 2007; pp. xiv, 191.

10. Wells-Gray, E. M. Development and application of dynamic light scattering methods for charcaterizing reaction kinetics. Oregon Health & Science University, 2011.

11. Gun'ko, V. M.; Klyueva, A. V.; Levchuk, Y. N.; Leboda, R., Photon correlation spectroscopy investigations of proteins. *Advances in Colloid and Interface Science* **2003,** *105* (1–3), 201-328.

12. Chu, B., *Laser light scattering : basic principles and practice*. Boston : Academic Press, c1991.: 1991.

13. Scheffold, F., Particle Sizing with Diffusing Wave Spectroscopy. *Journal of Dispersion Science & Technology* **2002,** *23* (5), 591.

14. Krieger, U. K.; Zardini, A. A., Using dynamic light scattering to characterize mixed phase single particles levitated in a quasi-electrostatic balance. *Faraday Discussions* **2008,** *137*, 377-388.

15. Scheffold, F.; Cerbino, R., New trends in light scattering. *Current Opinion in Colloid & Interface Science* **2007,** *12* (1), 50-57.

16. Pine, D. J.; Weitz, D. A.; Zhu, J. X.; Herbolzheimer, E., Diffusing-wave spectroscopy: dynamic light scattering in the multiple scattering limit. *Journal de Physique Archives* **1990,** *51* (18), 2101 - 2127.

17. Horne, D. S.; Davidson, C. M., Application of diffusing-wave spectroscopy to particle sizing in concentrated dispersions. *Colloids and Surfaces A: Physicochemical and Engineering Aspects* **1993,** *77*, 1-8.

18. Pine, D. J.; Weitz, D. A.; Chaikin, P. M.; Herbolzheimer, E., Diffusing wave spectroscopy. *Physical Review Letters* **1988,** *60* (12), 1134-1137.

19. Potenza, M. A. C.; Pescini, D.; Magatti, D.; Ferri, F.; Giglio, M., A new particle sizing technique based on near field scattering. *Nuclear Physics B Proceedings Supplement* **2006,** *150* (1), 334-338.

20. Fiber-Optic Performance Factors. http://cablingfiberoptic.blogspot.ca/2012/01/fiber-optic-performance-factors.html (accessed July 10, 2016).

21. Khalili, K. N. Development, Implementation And Validation Of In-Situ Raman Hot Stage Reactor. University of Alberta, Edmonton, 2014.

22. Dinh, D. In-Situ Observation of Heavy-Oil Cracking using Backscattering Optical Techniques. University of Alberta, Edmonton, 2015.

23. Zelmon, D. E.; Small, D. L.; Page, R., Refractive-index measurements of undoped yttrium aluminum garnet from 0.4 to 5.0 micrometers. *Applied Optics* **1998,** (21), 4933.

24. Malitson, I. H., Refraction and Dispersion of Synthetic Sapphire. *Journal of the Optical Society of America (1917-1983)* **1962,** *52* (12), 1377.

25. Rega, C.; Lloyd, C. J.; Attwood, D.; Clarke, D.; Geraghty, P., Temporal autocorrelation function for a diffusing-wave spectroscopy experiment with a point source and backscattering detection. *APPLIED OPTICS* **2001,** *40* (24), 4204-4209.

26. Brown, R. G. W., DYNAMIC LIGHT-SCATTERING USING MONOMODE OPTICAL FIBERS. *APPLIED OPTICS* **1987,** *26* (22), 4846-4851.

27. Wiese, H.; Horn, D., FIBEROPTIC QUASI-ELASTIC LIGHT-SCATTERING IN CONCENTRATED LATEX DISPERSIONS - THE PERFORMANCE OF SINGLE-MODE VS MULTIMODE FIBERS. *BERICHTE DER BUNSEN-GESELLSCHAFT-PHYSICAL CHEMISTRY CHEMICAL PHYSICS* **1992,** *96* (12), 1818-1828.

28. Utzinger, U.; Richards-Kortum, R. R., Fiber optic probes for biomedical optical spectroscopy. *JOURNAL OF BIOMEDICAL OPTICS* **2003,** *8* (1), 121-147.

29. Brenci, M.; Mencaglia, A.; Mignani, A. G.; Pieraccini, M., Circular-array optical-fiber probe for backscattering photon correlation spectroscopy measurements. *Applied Optics* **1996,** (34), 6775.

30. Myakov, A.; Nieman, L.; Wicky, L.; Utzinger, U.; Richards-Kortum, R.; Sokolov, K., Fiber optic probe for polarized reflectance spectroscopy in vivo: Design and performance. *JOURNAL OF BIOMEDICAL OPTICS* **2002,** *7* (3), 388-397.

31. Munzke, D.; Saunders, J.; Omrani, H.; Reich, O.; Loock, H. P., Modeling of fiber-optic fluorescence probes for strongly absorbing samples. *APPLIED OPTICS* **2012,** *51* (26), 6343-6351.

32. Coda, S.; Thompson, A. J.; Kennedy, G. T.; Roche, K. L.; Ayaru, L.; Bansi, D. S.; Stamp, G. W.; Thillainayagam, A. V.; French, P. M. W.; Dunsby, C., Fluorescence lifetime spectroscopy of tissue autofluorescence in normal and diseased colon measured ex vivo using a fiber-optic probe. *BIOMEDICAL OPTICS EXPRESS* **2014,** *5* (2), 515-538.

33. Beswick, K.; Baumgardner, D.; Gallagher, M.; Volz-Thomas, A.; Nedelec, P.; Wang, K. Y.; Lance, S., The backscatter cloud probe - a compact low-profile autonomous optical spectrometer. *Atmospheric Measurement Techniques* **2014,** *7* (5), 1443-1457.

34. Lee Black, D., Laser-based techniques for particle-size measurement: A review of sizing methods and their industrial applications. *Progress in Energy and Combustion Science* **1996,** *22* (3), 267.

35. Weitz, D. A.; Zhu, J. X.; Durian, D. J.; Pine, D. J., *Principles and Applications of Diffusing-Wave Spectroscopy*. Springer Netherlands: 1992; Vol. IV, p 731-748.

36. Keuren, E. R. V.; Wiese, H.; Horn, D., Diffusing-wave spectroscopy in concentrated latex dispersions: An investigation using single-mode fibers. *Colloids and Surfaces A: Physicochemical and Engineering Aspects* **1993,** *77*, 29-37.

37. Scheffold, F.; Shalkevich, A.; Vavrin, R.; Crassous, J.; Schurtenberger, P. In *PCS Particle Sizing in Turbid Suspensions: Scope and Limitations*, Harris, M. T.; Texter, J., Eds. Washington DC, American Chemical Society, [Oxford], Oxford University Press [distributor]: 2004; pp 3-32.

38. Chen, G.; Hou, Y.; Knapp, H., Diffusion Coefficients, Kinematic Viscosities, and Refractive Indices for Heptane + Ethylbenzene, Sulfolane + 1-Methylnaphthalene, Water + N,N-Dimethylformamide, Water + Methanol, Water + N-Formylmorpholine, and Water + N-Methylpyrrolidone. *JOURNAL OF CHEMICAL AND ENGINEERING DATA* **1995,** *40* (4), 1005.

39. Vargas, F. M.; Chapman, W. G., Application of the One-Third rule in hydrocarbon and crude oil systems. *Fluid Phase Equilibria* **2010,** *290*, 103-108.

40. Iglesias-Otero, M. A.; Troncoso, J.; Carballo, E.; Romaní, L., Density and refractive index in mixtures of ionic liquids and organic solvents: Correlations and predictions. *The Journal of Chemical Thermodynamics* **2008,** *40*, 949-956.

41. Krishnaswamy, R. K.; Janzen, J., Test Method: Exploiting refractometry to estimate the density of polyethylene: The Lorentz–Lorenz approach re-visited. *Polymer Testing* **2005,** *24*, 762-765.

42. Hulst, H. C. v. d., *Light scattering by small particles*. New York, NY : Dover Publications, Inc., 1981

43. Tang, Y.; Curtis, C. W., ACTIVITY AND SELECTIVITY OF SLURRY-PHASE IRON-BASED CATALYSTS FOR MODEL SYSTEMS. *ENERGY & FUELS* **1994,** *8* (1), 63-70.

44. Curtis, C. W.; Chen, J. H.; Tang, Y., HYDRODESULFURIZATION OF MODEL SYSTEMS USING - SLURRY-PHASE CATALYSTS. *ENERGY & FUELS* **1995,** *9* (2), 195-203.

45. Yaegashi, S.; Moffatt, W. C.; Murakami, H.; Nishino, J. y.; Shiohara, Y., Preparation of superconducting thin films of $Bi_2Sr_2CaCu_2O_y$ by metallo-organic decomposition method. 1989.

46. Xiaohong, W.; Beibei, H.; Zhiyu, H.; Zhigang, Z.; Sheng, H., Current advances in precious metal core–shell catalyst design. *Science & Technology of Advanced Materials* **2014,** *15* (4), 1-1.

47. Gao, C.; Farrell, G., Numerical aperture characteristics of angle-ended plastic optical fiber [4876-73]. *PROCEEDINGS- SPIE THE INTERNATIONAL SOCIETY FOR OPTICAL ENGINEERING* **2002,** (4876), 404-415.

48. Kovacevic, M. S.; Djordjevich, A.; Nikezic, D., Effects of end-face tilt angle on numerical aperture for straight and bent plastic optical fibers. *FIBER AND INTEGRATED OPTICS* **2007,** *26* (2), 111-122.

49. Ugural, A. C., *Stresses in beams, plates, and shells*. Taylor & Francis Group, LLC, 3rd ed.: 2009.

50. Koechner, W., Rupture stress and modulus of elasticity for Nd:YAG crystals. *Applied Physics* **1973,** *2* (5), 279.

APPENDIX A: REACTOR PARTS DETAILS

Appendix A covers in details the different parts of the reactor used in this work

APPENDIX A1: ONLINE OBSERVATIONS REACTOR

The bottom reactor Nut and Fiber Optics Holder, as well as the inside thread modification of the Gland were custom made by the Chemical and Material Engineering Department Machine Shop.

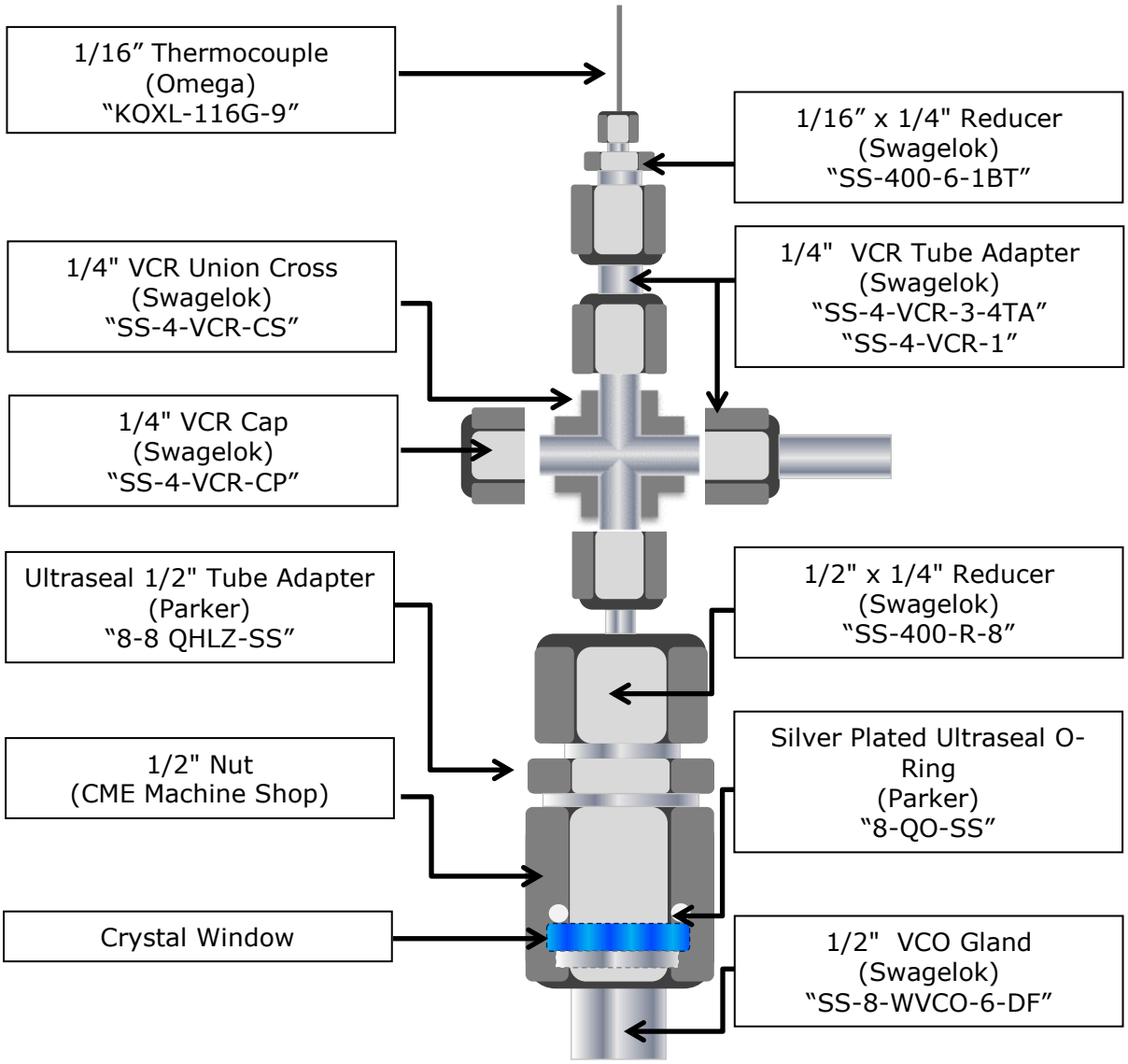

Figure A.1: Online Observations reactor parts details

APPENDIX A2: MICROBATCH REACTOR

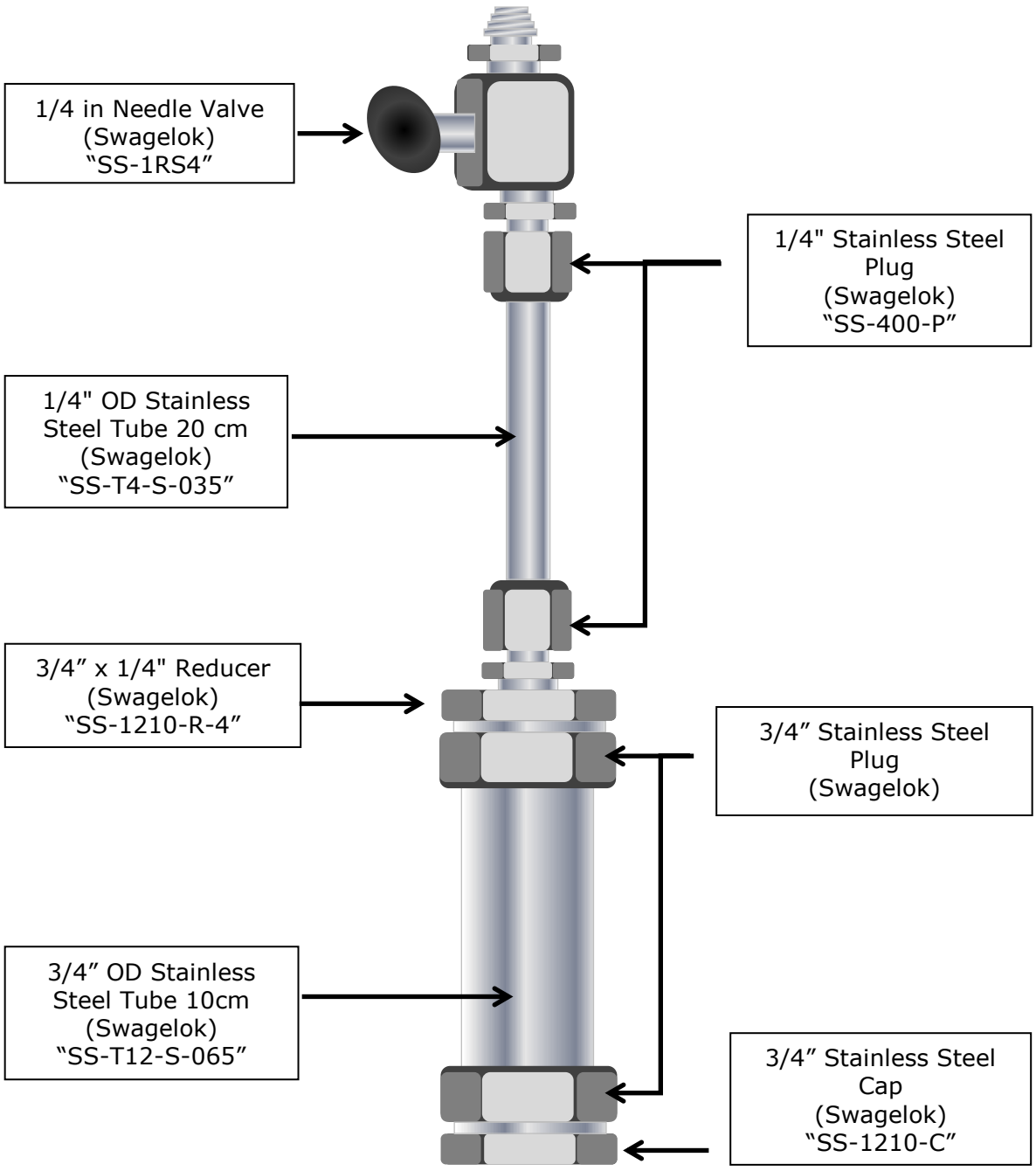

Figure A.2: Microbatch Reactor Parts Details

APPENDIX B: WINDOW THICKNESS CALCULATION

The maximum stress a circular plate uniformly loaded can tolerate is predicted by the maximum energy of distortion theory with the following equation[49]

$$\sigma_{max} = \frac{K*\Delta P*R^2}{4*t^2} * SF \qquad \text{Eq. B.1}$$

Where K is an empirical factor that depends on the method of support, ΔP is the pressure differential, R is the unsupported radius of the window, t is the thickness of the window slab and SF the safety factor

This configuration is operated in this project to a maximum pressure of 5MPa. Given that the window is placed over the gland unclamped, a typical value of K in unclamp assemblies is 1.125. Moreover the inclusion of the gland below the window reduce the unsupported window area of the reactor configuration to 10 mm from the previous arrangement. Using the modulus of rupture as the stress value at which the crystal material suffer breakage, the minimum thickness can be obtained from this equation.

Considering the high temperature experiments, it has been previously studied[49] that the rupture modulus of Sapphire has a particular dependence with temperature, exhibiting a dramatic decrease from the room temperature values. Table B.1. summarizes the minimum thickness calculations for both crystal materials under the operating conditions considering a safety factor of 4, minimum traditionally used for this kind of applications.

Table 5 Window thickness calculation

Material	Operating Temperature [°C]	Rupture Modulus [MPa]	Minimum Thickness [mm]	Actual Thickness [mm]
Yttrium aluminum garnet (Yag)	25	262[50]	1.47	4
Aluminum oxide (Sapphire)	25	706[49]	0.89	4 & 8
	350	245[49]	1.52	8

The minimum thickness calculated proofs safe operation with the windows selected for this project. It is important to note that the significant overdesign in terms of windows thickness used mainly caused by the availability from previous projects in the same research group that operated at much severe operating conditions.

APPENDIX C: CALCULATION ROUTINE CODE

APPENDIX C1: NORMALIZED IACF CALCULATION

```
clc,clear, close
display('Please Select files');
[f,p,fi]=uigetfile({'*.txt'},'Select files','.','MultiSelect','on');
d=length(f);
dataG=zeros(8003,1);
dataR=zeros(8003,1);
G=zeros(8000,1);
R=zeros(8000,1);
srtau=zeros(8000,1);
Gmat=zeros(8000,d);
Rmat=zeros(8000,d);
g2Gmat=zeros(8000,d);
g2Rmat=zeros(8000,d);

%Signal Read%
for n=1:d;
fname = strcat(p,f{n});
fid=fopen(fname);
fileG=textscan(fid,'%f',8003,'headerlines',17,'delimiter',';');
fileR=textscan(fid,'%f',8003,'headerlines',219,'delimiter',';');
fclose(fid);
dataG=fileG{1,1};
dataR=fileR{1,1};
    for i=1:8000;
        G(i,1)=dataG(i+3,1);
        R(i,1)=dataR(i+3,1);
        srtau(i)=sqrt(i);
    end;

%autocorrelation%
    L=length(G);
    G2G=xcorr(G);
    G2R=xcorr(R);
    G2G=G2G(1:L);
    G2R=G2R(1:L);
    g2G=(G2G./tau)/mean(G)^2;
    g2R=(G2R./tau)/mean(R)^2;

%matrix results%
    for i=1:8000
        g2Gmat(i,n)=g2G(i,1);
        g2Rmat(i,n)=g2R(i,1);

    end
end;
```

APPENDIX C2: NORMALIZED FIELD AUTOCORRELATION LINEAR FIT

```
clc,clear, close
display('Please Select files');
[f,p,fi]=uigetfile({'*.txt'},'Select files','.','MultiSelect','on');
d=length(f);
dataG=zeros(8003,1);
dataR=zeros(8003,1);
G=zeros(8000,1);
R=zeros(8000,1);
srtau=zeros(2000,1);
G8=zeros(2000,4);
R8=zeros(2000,4);
G1=zeros(2000,1);
R1=zeros(2000,1);
g1G=zeros(2000,1);
g1R=zeros(2000,1);
g1Gmat=zeros(2000,4);
g1Rmat=zeros(2000,4);
lg1G=zeros(2000,1);
lg1R=zeros(2000,1);
slopeGmat=zeros(d,4);
slopeRmat=zeros(d,4);

%Signal Read%
for n=1:d;
fname = strcat(p,f{n});
fid=fopen(fname);
fileG=textscan(fid,'%f',8003,'headerlines',17,'delimiter',';');
fileR=textscan(fid,'%f',8003,'headerlines',219,'delimiter',';');
fclose(fid);
dataG=fileG{1,1};
dataR=fileR{1,1};
    for i=1:8000;
        G(i,1)=dataG(i+3,1);
        R(i,1)=dataR(i+3,1);
    end;
    for i=1:2000;
        srtau(i)=sqrt(i);
    end

%autocorrelation%
    for k=1:4;
        for i=1:2000;
            G8(i,k)=G(2000*(k-1)+i,1);
            R8(i,k)=R(2000*(k-1)+i,1);
            G1(i,1)=G8(i,k);
            R1(i,1)=R8(i,k);
        end
    L=length(G1);
    G2G=xcorr(G1);
    G2R=xcorr(R1);
    G2G=G2G(1:L);
    G2R=G2R(1:L);
    g2G=(G2G./tau)/mean(G1)^2;
    g2R=(G2R./tau)/mean(R1)^2;
```

```
    g1G=real(sqrt((g2G-1)/(g2G(1)-1)));
    g1R=real(sqrt((g2R-1)/(g2R(1)-1)));
    for i=1:2000
        g1Gmat(i,k)=g1G(i,1);
        g1Rmat(i,k)=g1R(i,1);
    end

%selection for fit%
     for i=2:2000;
        if g1G(i,1)>0;
            if lg1G(i-1,1)>1;
            lg1G(i,1)= 2;
            else
            lg1G(i,1)=log(g1G(i,1));
            end;
        else
            lg1G(i,1)=2;
        end;
        if g1R(i,1)>0;
            if lg1R(i-1,1)>1;
            lg1R(i,1)=2;
            else
            lg1R(i,1)=log(g1R(i,1));
            end;
        else
            lg1R(i,1)=2;
        end
     end

%fit%
    ft=fittype('a*x','independent','x','dependent','y');
    IG=lg1G>1;
    outG=excludedata(srtau,lg1G,'indices',IG);
optsG=fitoptions('Method','NonlinearLeastSquares','Exclude',outG,'StartPo
int',1);
    IR=lg1R>1;
    outR=excludedata(srtau,lg1R,'indices',IR);
optsR=fitoptions('Method','NonlinearLeastSquares','Exclude',outR,'StartPo
int',1);
    fitlg1G=fit(srtau,lg1G,ft,optsG);
    coefG=coeffvalues(fitlg1G);
    slopeGmat(n,k)=coefG(1,1);
    fitlg1R=fit(srtau,lg1R,ft,optsR);
    coefR=coeffvalues(fitlg1R);
    slopeRmat(n,k)=coefR(1,1);
    end
end;
```

APPENDIX D: ATHABASCA VACUUM RESIDUE VISBREAKING ONLINE OBSERVATION.

Additional observation were made with the device in this case to study the visbreaking reaction of Athabasca Vacuum residue at 420 °C; following a similar procedure as with the particle reaction system described in sections 3.2.2 and 3.2.3.1.

Given that the ultimately objective of this research is to develop a technique capable of giving better insight of the mesophase reactions studied in previous researches[1, 22], an extra validation stage of this development was to confirm the capability of this configuration to obtain similar results in terms of signal backscattering behavior with reaction time. Figures D.1. and D.2. shows the respective backscattering signals at 532nm and 655nm.

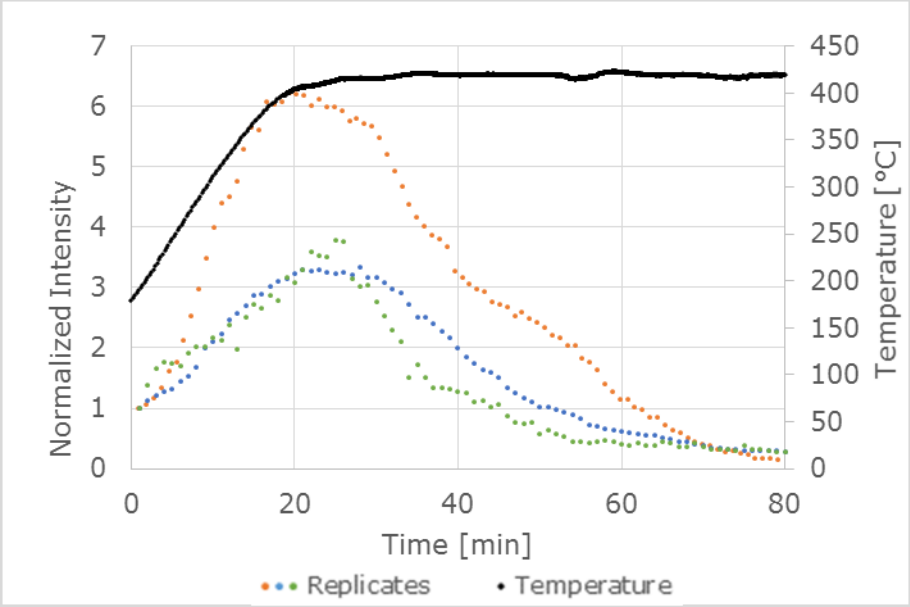

Figure D.1: Athabasca VR visbreaking at 420°C 532nm signal

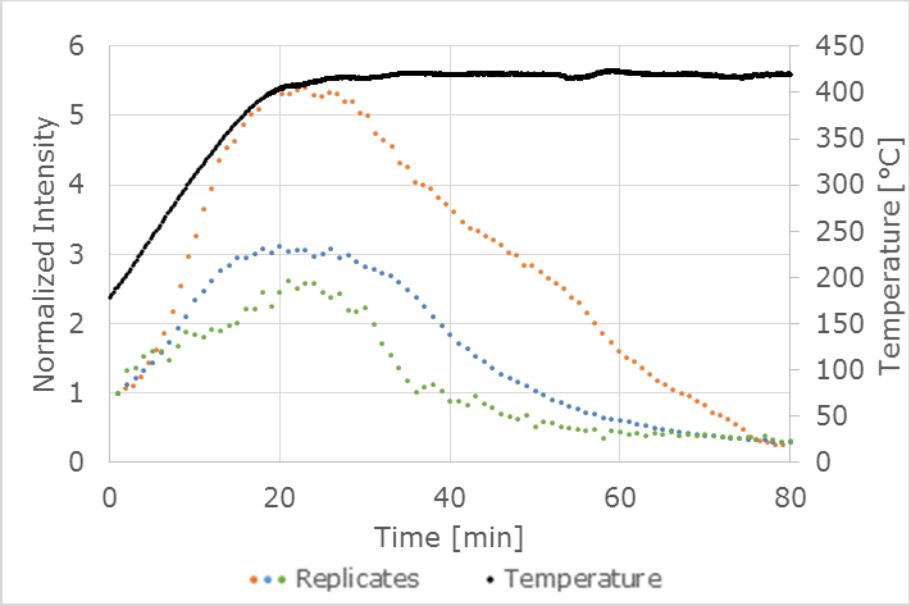

Figure D.2: Athabasca VR visbreaking at 420°C 655nm signal

The trend in the graphs even though shows a considerable difference in terms of backscattering signal intensity, qualitatively shows 2 similar characteristic stages explained in the previous studies of this system[1, 22]:

- Initial increase in the signal associated with the enhanced backscattering of the sample due to the heating.
- Once the system reaches reaction conditions, the backscattering signal begins to decline displaying a decreasing rate until the curve reaches a minimum.

These qualitative results, confirmed by 3 replicates, sufficed the purpose of validating the capability of this device to truly obtain information from the reacting sample. Further studies of this system were not pursued given the early stage of the development of this technique and the extreme complexity that such reactive medium poses to the interpretation of the results.

APPENDIX E: ANGLED-ENDED FIBER OPTIC

Appendix D covers in details the changes in the acceptance cone and numerical aperture of an angle ended fiber optics. The most common fiber optic termination explained in section 2.x consist in a perpendicular angle between the surface of its end-face and the axis of the fiber creating a circular profile. The numerical aperture in this cases is defined as a half-conical-angle by the equation showed before

$$NA = \sin \theta_{a_{max}} = \sqrt{{n_1}^2 - {n_2}^2} \qquad \text{Eq. E.1}$$

Where $\theta_{a_{max}}$ is the maximum acceptance angle of the fiber, showed in the previous figure 5.3., n_1 is the refractive index of the core material of the fiber and n_2 is the refractive index of the cladding material of the fiber.

In the case of an angle ended the surface and the axis of the fiber optics creates an angle <90°, creating an elliptical profile and thus changing the geometry of the propagating rays of light. Figure E.1. shows a critical ray of light propagating in the minor and mayor semi-axes respectively.

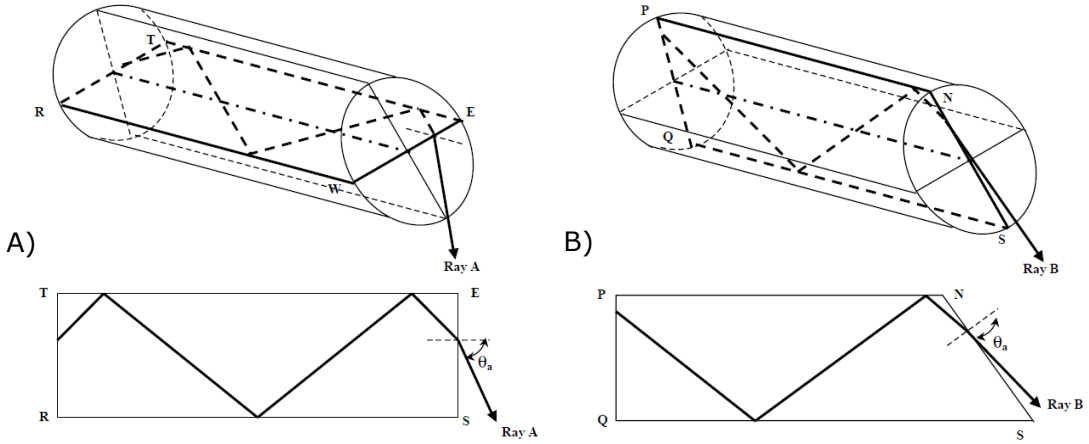

Figure E.1: Light propagation in angle ended fiber A) minor axis, B) mayor axis.[47] (used with permission)

The ray A propagating through the minor semi-axis behaves similarly as the perpendicular therefore the same equations can be used to describe the $\theta_{a_{max}}$. However considering the ray B propagating through the mayor semi-axis the critical angle differs significantly from the perpendicular case. Additionally the direction of the ray introduces two possible scenarios for the critical internal reflection depending on the relationship

between the tilt angle ε and the angle θ with respect to the fiber axis. Figure E.2. shows the representation of the propagating scenarios of ray B

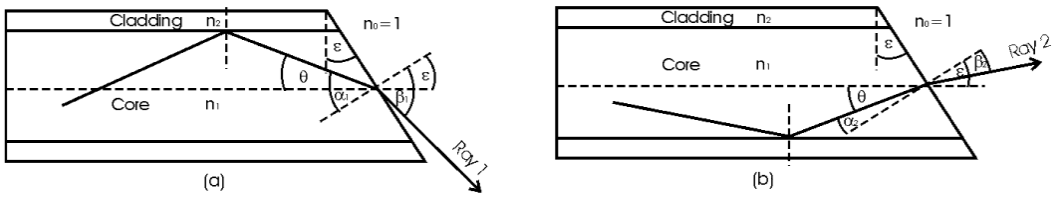

Figure E.2: Angle ended fiber Mayor Axis light propagation: a) ε ≤ θ, b) ε > θ .[48]

(used with permission)

In the case ε ≤ θ (a), the new incident angle α_1 will be increased by the tilt angle ε therefore

$$\alpha_1 = \theta + \varepsilon \qquad \text{Eq. E.2}$$

In the opposite case (b) when ε > θ, then the incident angle α_2 will be decreased by ε

$$\alpha_2 = \theta - \varepsilon \qquad \text{Eq. E.3}$$

The relationship within the internal reflection angle and the external propagation angle is calculated by using Snell's law of refraction as follow

$$n_1 \sin \alpha_1 = n_0 \sin \beta_1 \qquad \text{Eq. E.4}$$

$$n_1 \sin \alpha_2 = n_0 \sin \beta_2 \qquad \text{Eq. E.5}$$

Similarly to the traditional fiber end, there is a critical angle value that causes a total internal reflection of the light at the external fiber end interface, the presence of the tilt angle also involves additional changes to this critical value as follow

$$\varepsilon_{crit} = \sin^{-1} \frac{n_0}{n_1} \qquad \text{Eq. E.6}$$

The tilt-angle value must not exceed a maximum ε_{crit} to avoid total internal reflection of the light. It is important to note that n_0 refers to the external refractive index which in this specific case correspond to the window material given that the fibers terminations are in direct contact with the outer surface of the crystal during the measurement.